Title
Synthesis and Functionalization of Carbon and Boron Nitride Nanomaterials and Their Applications

Author
Erickson, Kristopher John

Publication Date
2012

Peer reviewed|Thesis/dissertation

Synthesis and Functionalization of Carbon and Boron Nitride Nanomaterials and Their Applications

By

Kristopher John Erickson

A dissertation submitted in partial satisfaction of the

requirements for the degree of

Doctor of Philosophy

in

Chemistry

in the

Graduate Division

of the

University of California, Berkeley

Committee in charge:

Professor Alex Zettl, Co-Chair
Professor Paul Alivisatos, Co-Chair
Professor Peidong Yang
Professor Ramormoothy Ramesh

Fall 2012

Abstract

Synthesis and Functionalization of Carbon and Boron Nitride Nanomaterials and Their Applications

Kristopher John Erickson
Doctor of Philosophy in Chemistry
University of California, Berkeley

Professor Alex Zettl, Co-Chair
Professor Paul Alivisatos, Co-Chair

Carbon and boron-nitride based nanomaterials possess many exciting properties making them suitable for numerous applications spanning from electronics to advanced composites. However, these materials when synthesized often differ significantly from the idealized crystals usually considered theoretically. A thorough understanding of the structure of the materials as synthesized and how the resultant materials can be utilized for specific application purposes is required such that these applications can be effectively realized. To this end, the synthesis and characterization of carbon and boron-nitride based nanomaterials is undertaken with specific application purposes in mind.

As a potential scalable synthetic route for graphene, graphene oxide (GO) and reduced graphene oxide are synthesized and characterized using atomic resolution electron microscopy. This elucidates their underlying structures revealing that the reduced form of GO does not resemble pristine graphene. The long-standing debate over the structure of GO is successfully ended with this study given the direct observation of the atomic structure of this material.

To develop advanced composite materials, the functionalization of carbon and boron nitride nanotubes is undertaken. The characterization of their functionalization and incorporation within composite materials, specifically within a Kevlar polymer matrix, is presented to allow for the development of composites with significantly enhanced mechanical properties.

Given a significant body of theoretical work paired with a single previous synthetic success, the synthesis of boron nitride nanoribbons is outlined. The first scalable synthesis of boron nitride nanoribbons is demonstrated resulting in long, consistent width, narrow, few-layer boron nitride nanoribbons which could be ideal for addressing these theoretical considerations.

To establish a method for the synthesis of thin hexagonal-boron nitride (h-BN), the design of a specialized CVD system is described. The material resulting from this system is analyzed with methods including atomic resolution electron microscopy with the results informing future approaches for the synthesis of h-BN.

Finally, high surface area boron nitride materials should be promising for hydrogen storage applications, especially if templated with a microporous scaffold. To this end, the first synthesis of a high surface area, microporous boron-nitride material is accomplished and the resultant surface areas of these materials are reported.

Sincere thanks to all of those who have helped me throughout this entire process with both my scientific pursuits and my pursuits outside of the lab. Special thanks to my wife for all her love and support during my time at Cal.

Table of Contents

Chapter 3: Boron Nitride Nanoribbons

Chapter 4: Hexagonal Boron Nitride

Chapter 5: High Surface Area Boron Nitride for H_2 Storage

Chapter 1: Graphene Oxide and Reduced Graphene Oxide

1.1 Motivation for Interest in Graphene

Graphene is material of significant interest to both the scientific and industrial communities as its properties have been proposed to yield exciting physics and numerous potential applications. Graphene is a single sheet of graphite, the most thermodynamically stable form of pure carbon, where sp^2 bonding exists between two carbon atoms 142 pm apart, forming its unit cell (Figure 1-1a). This unit cell, repeated in two dimensions with unit cell vectors a_1 and a_2 of length 246 pm, forms a "honeycomb" structure (Figure 1-1b) with each carbon bonded to three other carbons with both localized $\sigma_{c\text{-}c}$ bonds and delocalized π bonds forming from the remaining p_z orbitals of the carbon atoms. This delocalized bonding of the p_z orbitals is largely responsible for the elegant band structure of graphene indicating a zero-bandgap semi-conductor with massless relativistic carriers at the Dirac point. Weak interlayer interaction arises between stacked graphene sheets, and layers will form with an interlayer distance of 335 pm, stacking in an AB formation (Figure 1-1c) to form multi-layer graphite.

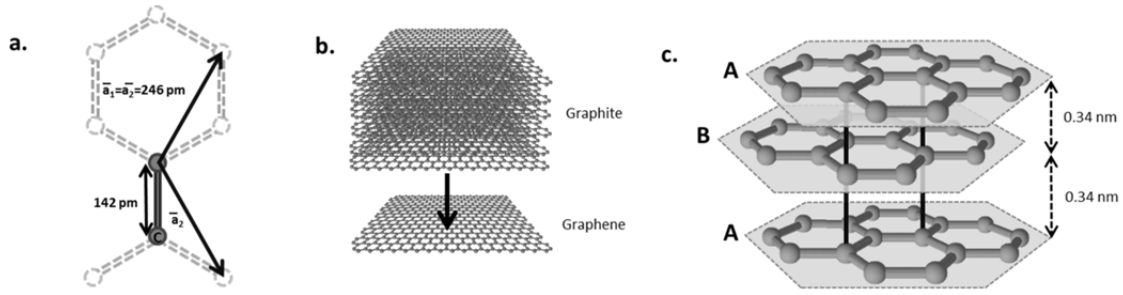

Figure 1-1. a. The unit cell of graphene consists of two carbon atoms spaced 142 pm apart. Unit vectors $\boldsymbol{a_1}$ and $\boldsymbol{a_2}$ translate in a plane to create the "honeycomb" lattice of graphene. **b.** When one layer is exfoliated off of bulk graphite, graphene forms. **c.** The stacking of bulk graphite is ABA in the *c* direction where adjacent layers are offset from one another with a consistent interlayer spacing of 0.34 nm.

Some of the most impressive, and potentially useful, properties of graphene include its ballistic transport with an exceptionally high carrier mobility of up to 200,000 $cm^2/(V \cdot s)$,[1] at carrier concentrations of 10^{13} $1/cm^2$,[2] a half integer quantum hall effect,[3] high transparency within the visible range, exceptional thermal conductivity of 5,000 $W/(m \cdot K)$,[4] a very high surface area of 2,620 m^2/g as well as a Young's modulus around 1.0 TPa.[5] These impressive characteristics pose it well for use in numerous applications. Envisioned uses include use as a field effect transistor, for memory applications, as a sensor, as a transparent electrode for photovoltaics or electronics, as a supercapacitor or battery electrode, and for composite enhancement.[6] The myriad applications as well as the exciting fundamental physics investigations possible with graphene make it a material of the utmost interest for researchers. Indeed it has become a material under intense investigation within many scientific disciplines.

1.2 Synthesis of Graphene

To realize the proposed applications for graphene, high quality graphene must be synthesized in a bulk, scalable fashion. The original synthesis of graphene was done using the "scotch tape" method (Figure 1-2a),[2] whereby individual sheets of graphene were exfoliated from bulk graphite simply by repeatedly attaching and pulling apart scotch tape with graphite in between, followed by firmly placing the tape onto a silicon wafer. Although brilliantly simple, this method produced very few single sheets of graphene which were randomly spaced upon a silicon wafer and were also surrounded by multilayer graphene flakes. This approach is not scalable and lithography paired with microscopy is necessary for device fabrication of such graphene samples. However, the quality of the graphene achieved through this route is still unmatched (in terms of its high mobility and low numbers of defects),[1] and fundamental physics studies requiring graphene often still utilize this route for graphene synthesis.

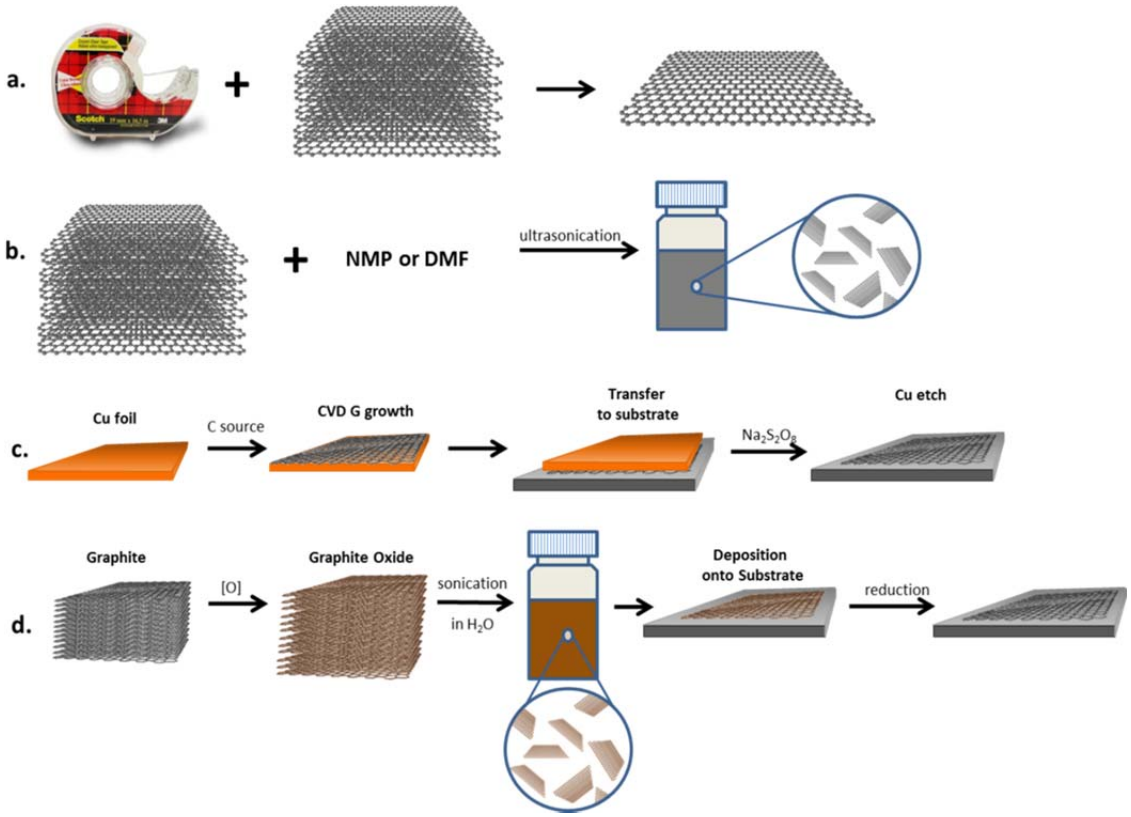

Figure 1-2. Cartoons indicating methods for the production of graphene include **a.** "Scotch tape" method whereby individual sheets of graphene are mechanically exfoliated from bulk graphite via the repeated peeling apart of tape with graphite attached. **b.** Solvent based exfoliation whereby bulk graphite is exfoliated into solution via ultrasonication. **c.** CVD growth of graphene via the decomposition of a carbon source upon a transition metal substrate (often copper) after which the substrate is etched away. **d.** Synthesis via graphene oxide (GO) whereby graphite is oxidized in the bulk to graphite oxide and the exfoliated in solution via sonication after which the material can be deposited on a substrate and then reduced back to graphene.

A more scalable route to graphene was envisioned whereby exfoliation could be induced within a stabilizing solvent.[7] It was believed that high quality graphene could simply be exfoliated within a solvent and then incorporated within any desired architecture (onto 2D substrates or within 3D composite materials). This approach would achieve material in the bulk and would thus be scalable in an industrial setting. Although relatively high concentrations of graphene could be achieved (~0.01 mg/mL) in solvents such as N-methyl-pyrrolidone, there were many drawbacks. The quality of the resulting graphene sheets was greatly under question, single sheet material was still very difficult to obtain, and conductivities were much lower than expected.[7] However, alternative methods for direct exfoliation within a solvent system are still being investigated,[8] and could eventually yield bulk solutions of pristine graphene.

The turning point in graphene research with an eye for application was with the bulk 2D synthesis involving the decomposition of carbonaceous feedstock onto a catalytic substrate under standard chemical vapor deposition (CVD) growth conditions. Initial syntheses on Ni foils showed promise as high quality films of potentially arbitrary size of graphene could be grown on commercial Ni foils by the decomposition of methane at 1,000 °C under Ar flow.[9] However, these films were rarely single sheets of graphene, and although promising mobilities of these films could be achieved, tailoring this synthesis to yield thinner material seemed difficult. The breakthrough came as the catalytic substrate was changed to Cu[10] whereby continuous graphene films almost entirely composed of a single graphene layer could be synthesized on a bulk substrate. This approach to graphene synthesis has been widely utilized within the graphene research community showing to potentially be scalable for commercial production[11] while displaying high mobilities of up to 37,000 $cm^2/(V \cdot s)$.[12]

However, this promising synthesis is geometrically limited in the sense that it is grown on a substrate and can never be scaled to produce kilogram quantities of graphene (in fact, to synthesize a single kilogram of graphene via this method, 1.3 km^2 of catalytic substrate would be required!). Given this, a method for the bulk production of graphene is highly desired especially when considering it for applications within the fields of batteries, supercapacitors, and composites, all of which require kilogram quantities of material for commercially viable products.

Considering this, approaches have been made to synthesize graphene via graphene oxide (GO). Essentially, a bulk quantity of graphite can be oxidized in solution to result in graphite oxide. This material can then be exfoliated in a variety of solvents, including water, via moderate sonication or prolonged stirring to yield single sheets of GO. At this point, the GO material can be incorporated within another material (for instance, for composite reinforcement), be deposited in the bulk onto a substrate (for instance, for battery or supercapacitors electrode materials), or be deposited as single sheets on a substrate (for instance, for transparent electrodes). Following the incorporation into various architectures, the GO can be reduced to form a material potentially resembling graphene. The scalability and versatility the GO approach poses this synthesis as the most promising route to graphene for many application purposes.

1.3 Debate over the Structure of Graphene Oxide

Considering the structure of GO, although the parent graphite material if exfoliated to a single sheet would very well resemble graphene, the two requisite steps for synthesizing graphene via GO, with the initial oxidation and subsequent reduction, may make the reduced form of GO differ substantially from graphene. Therefore, the reaction pathways for GO and reduced GO must be well understood as these reactions will determine the final structure of reduced GO and how well it resembles graphene. The initial oxidation is most often done with the *in situ* formation of Mn_2O_7 formed via $KMnO_4$ within an acidic medium (often H_2SO_4).[13] Usage of this powerful of an oxidant is necessary given the inert nature of graphite (being the highest of common materials on the galvanic series), but can result in over-oxidation (carbons more than singly oxidized) of the graphitic material (Figure 1-3). Indeed, CO_2 formation is common during graphite oxidation via this route[14] meaning that single, double, triple and quadruple oxidation of carbon atoms within the basal plane of the parent graphene does occur. However, the extent to which this over-oxidation occurs is not well understood and has been under significant debate for the greater part of a century (Figure 4).[15] The actual functionalities within GO are part of this debate and hydroxyls, epoxies, carbonyls, and carboxylic acid functionalities are the main functionalities believed to exist within GO.[13]

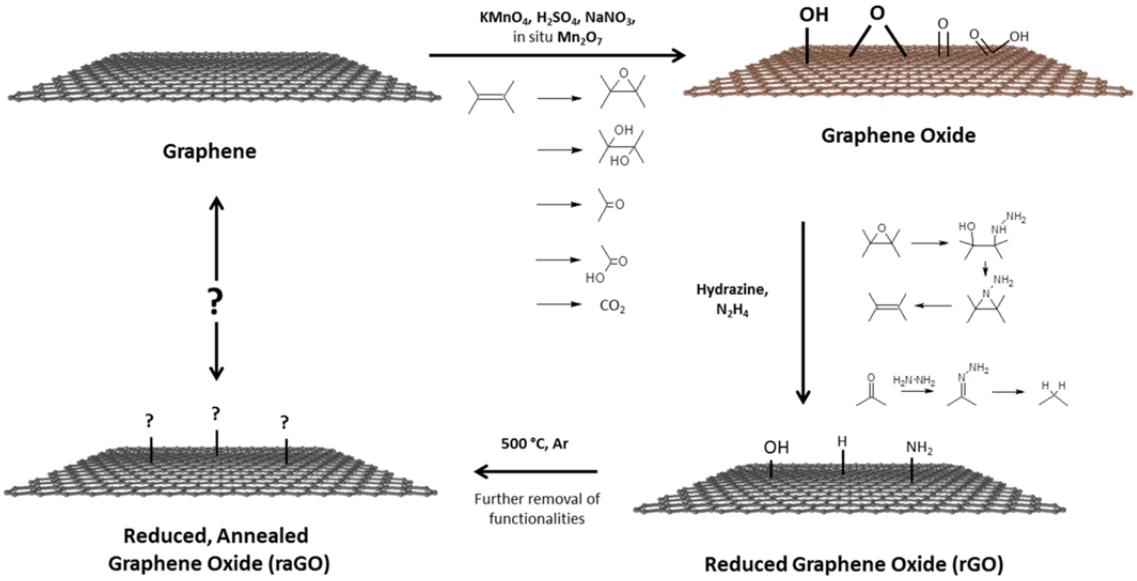

Figure 1-3. Reaction scheme for the synthesis of graphene via GO. First, oxidation of graphene is accomplished via *in situ* Mn_2O_7 formation with a number of possible functionalities resulting, including epoxies, hydroxyls, carbonyls, carboxylic acids. Full oxidation of carbon atoms results in removal of the carbon from the basal plane in the form of CO_2. GO is then chemically reduced via hydrazine through a few known reactions schemes and results in the removal of most of the GO functionalities. However, this reduction will depend on the initial functionalities of the GO material and full removal of functionalities is not achieved after chemical reduction. A high temperature anneal in an inert environment is then done to further remove remaining functionalities. However, the extent to which functionalities are fully removed and the resulting structure of reduced, annealed GO is not well understood.

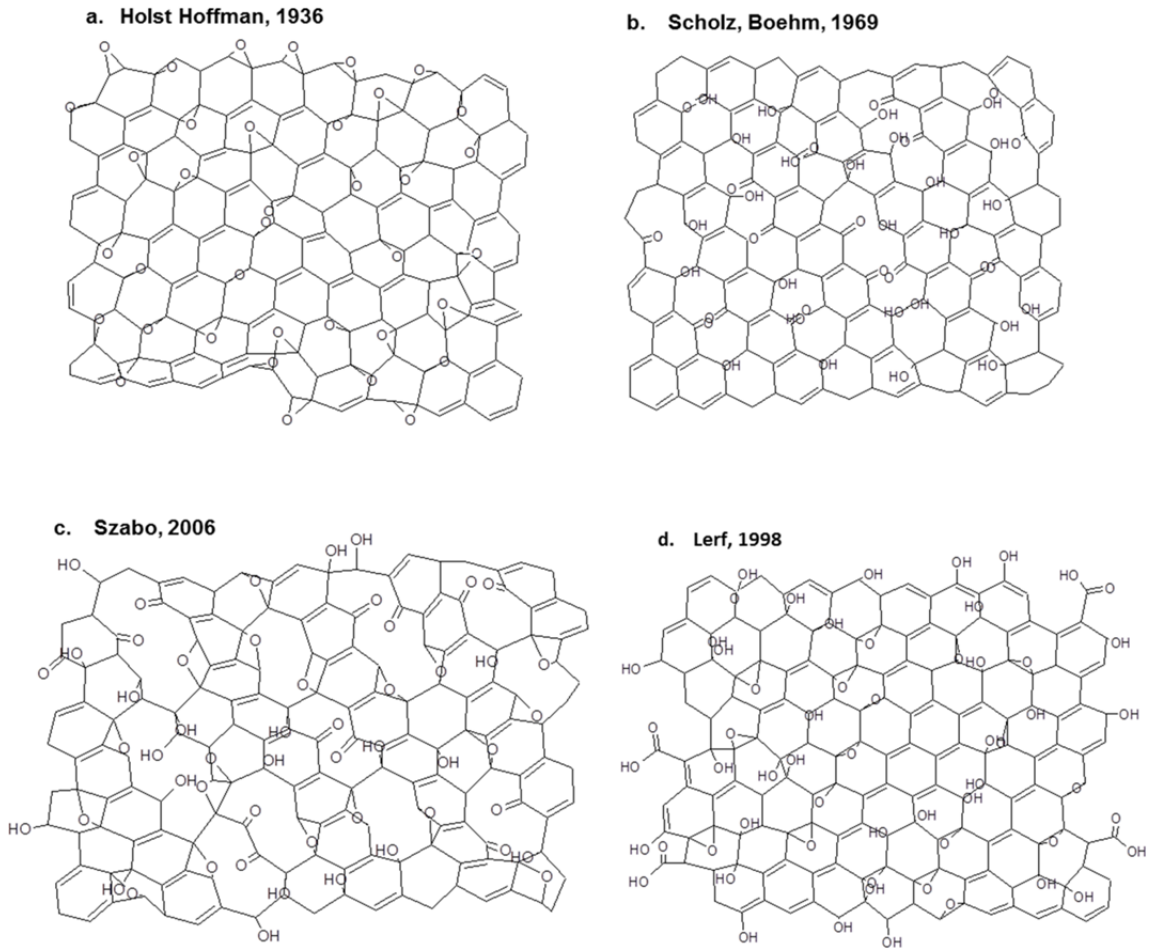

Figure 1-4. Representative structures of a few structural theories for GO and the years of the theory. **a.** The "Holst Hoffman" structure[16] proposed that (1,2) epoxies were the only functionalities on GO. **b.** The "Scholz, Boehm" structure[17] proposed that quinones and hydroxyls were the only functionalities which formed in lines of functionality with adjoining lines of double bonded regions. **c.** The "Szabo" structure[15] proposed that (1,3) ethers, hydroxyls and carbonyls were the major functionalities of GO. **d.** The "Lerf" structure[18] proposed that (1,2) epoxies and hydroxyls were the main functionalities with carbonyls existing on the edges of the GO sheets. This theory was also the first to proposed regions that retained aromaticity.

Following the initial oxidation, reduction of GO is accomplished in two steps (Figure 1-3). First, a chemical reduction is done via reaction with hydrazine, forming reduced graphene oxide (rGO). Hydrazine is understood to reduce some of the common functionalities expected on GO, but many reaction routes for the assumed reduction of functionalities is not well understood.[19] Hydrazine reduction has also been seen to incorporate in C-N bonds (via XPS analysis).[19] Following this chemical reduction, further reduction is accomplished by an inert environment, high temperature anneal to form reduced, annealed graphene oxide (raGO). This step further removes functionalities and helps to restore the structure to the most thermodynamically stable form of a purely graphitic structure.

The material at this point has undergone a harsh oxidation followed by a potentially incomplete reduction. If oxidation occurs past single oxidation of carbon atoms which form hydroxyls or epoxies, then carbon-carbon bonds are broken. This

bond breakage will not be restored during chemical reduction and the moderate annealing employed. Although higher temperature annealing should restore much of the material to a graphitic state, any carbon lost during oxidation will never be replaced through simple reduction and annealing. Also, the higher temperatures necessary for a more restored graphitic structure make the argument for an economically viable route to graphene more tenuous. Therefore, the structure of GO and the resultant raGO must be determined such that the practicality of its use as a route to graphene can be assessed.

1.4 Spectroscopic Methods for GO Structural Determination

Many spectroscopic methods have been utilized to better understand the structure of GO and raGO.[19] Among them, X-Ray Photoelectron Spectroscopy (XPS) and Fourier Transform Infrared Spectroscopy (FTIR) are useful techniques for determining types of bonds within GO.

1.4.1 XPS Analysis

With XPS spectroscopy, an X-Ray source, in the keV range, is focused onto a sample which undergoes core-shell ionization (Figure 1-5a). Given the energy of the photon, the kinetic energy of the emitted electron and the detector work function, the binding energy of the core electron can be determined (Figure 1-5b). This technique gives very good atom type determination as well as chemical bonding nature given the variation of binding due to various bonding types. Some limitations of XPS are that it is a surface limited analysis technique (probing the top ~10 nm of material) as well as requiring ultra-high vacuum conditions.

When analyzing GO, rGO and raGO, XPS data seems to indicate complete removal of the functionalities found within GO (Figure 1-5c). Indeed, the initial signal found in the 287 eV range which indicate the significant presence of oxidative functionalities (mainly singly oxidized, but some higher oxidation states as well),[19] are almost fully removed upon initial reduction and also with the raGO material. Although noise may mask residual signals within this data, a stark contrast between the initial significant signal from oxidative functionalities in GO and the lack of this signal for rGO and raGO seems to indicate that removal of the functionalities within GO is very successful using these conditions.

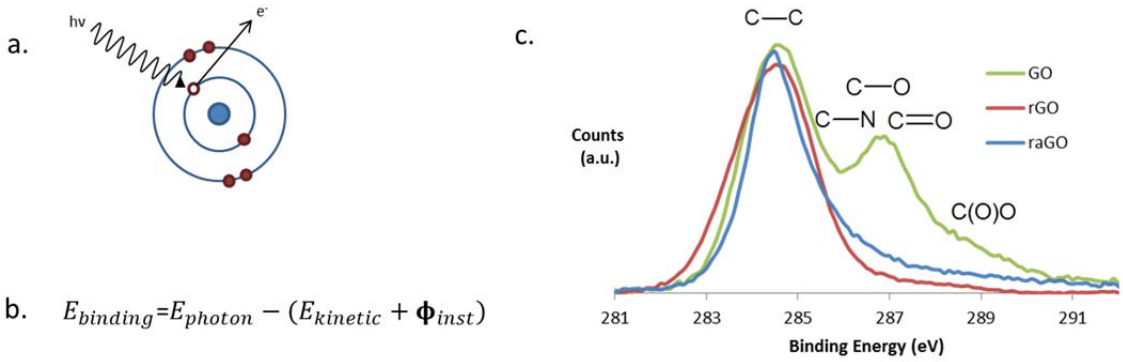

Figure 5 a. Cartoon representation for the process occurring during XPS analysis whereby a high energy photon (and X-Ray) ionizes a core electron from an atom. **b.** Equation for determining the binding energy ($E_{binding}$) of the electron within the original atom, being equal to the X-Ray energy (E_{photon}) minus the measure kinetic energy of the ejected electron ($E_{kinetic}$) minus the work function of the detector (ϕ_{inst}) **c.** C-1s XPS spectrum of GO (green line), rGO (red line), and raGO (blue line). The labeling above indicates the type of bond expected to give signal in the corresponding range with C-C at 284.5 eV, C-N at 286 eV, C-O at 286.5 eV, C=O at 288 eV, and C(O)O (carboxylic acid functionality) at 289 eV.[19] It should be noted that the rGO and raGO spectra exhibit very little signal in all ranges other than the C-C range.

1.4.2 FTIR Analysis

An assessment of the effectiveness of reduction and annealing at the removal of functionalities from GO is made when considering the FTIR spectra of GO and raGO (Figure 1-6). Hydroxyl, epoxy and carbonyl functionalities are significant features with the GO spectrum but seem to be almost completely removed after reduction and annealing, making the raGO spectrum closely resemble the FTIR spectrum of bulk graphite. It should be clarified that the aromatic C=C peak seen in GO at 1590 cm^{-1} is expected to diminish almost completely as the IR active vibration which exists for simple aromatic groups changes symmetry becoming Raman active (IR inactive) with C=C bonds in an extended aromatic material like graphite.

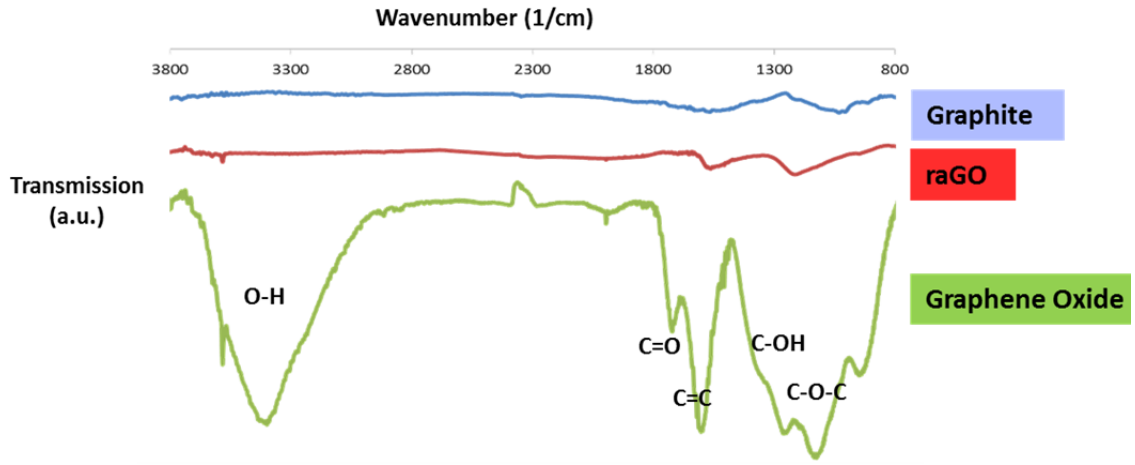

Figure 1-6. FTIR spectrum of GO (green), raGO (red), and graphite (blue). Initially, significant signal from the expected functionalities of GO is present with a broad O-H stretch at 3430 cm^{-1}, carbonyl stretch at 1730 cm^{-1}, aromatic C=C at 1590 cm^{-1}, C-OH stretch at 1230 cm^{-1}, and C-O-C stretch at 1100 cm^{-1}.[20] Following reduction and annealing, raGO lacks any of these functionalities, even losing signal from the aromatic C=C bonds given the change of symmetry to a Raman active mode when in a graphitic bonding structure.

1.4.3 Raman Spectroscopy Analysis

Assessing FTIR and XPS spectroscopy by themselves seems to indicate that full removal may occur in GO and the potential for GO to be fully restored to a graphitic structure following reduction and annealing could be argued for. However, other spectroscopy seems to indicate otherwise. Raman is useful for assessing graphitic materials given the many Raman active modes within the typical analysis range (Figure 1-7). Focusing on the 1100-1800 cm^{-1} range, two major features will occur with graphitic materials. The G-band occurs for all graphitic materials coming from an in-plane oscillation of the graphitic honeycomb structure (Figure 1-7a). However, the D-band is defect induced and will only be active when disruption of the crystalline lattice occurs within a graphitic material. This can be a defect from lost carbon from the basal plane or from functionalities that disrupt the sp^2 bonding between carbon atoms in a perfect graphene crystal. Therefore, D-band signal can be a good spectroscopic tool for determining the crystallinity of a graphitic material. In the case of GO, significant D-band signal is expected given the prevalence of functionalities within the GO structure. However, if complete removal of functionalities and a restoration of the GO structure occurs during reduction and subsequent annealing, this signal should be completely absent in the raGO Raman spectrum. Quite to the contrary, rGO and raGO are seen to have almost identical D-band signal compared to GO, whereas a high quality graphene sample will have no D-band signal. This is commonly the case with materials derived from GO,[19] and is the first spectroscopic method presented here indicating that the structure of raGO and graphene may significantly differ.

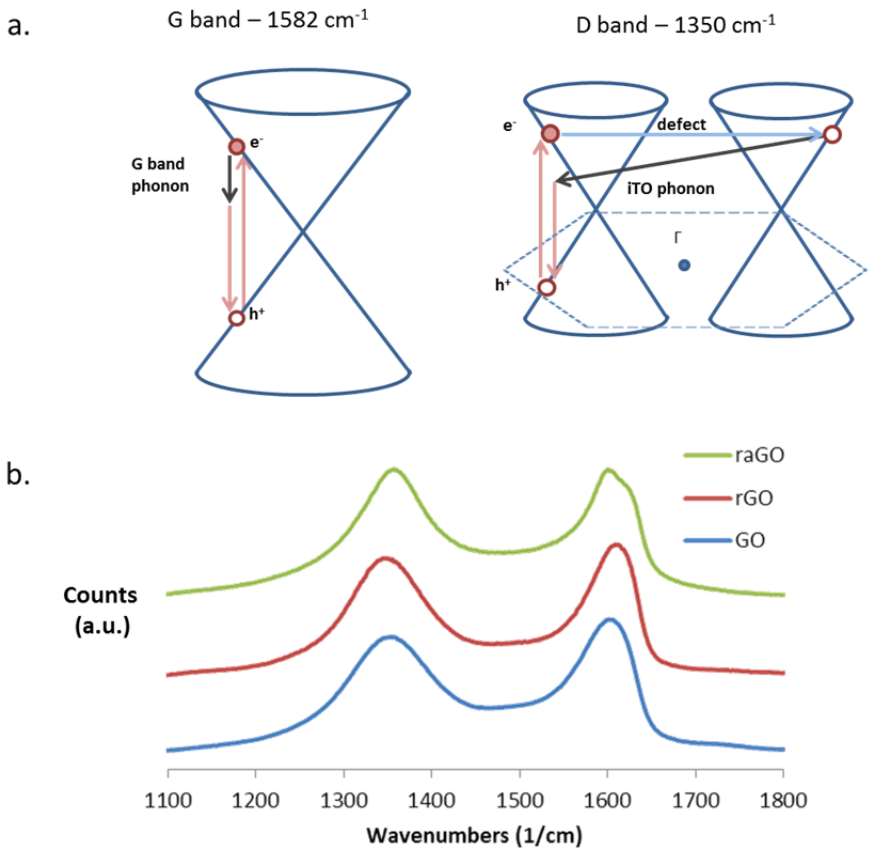

Figure 1-7. a. Cartoons of graphitic Raman modes in the 1100-1800 cm^{-1} range. The cones represent the Dirac cone features of the band structure of graphene at the K and K' points. The G-band, at 1582 cm^{-1} for a 514 nm excitation, is a doubly degenerate phonon mode with E_{2g} symmetry. The D-band, at 1350 cm^{-1} for a 514 nm excitation, is only active when a defect scatters the excited electron from one Dirac cone to another, mediated back by an iTO phonon excitation. **b.** Raman spectra of GO (blue), rGO (red), and raGO (green). Within this range, the D-band is noticed for all samples at ~1350 cm^{-1} and the G-band as well at ~1580 cm^{-1}.

1.4.4 Assessment of Spectroscopic Analyses

Another indication of a lack of return of GO to graphene upon reduction and annealing comes from looking at the conductivity of GO and raGO compared to the conductivity of graphene. The significant oxygen functionalities imparted during the oxidation of GO results in significantly reduced conductivity in GO resulting in conductivities in the range of 10^{-3} S/cm.[21] Upon reduction, significant conductivity is restored and samples have conductivities of up to 300 S/cm.[21] However, this is still far from reported values for the conductivity of pristine graphene at around 5,000 S/cm.[21]

Between the Raman analysis and the commonly found lack of raGO conductivity compared to pristine graphene, it is evident that some difference between raGO and graphene likely exists. This raises the question: can oxidized graphene indeed be effectively converted back to graphene, and if not, what can it be converted to? Central to this question are the detailed atomic structures of GO and raGO, which, despite their importance, remain largely unknown.[15]

1.5 Aberration Corrected Transmission Electron Microscopy Investigation of GO and raGO

Usage of aberration corrected microscopy techniques could be very valuable in elucidating the GO structure. Aberration corrected microscopy is a powerful technique which applies to any microscopy technique by correcting for two major aberrations which arise when focusing either a beam of photons or electrons. Chromatic aberrations occur when the incoming beam has an energy spread with the higher energy portion of the beam refracting at a larger angle (Figure 1-8a). Spherical aberrations arise whenever focusing a beam as an imperfect lens will spread the focal point of the focused beam (Figure 1-8a). Both of these aberrations can be corrected for by adding additional lenses and chromatic aberration can be minimized by decreasing the energy spread of the incoming beam and through corrective lenses.

The utility of this technique is very apparent when comparing micrographs of graphene with a non-aberration corrected JEOL 2010 microscope (Figure 1-8b) and an aberration corrected microscope (Figure 1-8c). Without aberration correction, only adsorbates and residual polymer from the transfer can be seen on top of graphene, but the underlying graphene sheet is almost invisible given its significant electron transparency and lack of features resolvable at the resolution possible without aberration corrected. This is starkly contrasted with the atomic resolution micrograph of graphene possible with an aberration corrected transmission electron microscope (TEAM 0.5, at the National Center for Electron Microscopy at the Lawrence Berkeley National Laboratory), where each individual atom of graphene can be resolved revealing the honeycomb structure of graphene. This technique for producing atomic resolution micrographs of graphitic materials will be very powerful when analyzing GO and raGO in terms of being able to greatly contribute to the debate over their otherwise not well understood structures. This technique is especially useful considering the unperturbed nature of the sample when analyzed while suspended on a TEM grid, compared to techniques requiring a substrate like STM and AFM.

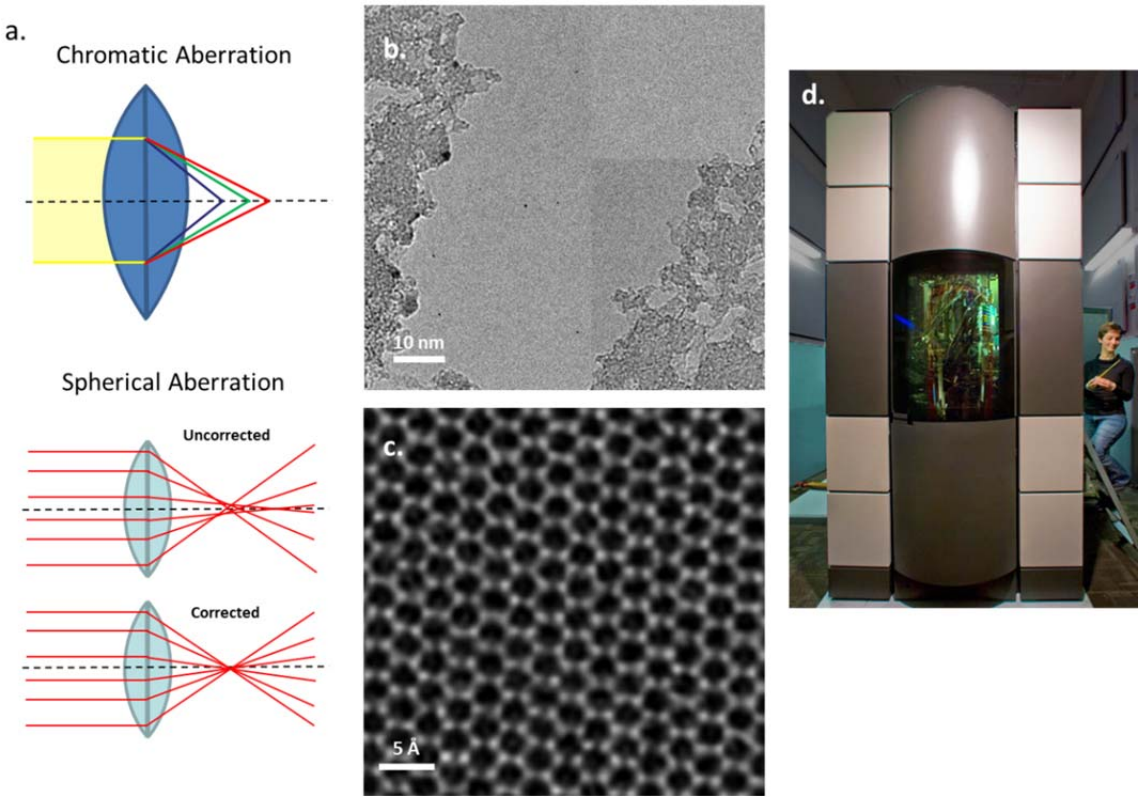

Figre 1-8. a. Cartoons indicating the spreading of a focused beam due to chromatic aberration (top) given an energy spread of an incoming beam or due to spherical aberration (bottom) owing to the imperfect nature of any lens (especially electromagnetic lens for electron optics). **b.** TEM micrograph of a graphene film using a non-aberration corrected TEM, JOEL 2010 (courtesy of Nasim Alem). The graphene film is the featureless material in the middle of the micrograph, being surrounded by adsorbates and residual polymer for the transfer technique. **c.** TEM micrograph of graphene using an aberration corrected TEM (TEAM 0.5) within which each atom of graphene can be resolved forming a honeycomb-like structure (courtesy of Rolf Erni).[22] **d.** Photograph of the TEAM 0.5 microscope used for "c." and for the high resolution micrographs of graphene, GO and raGO following which is housed at the National Center for Electron Microscopy (NCEM) at the Lawrence Berkeley National Laboratory in Berkeley, CA. (image courtesy of NCEM)

1.5.1 GO and raGO Synthesis

For the presented aberration corrected TEM graphene, GO, and raGO study,[23] GO was produced via a modified Hummers' method.[24] All chemicals were used from Sigma-Aldrich as received. Reverse osmosis de-ionized water was used throughout the experiment. Briefly, 0.5 g of graphite powder (200 mesh) was added to a mixture of 0.5 g of $NaNO_3$ and 23 mL of H_2SO_4 (98%) in an ice bath. Following the addition of the graphite, 3 g of $KMnO_4$ was slowly added. The solution was brought to 35 °C and stirred for one hour until a thick paste formed. To the paste, 40 mL of water was slowly added under stirring. This solution was brought to 90 °C and stirred for 30 min. After the addition of 100 mL of water, 3 mL of H_2O_2 (30%) was slowly added under vigorous stirring. The color of the solution turned from a dark brown to a bright yellow.

The resulting material was centrifuged to precipitate most of the material. This precipitate was placed under dialysis for 1 day, with many changes of the surrounding water. To aid exfoliation, the solution was mildly sonicated at low power for 10 minutes. Following moderate centrifugation to remove large particles, the supernatant was diluted 4:1 with MeOH, to aid in TEM grid preparation. This material was stable in solution for at least 6 months.

The GO in MeOH/H_2O solution was drop cast onto lacey carbon grids (400 mesh) and allowed to air dry. For raGO samples, grids were placed in a loosely covered beaker with an open reservoir of hydrazine (N_2H_4) for 12 hours. Following modest vacuum annealing (100 °C, 150 Tor, in N_2 atmosphere), grids were moved to a clean quartz tube and placed in a CVD furnace. Under constantly flowing N_2 (200 ccm), the tube was heated at 105 °C/hr to 550 °C and held at this temperature for one hour. The tube was allowed to slowly cool to room temperature over the course of 4 hours. Initial microscopy with a HRTEM (JEOL 2010) at 100kV confirmed the layer number for suspended specimens via electron diffraction (Figure 1-9).[25, 26]

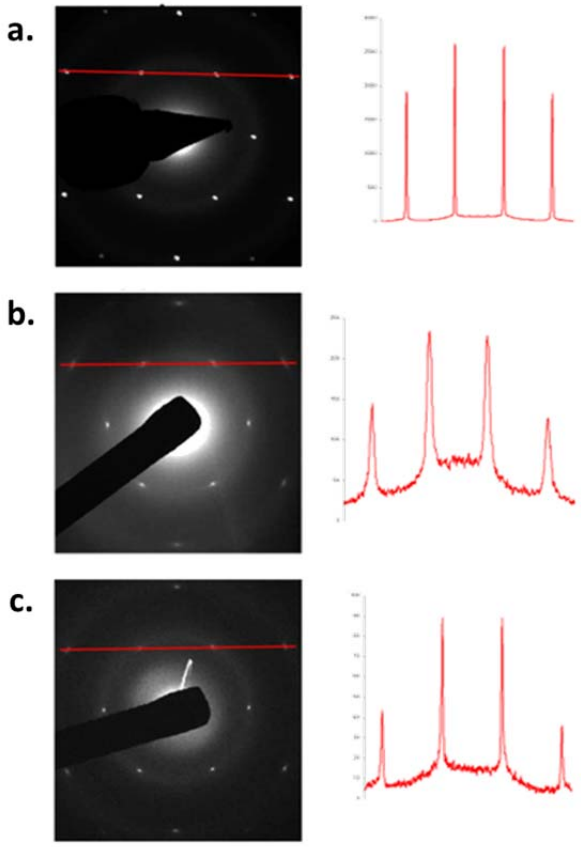

Figure 1-9. a. Diffraction indicating a monolayer of graphene. A line profile (red line), with the number of counts shown below the diffraction pattern, shows the (1-210) type reflections to be lower in intensity than the (0-110) type reflections. Assuming no significant sample tilt, this indicates a single sheet of graphene.[26] **b.** Diffraction indicating a monolayer of GO. A similar line profile (red line), shows the (1-210) type reflections to be lower in intensity than the (0-110) type reflections. Assuming no significant sample tilt, this indicates a single sheet of GO. **c.** Diffraction indicating a monolayer of raGO. A similar line profile (red line), shows the (1-210) type reflections to be lower in intensity than the (0-110) type reflections. Assuming no significant sample tilt, this indicates a single sheet of raGO.

1.5.2 Microscopy Conditions and Analysis Details

Atomic resolution micrographs were obtained with the TEAM 0.5 TEM (a monochromated aberration-corrected instrument operated at 80 keV). TEAM 0.5 imaging was performed in a high vacuum environment ($<10^{-7}$ mbar), and the electron monochromator was adjusted to enable an energy spread of the electron beam of less than 0.2 eV. The aberration corrector was fine tuned to obtain a third-order spherical aberration of -14 μm, which in consideration of the positive fifth-order aberration of 5.2 mm yielded an optimal phase contrast for a slight positive defocus of +8 nm down to the information limit of 0.08 nm at 80 kV. The resulting electron dose is approximately $2.8*10^6$ electrons/(sec*nm^2). Details of the microscope configuration can be found elsewhere.[27, 28] Grids were briefly (8 min.) placed on a hot plate at 140°C to facilitate ambient hydrocarbon desorption.

Throughout this study, the simulations of the TEM images were done with the program MacTempasX Version 2 simulating the structures proposed in each of the corresponding figures. The simulation parameters were entered to match the experimental microscope conditions. Furthermore, for the proposed potential atomic structures in Figures 2 and 3, the atomic representations were created using the program ACD/ChemSketch (Freeware), version 11.02. After creating a structure for the proposed structures, the 3D Optimization feature was utilized which calculates a lowest energy structure based on bond stretching, angle and rotation as well as Van der Waals interactions. The 3D Viewer feature was used to create the 3-dimensional representations found in the figures. Finally, images used in the following study were analyzed using the program ImageJ, version 1.40g. Images were filtered with the FFT Bandpass Filter function with a high bandpass filter of 80 pixels and a low bandpass filter of 2 pixels, with one pixel equaling 0.24 Å, for enhanced visualization.

1.5.3 Graphene, GO, and raGO Atomic Resolution Microscopy Study

Figure 10 shows high resolution TEM micrographs of suspended monolayer sheets of graphene, GO, and raGO, respectively. Images were processed with an FFT bandpass filter for greater clarity. As is well known,[26] graphene consists of an extended, two dimensional sp^2 bonded carbon "honeycomb" lattice. After heating and additional electron beam exposure, hydrocarbon adsorbates, often seen during TEM imaging,[29] desorb, leaving a pristine graphene sheet (Figure 1-10a).

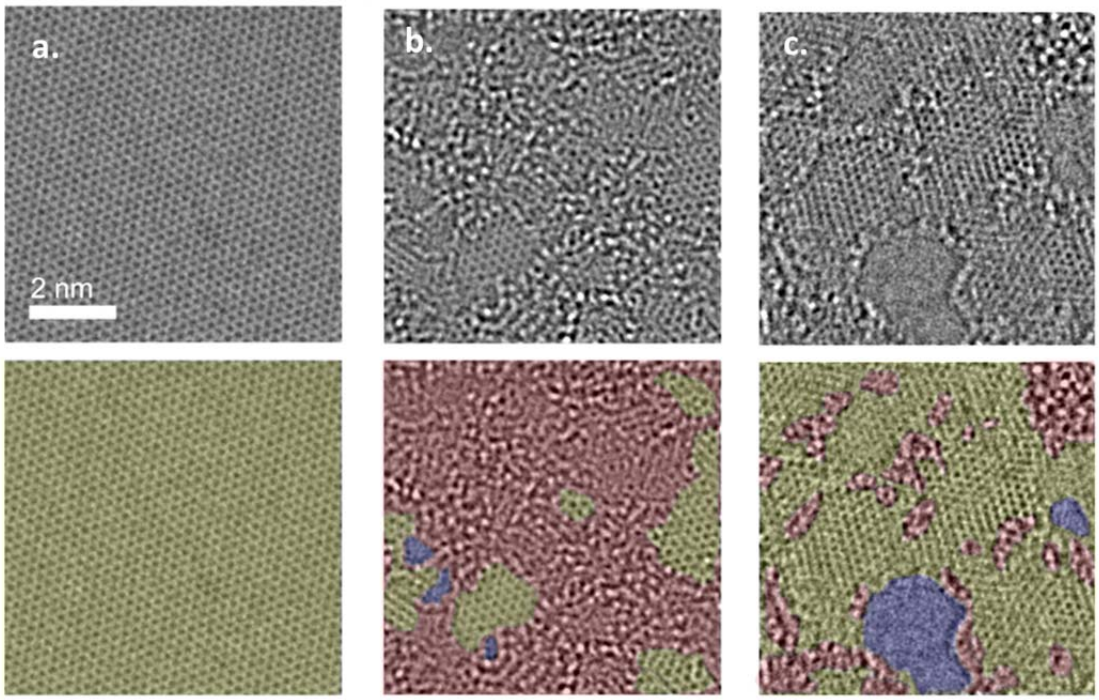

Figure 1-10. Aberration corrected TEM micrographs of the following materials. Scale bar, denoting 2 nanometers, is valid for all micrographs. **a.** Single suspended sheet of graphene. On the bottom, graphitic area indicated in yellow. **b.** Single suspended sheet of GO. On the bottom, holes are indicated in blue, graphitic areas in yellow, and high contrast, disordered regions, indicating oxygen functionalities, in red. **c.** Suspended monolayer of raGO. On the right, holes indicated in blue, graphitic regions in yellow, and areas with remaining functionalities in red.

Following oxidation of the parent graphene, the resulting GO material (Figure 1-10b) is found to be highly inhomogeneous with respect to structure. Three major features are present: holes (indicated in blue), graphitic regions (indicated in yellow, as they were for Figure 1-10a), and high contrast disordered regions (indicated in red), indicating areas of high oxidation, with approximate area percentages of 2%, 16%, and 82%, respectively. Holes form in GO as CO and CO_2 are released during the aggressive oxidation and sheet exfoliation,[14] found here to be usually less than 5 nm^2. Although some high resolution electron microscopy studies have not reported holes in GO samples,[30] a high resolution aberration corrected electron microscopy study of the reduced form of GO has observed similar holes.[31] Graphitic regions, covering between 1 and 6 nm^2, indicate incomplete oxidation of the basal plane with the preserved honeycomb structure and 1.4 Å atomic spacing of graphene. The disordered, high contrast oxidized regions of the basal plane form a continuous network throughout the GO sheet. Monolayer raGO (Figure 1-10c) is similarly structurally inhomogeneous with holes (blue), graphitic regions (yellow), and disordered areas with high contrast (red). The observed holes comprise approximately 5% of the area. An increase in the area of holes compared to GO is expected as CO and CO_2 form during annealing.[32] The anticipated significant increase in graphitic area observed, up to approximately 70% of the area, indicates a substantial restoration of the original sp^2 bonding character lost during the oxidation, by the reduction of oxygen functionalities. However, extensive disordered high contrast regions still exist, likely from nitrogen and oxygen functionalities which persist even after reduction and

annealing.[33] Uninterrupted translational order, as observed with pristine graphene, is not seen, being disrupted by the holes and the remaining functionalities.

This raGO material under study is substantially different from graphene as indicated by Figure 1-10. Although significantly restored graphitic nature is imparted upon reduction, the remaining functionalities and holes in raGO drastically differentiate it from graphene. Attempts at synthesizing limitedly oxidized graphene oxide or at introducing a carbon feedstock for the "healing" of raGO show promise for potentially addressing these observed differences between raGO and graphene, possibly resulting in minimal defects and reincorporation of carbon into the basal plane when missing from the synthesized raGO material.[21, 34-36]

1.5.3.1 Detailed GO Analysis

The structure of GO can be better elucidated by a closer look at the electron micrographs of GO. The main body of Figure 1-11 shows another representative TEM image of GO, suitable for detailed examination. A high contrast region is selected in Figure 1-11a. With this sample, adsorbates are understood to be limitedly present, and if present, to only be adsorbed onto the oxidized regions of GO. Grid heating prior to TEM imaging largely desorbs such weakly, physically bonded species. Furthermore, electron beam exposure induces desorption and motion of such weakly, physically bonded species,[29] resulting in minimally observed adsorbates in the similarly prepared and imaged graphene and raGO samples (Figure 1-10a and 1-10c). Finally, time-dependent changes in the overall area of the high contrast regions would be expected during TEM imaging if they were caused by large numbers of adsorbates as some of these adsorbates would desorb under electron
beam exposure. However, the increased Van der Waals interaction between adsorbates and oxidative functionalities compared to their interaction with graphitic regions means that any remaining adsorbates would be adsorbed to the oxidized regions of GO. High contrast regions are thus primarily from oxidized carbons and limitedly from adsorbates, which indicate an underlying oxidized region. The high amount of contrast variation indicates a high density of oxygen functionalities, with each carbon likely being oxidized with no order between functionalities.

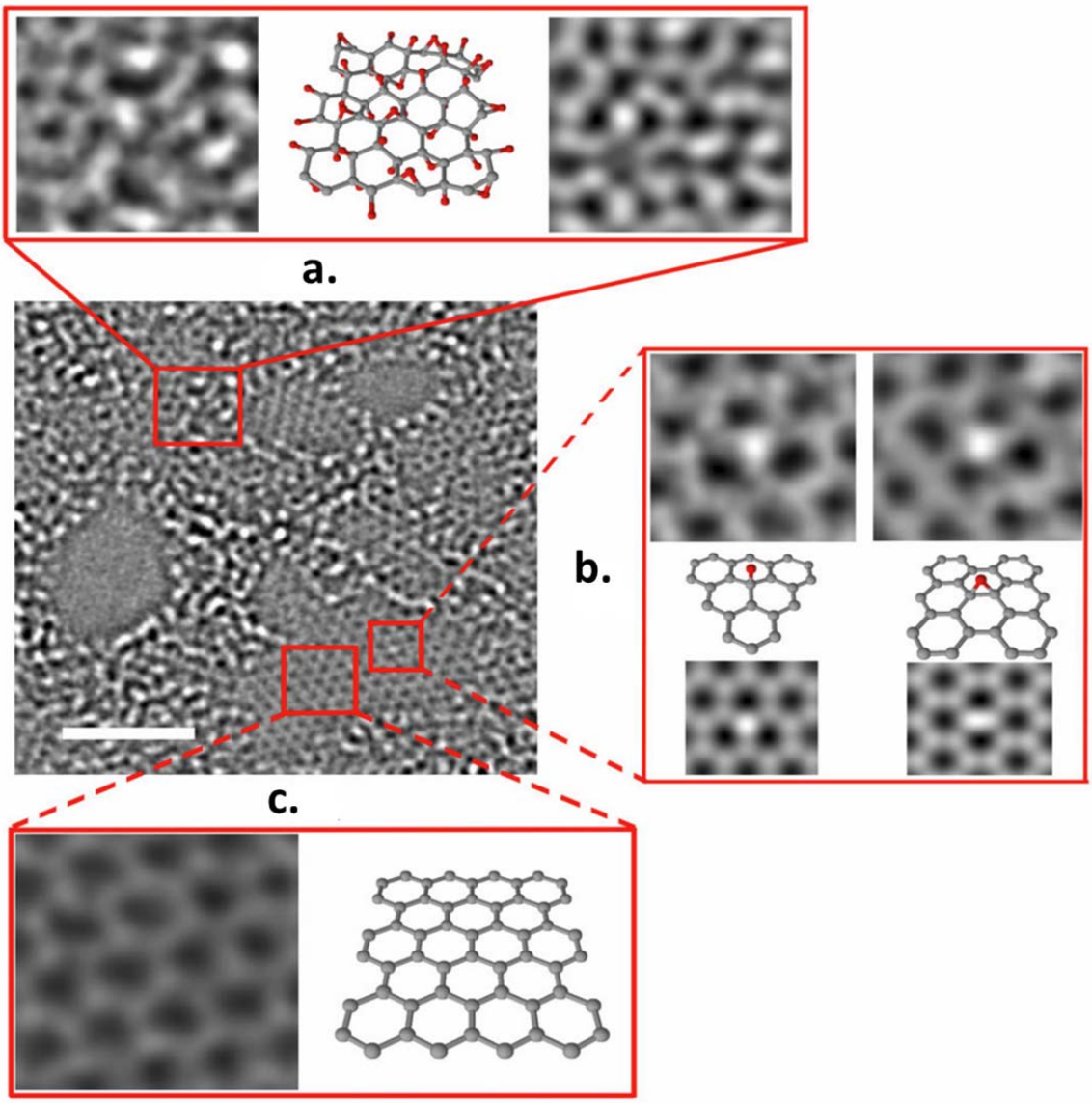

Figure 1-11. Aberration corrected TEM micrograph of a single sheet of suspended GO. The scale bar is 2 nanometers. Expansion **a.** shows, from left to right, a 1 nm^2 enlarged oxidized region of the material, then a proposed possible atomic structure of this region with carbon atoms in gray and oxygen atoms in red, and finally the average of a simulated TEM image of the proposed structure and a simulated TEM image of another structure where the position of oxidative functionalities has been changed. Expansion **b.** focuses on the white spot on the graphitic region. This spot moved along the graphitic region, but stayed stationary for 3 frames (6 seconds) at a hydroxyl position (left portion of expansion **b.**) and for 7 frames (14 seconds) at a (1,2) epoxy position (right portion of expansion **b.**). The ball-and-stick figures below the micrographs represent the proposed atomic structure for such functionalities. The simulated TEM image for the suggested structure agrees well with the TEM data. Expansion **c.** shows a 1 nm^2 graphitic portion from the exit plane wave reconstruction of a focal series of GO and the atomic structure of this region.

In the high contrast regions, oxygen atoms are present in a much higher density and greater numbers will be mobilized by the electron beam. After studying the times series, although cases of functionalities being stable for multiple seconds can be found, most functionalities seem to be mobile of the timescale of a second. Given this,

significant changes in the bonding can occur over the course of each captured frame, and each micrograph could represent multiple bonding configurations between the carbon basal plane and oxidative functionalities. Figure 1-11a shows such a region with a high degree of oxidative functionalities. A possible representative local atomic structure for this oxidized region is proposed, but of course the complicated contrast within this region makes any specific definition of a structure for this region impractical. Simulations of TEM images were made from this proposed structure and another structure where the location of the oxidative functionalities was changed, the average of which is compared to the obtained micrograph.

Figure 1-11b highlights a mostly graphitic region with isolated anomalous bright spots. The anomalies are dynamic on the timescale of a second, likely indicating isolated mobile oxygen functionalities. The anomalies of Figure 1-11b are consistent with simulations of TEM images for an oxygen resting at a hydroxyl position (left), or an oxygen resting at an (1,2) epoxy position (right). Multiple instances of such isolated functionalities are observed in GO. Although it is possible that the observed adatoms were carbon adatoms, the likelihood of mobilizing a carbon bound to the graphitic sheet or even from a nearby hole is unlikely given the multiple bonds required to be broken (with a graphene C-C bond energy of 4.9 eV)[37] compared to those required to be broken to mobilize an oxygen from common functionalities expected in GO: 2.1 eV for (1,2) epoxies and 0.7 eV for hydroxyls.[38] The mobility of these functionalities is a consequence of the incident 80keV electron bombardment, which transfers a maximum of 11.8 eV to an oxygen atom,[39] well over epoxy and hydroxyl bond energies and well over the hopping barrier, being much lower.[40] Electron beam induced bond breakage occurs, mobilizing atoms which rest at stable positions nearby on the basal plane. The energy for the ejection of an atom from the sheet is much greater.[41] For GO, we observe minimal loss of high contrast and stable hole size indicating relatively little overall beam-induced oxygen- or carbon-ejection, respectively.

Figure 1-11c highlights a graphitic region of GO. The sharpened blowup was obtained from the exit plane wave reconstructed from a 12-member focal series using the following reconstruction parameters: Electron energy: 80 keV, Spherical aberration C_{3m}= -0.014, Focus step: -0.73 nm, Focal range: +11.97 nm ... +3.94 nm, Sampling: 0.0233 nm/pixel, Focus spread: 1.2 nm, MTF at Nyquist frequency: 0.25, Semi-convergence angle: 0.1 mrad, Reconstruction limit: 0.11 nm, Two-fold astigmatism A_1: 1 nm (+37degree), Axial coma B_2: 116 nm (+30degree). The highly graphitic nature of this region is striking. Some bond strain does occur at the interface of oxidized and unoxidized regions, but the interior of the graphitic regions, when lacking oxygen functionalities, are found to be largely unaffected by this strain. The different graphitic regions can be thought of as flakes of nearly pure graphene separated by highly oxidized and thus structurally modified regions. The graphitic domains are mis-tilted in the azimuthal direction with respect to each other. This combined with bond strain at the interface of the graphitic and oxidized regions results in the observed blurring of diffraction spots compared to graphene (Figure 1-9).[42]

1.5.3.1 Detailed raGO Analysis

The structure of raGO can be better elucidated by a closer look at the electron micrographs of raGO. Figure 1-12 shows a representative image, similar to that presented in Figure 1-10c. A significant portion of raGO is indeed graphitic, but certainly raGO cannot be properly characterized as constituting "graphene". The examined raGO material was found to be overall highly sensitive to electron beam induced degradation to the point that meaningful exit plane wave reconstruction was not possible. This indicates a higher instability of raGO, as compared to graphene, or even to GO (I found, however, a significantly higher stability for bilayer raGO, as compared to monolayer raGO, as discussed below).

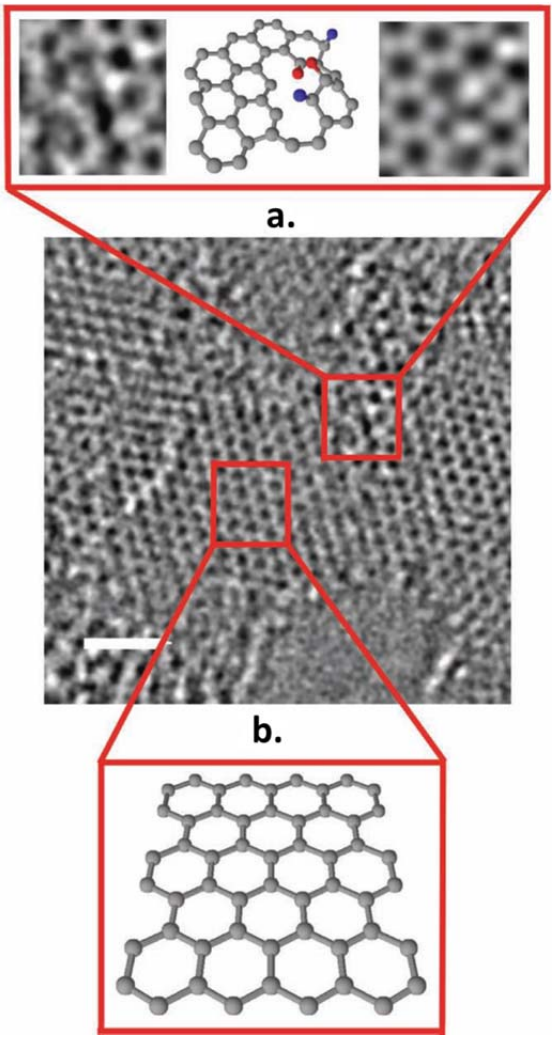

Figure 1-12. Aberration corrected TEM micrograph of a monolayer of raGO. The scale bar is 1 nanometer. Expansion **a.** shows, from left to right, an enlarged region of the micrograph, then a proposed possible structure for the region where oxygen (indicated in red) and nitrogen (blue) remain as functionalities on the sheets, and finally a simulated TEM image for this proposed structure. Expansion **b.** shows the structure of a graphitic region.

Nevertheless, the high amount of restored graphitic area in raGO supports the supposition that the parent GO contains mostly hydroxyl and epoxy functionalities. Only these oxidative functionalities (other than high energy peroxide functionalities) would result in fully restored graphitic character once reduced, as other functionalities would induce C-C bond breakage.[42] Figure 1-12a highlights regions of raGO with high contrast spots, likely representing remaining functional groups. These are understood to be either oxygen functionalities from the initial oxidation or nitrogen functionalities from the hydrazine reduction.[33] Although specific determination of a structure cannot be made, a likely structure for this region is proposed in Figure 1-12a. A simulated TEM image for the proposed structure is included for comparison. Figure 1-12b highlights a fully restored graphitic region of raGO.

1.5.3.1 GO and raGO Dynamics under Imaging Conditions

It is instructive to examine in some detail the relative temporal stability of graphene, GO, and raGO when exposed to the agitation of the imaging TEM electron beam. Under the imaging conditions, graphene is exceptionally stable, suffering only occasional knock-on damage.[41] Figure 1-13 contrasts time series images of GO, raGO, and a bi-layer of raGO. GO was seen to be stable under the beam with each of the discussed regions not changing in area percentage during the obtained time series (75 seconds) (Figure 1-13a). This indicates that although atoms may become mobile within the GO plane under electron beam irradiation, significant atom ejection does not occur, which would result in changes to these percentages, indicating degradation of the material. As discussed previously, mobile oxygen functionalities result in the shift of boundaries between the graphitic and oxidized regions as functionalities move along the basal plane. The effective motion of functionalities does not result in an averaging of these functionalities across the GO sheet, indicating mainly sp^2 or sp^3 bonding character for the most stable regions, as expected from geometrical constraints and aromaticity. It was noticed in the acquired videos that small holes (<1 nm^2 in area) which were present during the beginning of the obtained time series seemed to be closed over the course of the time series. This observation supports the notion that if a carbonaceous feedstock (in this case mobilized carbon or carbon from the limited adsorbates) is present, carbon loss from the basal plane, which occurs during the synthesis of GO, could possibly be reincorporated into the sheet under the proper experimental conditions.

The dynamics of raGO under the electron beam indicate significant degradation over relatively short time periods (Figure 1-13b). Degradation revolves around highly active regions with limited connectivity to the main raGO sheet, making them more easily accelerated under the electron. Bi-layer raGO (Figure 1-13c) shows increased stability under the electron beam, though it, too, degrades more quickly than GO or graphene.

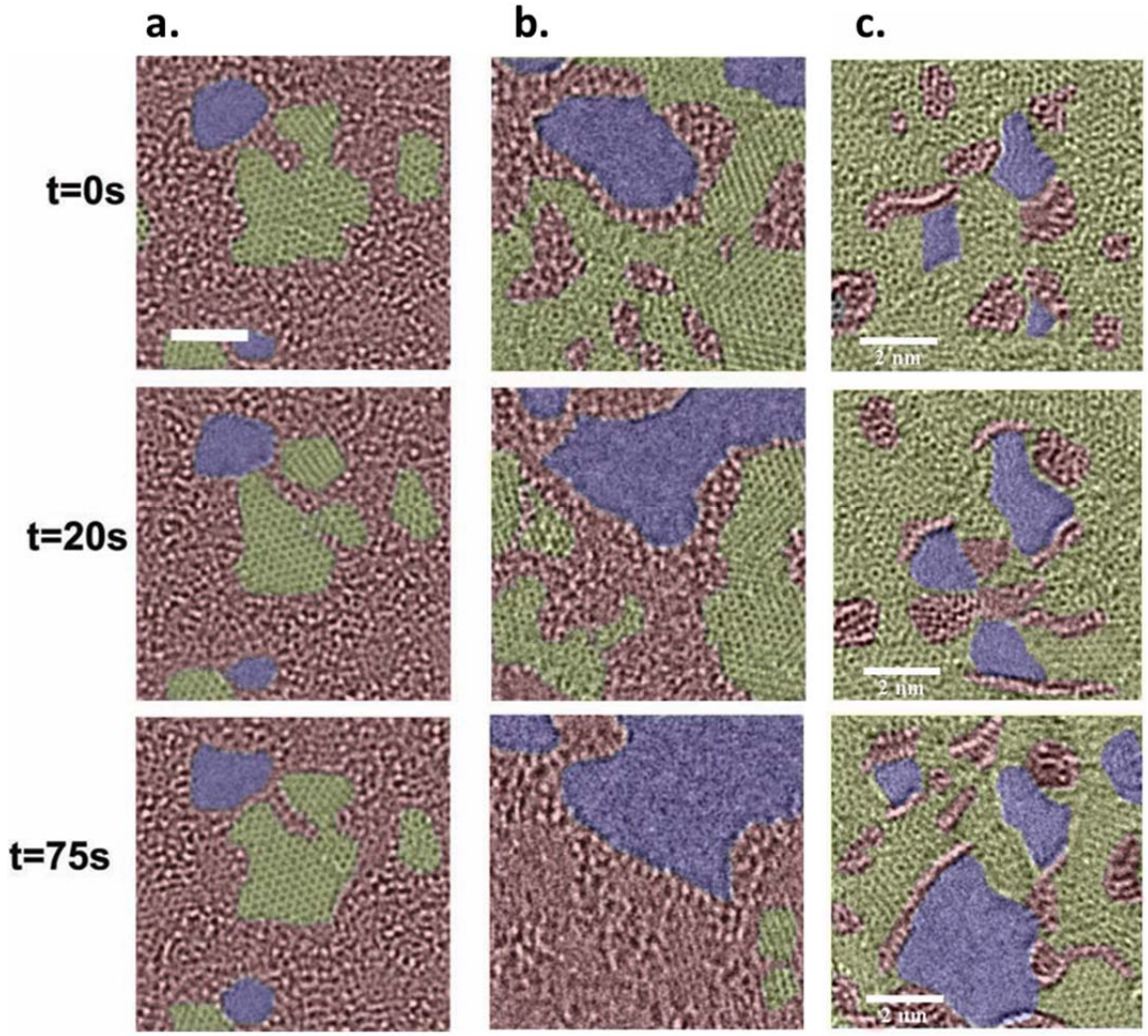

Figure 1-13. Aberration corrected micrographs of **a.** GO, **b.** raGO, and **c.** a bi-layer of raGO from acquired time series. Scale bar, indicating 2 nanometers, is valid for all micrographs. Frames show the two materialsat the indicated number of seconds. GO is seen to be overall stable with its regions changing morphology, but not overall area. raGO is seen to degrade significantly over the course of the obtained time series. The bi-layer of raGO is seen to have significantly enhanced stability compared to a single layer of raGO, but still suffers from significant electron beam induced degradation compared to even a single sheet of GO.

1.6 Structural Insights from Investigation of GO and raGO

By contrasting the previously presented images of GO and raGO, a further understanding of the functionalities of GO can be obtained. First, out of the various oxygen functionalities that have been proposed to exist in GO,[15] the main functionalities are hydroxyls and (1,2) epoxies, and carbonyls form mainly around the holes in the sheet. This is evidenced by the observed stability of hydroxyls and (1,2) epoxies and the significantly restored graphitic nature of raGO, the restoration being possible only when these functionalities are dominant. Also, since bond breakage associated with carbonyl formation likely accommodates hole formation and expansion,[43] and given XPS and FTIR evidence for these functionalities (Figures 1-5 and 1-6), carbonyls likely form at the edges of the observed holes within the GO sheet.

Our experiments greatly elucidate the important and previously controversial structure of GO. Previous attempts at experimentally determining this structure involved analyzing chemical reactivity, XPS, Raman, NMR, IR, conductivity, TGA, diffraction and absorption,[15] were relevant only to macro to microscopic regions of GO. Theoretical calculations have conversely been limited to considering regions less than 100 atoms,[14] sometimes less than 10 atoms,[38] in extent, and then generalizing a larger structure. Since regions larger than 100 atoms exist with only sp^2 or sp^3 bonding nature, these theoretical considerations are seen to poorly describe GO. Likewise, when bulk properties are generalized down to determine the most likely atomically defined structure, many nuances are overlooked. For instance, XPS results indicating carbonyls within GO have been attributed to these groups being along the microscopic edges of GO. The observation of holes, likely with edge carbonyls, every few nanometers redefines how these results should be interpreted.

Our observations and deductions about the structure of GO can be summarized as follows: 1. Graphitic regions up to 8 nm^2 remain. 2. Oxidized regions exhibit no order with regards to oxidation, have minimal sp^2 bonding character, and form a continuous network across the GO sheet. 3. Holes are present, usually under 5 nm^2. 4. Hydroxyls and (1,2) epoxies are the dominant functionalities. Carbonyls likely exist along the edges of the holes. 5. Largely unstrained sp^2 bonds exist between carbons within the core of graphitic regions. 6. Lines of graphitic or oxidized regions do not form and no superstructures are formed.

Given these deductions, theories of the structure of GO can be evaluated. Proposals for ordered functional groups or long range order, for instance lines of aromatic regions[15] or lines of oxidized regions[15, 40] are unsubstantiated. Predictions of densely oxidized regions with hydroxyls and (1,2) epoxies as the primary functionalities and carbonyls along the edges are supported,[14, 18, 42, 44, 45] whereas prediction of (1,3) epoxies,[46] carbonyls as dominant functionalities,[15] other functionalities,[17] numerous isolated functionalities,[17] or just epoxies[16] are not supported. Theories disregarding significant aromaticity[14] are likewise not supported. Theoretical considerations of less than 10 carbons[38] in GO are discarded owing to the high degree of structural inhomogeneity. Also, the proposed mechanism of "unzipping" GO sheets caused by sequential epoxies[40] is not observed. Adjacent functionalities with positions indicative of

epoxies are observed, but continuation of this defect line is not; thus the proposed microscopic cleavage of GO sheets via this mechanism is doubtful.

Given all these considerations, the structure proposed by Lerf[18] is supported, albeit with modifications. The sizes of graphitic and oxidized regions are much larger than those proposed by Lerf and with this studied GO material, holes are found throughout the sheet. These changes are represented in our proposed model for GO (Figure 14). The main differentiating feature of this model compared to the Lerf model is the large areas of the three different regions founds within GO. This is understood to be expected for GO given the nature of the oxidation employed. The extremely harsh oxidant necessary for oxidation of an otherwise highly inert material (graphite) results in initial oxidation which disrupts the local aromaticity of the basal plane which increases the reactivity of adjacent carbons towards oxidation. Essentially, once this local aromaticity is removed, oxidation can continue more readily in the surrounding region creating the observed regions of oxidation. Likewise, if the graphitic nature remains intact within a region, this portion of the GO sheet has diminished reactivity towards the oxidant as the aromaticity stabilizes it compared to already oxidized portions. Finally, following single oxidation of carbon atoms, the enhanced reactivity of these functionalized carbons will result in further oxidation and potentially full oxidation to CO_2 resulting in the observed holes within GO.

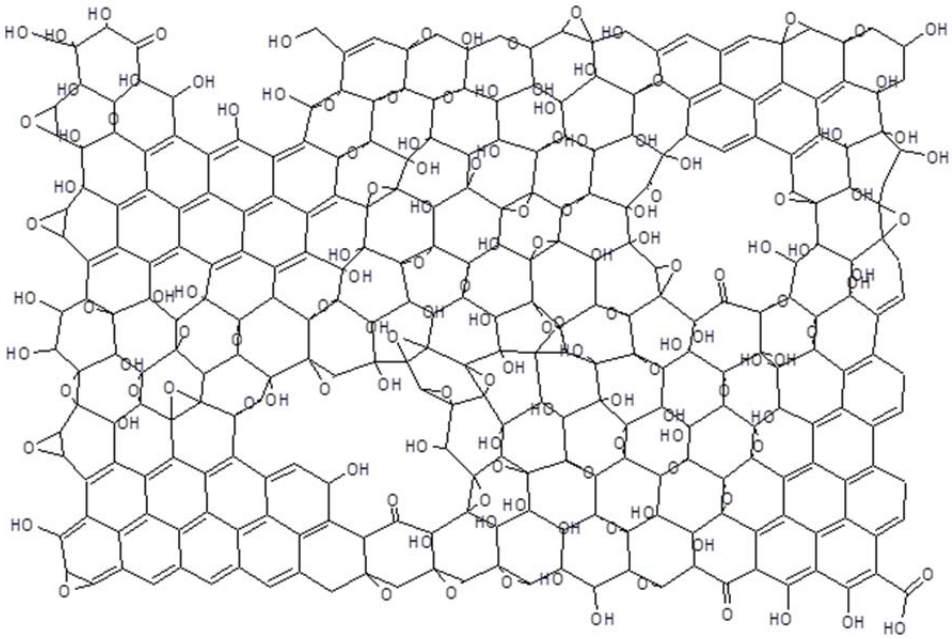

Figure 1-4. Structural model for GO proposed given the findings of the previously described study. It should be noted that the regions within this model potentially are much larger than indicated (up to many nm^2 in area for aromatic regions, oxidized regions and for holes). The major differences with this model compared to a previously proposed model[18] are the large extended regions which exist: graphitic portions, oxidized portions, and holes as well as the existence of holes within the GO sheet around which carbonyl functionalities likely exist.

1.7 Prospects for GO and raGO

Although it has been established that raGO poorly resembles graphene, it is still a material of significant interest, especially in terms of its applicability within a wide range of disciplines. It is apparent that raGO is by no means a perfect 2D crystal like graphene and the ballistic transport observed for graphene will be almost impossible to mimic with raGO, however it is a material with very high conductivity, making it suitable for a number of applications. Owing to the ease with which is can be processes, it is still of interest as a potential material for transparent electrodes,[47] for both solar cell and touch screen applications. Indeed, the increased surface area of GO and raGO makes it of particular interest for use as a chemical sensor, and in fact further increasing the surface area by steam etching the material has shown promise for the development of a high sensitivity sensor.[48]

The scalability of GO and raGO material also gives it a significant advantage over higher quality graphene syntheses like the common CVD synthesis in terms of it applicability. Significant advancements in supercapacitor[49] and battery[50] technologies have been made owing to the higher surface area of GO-based graphene material, coupled with its sufficient conductivity and its bulk producability. Finally, numerous applications within the field of advanced composites have been studied,[51] being possible owing to the superior mechanical properties that still exist even with the disordered GO and raGO structure and due to the ability to produce bulk quantities of this material. In all, although the structure of raGO is far from that of graphene, the limitations on its resultant properties given this structure are minimal depending upon the application envisioned. Therefore, until a bulk synthesis of a more structurally ideal graphene material is possible, GO-based graphene materials show significant promise in terms of its applicability, and given the enhanced surface area of this highly defective crystal, it could be an ideal form of this material for certain applications.

Chapter 2: Functionalized Carbon and Boron Nitride Nanotubes for Composite Materials

2.1 Motivation for Nanotube Composite Materials

Carbonaceous and boron nitride based nanomaterials have many impressive properties which could enhance composite materials if incorporated within them.[52] The nanotube geometry of these materials is of particular value when considering potential composite enhancement as the rigidity of a 1D material allows for a more evenly distributed filler compared to 2D fillers, presuming sufficient dispersion of the filler within the matrix material. Likewise, compared to 0D nanomaterials, 1D nanotubes are also able to better impart mechanical, electrical, and thermal enhancement given a potential for a percolation network to form within the matrix as well as allowing for properties of the filler to enhance a matrix material under the influence of strain (in the case of mechanical reinforcement).

We will begin by assessing the prospect of using carbon nanotubes (CNTs) as a filler material for enhancement of composite properties. The carbonaceous version of the this 1D nanomaterial has the benefit of being commercially available at a competitive cost as opposed to the scarcity of boron nitride nanotubes (BNNTs), even within the BNNT research community. This is largely due to the bulk of research on CNTs, which motivated significant advancement in synthetic methods for CNTs, as opposed to BNNTs which have lacked such a widespread attempt at optimizing synthetic methods. Carbon nanotubes have many impressive properties which can be partially imparted upon a host matrix or be utilized in another manner while within a composite. Among these include superior thermal and electrical conductivities as well as superphobicity.[53] Composites can therefore benefit from enhanced electrical conductivity[54] and thermal conductivity[55], as well as finding applications within the field of filtration, utilizing its superphobicity.[56] Although CNTs can be used within a wide variety of host matrices including metallic host materials,[57] the bulk of CNT composite research revolves around the enhancement of polymeric composite materials,[52] which will be the focus here.

2.2 Mechanical Reinforcement using CNTs

A useful CNT property is the superior mechanical properties of CNTs, including a high Young's Modulus (YM, or tensile modulus being the uniaxial stress versus an applied strain), on the order of 0.9 TPa,[58] and high tensile strength, on the order of 150 GPa.[58] When compared to other high strength and modulus materials, carbon nanotubes are seen to be among the most mechanically robust materials (Table 2-1), owing to the exceptional strength of the sp^2 C-C bonding within the material. Therefore, a natural application of CNTs is for mechanical reinforcement of polymeric materials, which often require superior mechanical properties and will have ever-increasing application if the mechanical properties can continue to be optimized.

Material	Tensile Strength (GPa)	Young's Modulus (GPa)
Tungsten	1.5	411
Silicon (monocrystalline)	7.0	188
Tool Steel	5.2	200
Kevlar	2.7	180
UHMWPE	8.0	222
Carbon Fiber	5.6	530
Carbon Nanotube	150	900
Boron Nitride Nanotube	33	1200
Graphene	130	1000
Diamond	60	1200

Table 2-1. Mechanical properties of mechanically robust elements, polymers and alloys, and carbonaceous and boron-nitride based materials.[5, 58-62]

However, a single property of CNTs discussed above makes the incorporation of CNTs within a host matrix with the aim of enhancing composite properties very difficult. This is the superphobicity of CNTs and other sp^2 carbon and boron nitride based nanomaterials, meaning that these materials combine both super-hydrophobicity and super-oleophobicity, having a felicity for very few materials. The dominant felicity these materials have are with other sp^2 bonded carbon and boron nitride materials, i.e. themselves. Unfortunately for the application of composite formation, this means that

attempts to synthesize composites will be greatly hindered by an inherent lack of interaction between the filler material (CNTs) and host matrix (polymer) as well as the polymer solvent system.

This lack of intermolecular interaction is even more detrimental when considering the mechanism by which a fiber material is able to reinforce a host matrix. The most general equation for strength enhancement of a fiber within a host matrix is,

$$\sigma_C = (\sigma_f - \sigma_m)V_f + \sigma_m \qquad \text{Equation 2-1}^{63}$$

Where the strength of the composite (σ_c) will be equal to the difference between the fiber strength (σ_f) and the matrix strength (σ_m) times the volume fraction of the fiber (V_f) added to the matrix strength.

This simple proportional enhancement is complicated when considering the strength of the interaction between the fiber and the host matrix yielding,

$$\sigma_C = (\tau \cdot l/D - \sigma_m)V_f + \sigma_m \qquad \text{Equation 2-2}^{63}$$

With the strength of the fiber-matrix interface (τ) moderated by the ratio of fiber length (l) to fiber diameter (D) determining the portion of reinforcement imparted upon the matrix material. Although CNTs have a very high aspect ratio of a few orders of magnitude, the non-interacting nature of a pristine CNT within a host matrix will result in a many orders of magnitude smaller interaction strength between the fiber and matrix compared to the actual strength of the CNT.

This discussion outlines the major considerations when attempting to reinforce a polymeric matrix with CNTs. One significant considering is whether CNTs are thoroughly dispersed within the polymeric matrix. Unmodified, carbon nanotubes will agglomerate given their lack of intermolecular interactions with most materials. Any potential reinforcement will be sacrificed as only the volume of CNTs homogenously dispersed within the matrix will result in mechanical reinforcement similar to that indicated by Equation 2-2. Conversely, if agglomerates of CNTs indeed do exist within the host matrix, the mechanical properties of the composite can be diminished as these voids can be a nucleation point for fracture. Indeed, work done with crudely mixing CNTs within an epoxy material greatly diminished the strength of the epoxy (Figure 2-1). Even when then CNT surface is functionalized to enhance solubility within the matrix, addition of CNTs can still result in a lower strength (Figure 2-1).

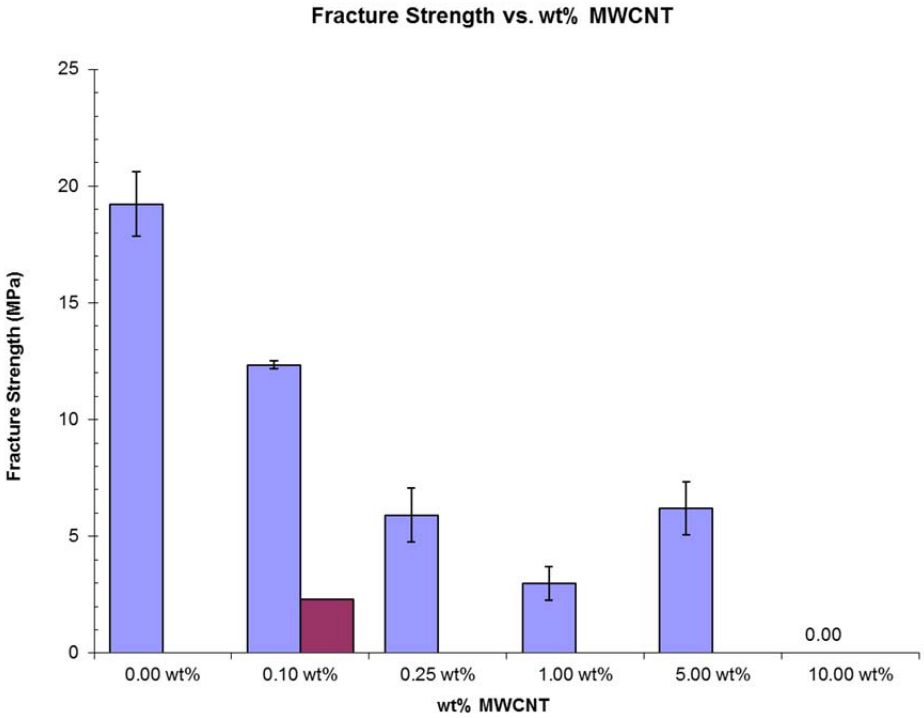

Figure 2-1. Plot of fracture strength versus wt% with associated error bars of multi-walled CNTs (MWCNT) homogenized within an epoxy matrix. The blue bars represent composites where MWCNTs were functionalized to enhance dispersion within the host matrix. The one purple bar represents a sample where the MWCNTs were not functionalized. Only the 0.10 wt% sample was mechanical robust enough for testing. Other non-functionalized MWCNT samples failed before testing was possible. Of the functionalized MWCNT composite samples, the 10 wt% sample also failed before testing was possible. Results from and courtesy of Prof. Rob Ritchie and Joe Lemberg under a collaborative effort whereupon synthesis was done in the Zettl labs and mechanical testing within the Ritchie labs.

The other major consideration which must be made is the interfacial stress that can be transferred from the host matrix to the fiber filler, τ from Equation 2-2. Not only must the CNT fibers be well dispersed within the matrix, the matrix must bond with the CNT such that stress can be transferred while the composite is under stress. If this interaction is limited to weak Van-der-Waals type interactions, pull-out of the fiber will easily occur and the enhancement to the strength will be minimal. However, if covalent bonding with the host matrix is possible, or if sufficiently strong intermolecular interaction is achieved, then the stress transferred may be sufficient to allow for a reinforcement of the matrix.

2.3 General Route for the Covalent Attachment of Moieties onto MWCNTs

Great consideration must be made to maximize both dispersion of CNTs within the polymeric solvent system and resultant composite material as well as maximizing the interaction between CNTs and the host polymer at the interface of these materials. The best approach for achieving both dispersion and maximizing the fiber-matrix interaction is to covalently functionalize the CNT. It should be noted at this point that only MWCNT can be functionalized in the manner to be described as SWCNTs will completely degrade under the reaction conditions heretofore specified and generally SWCNT have proven more difficult to functionalize.

First, a chemical handle is created off the MWCNT such that subsequently a variety of further chemical groups can be attached. These chemical groups can then be chosen such that the interaction with a chosen host polymer can be maximized. A general method for dictating the exposed chemical nature of a MWCNT is outlined in Scheme 2-1.

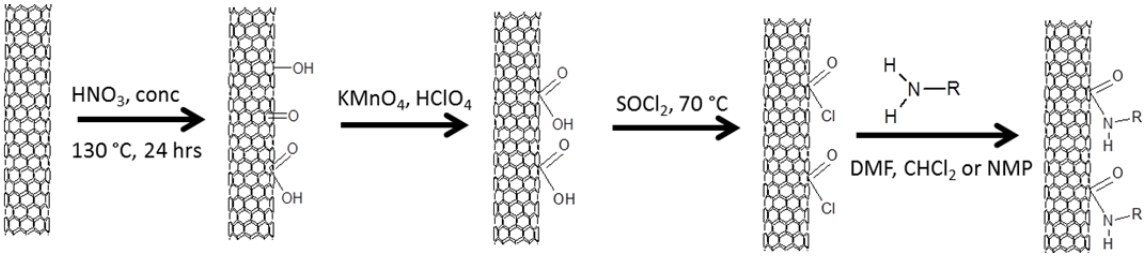

Scheme 2-1. General method for the functionalization of MWCNTs. Initial oxidation imparts hydroxyl, carbonyl, and carboxylic acid functionalities. Further oxidation converts all functionalities to carboxylic acid groups, which can then be converted to acid chloride functionalities via $SOCl_2$ treatment. Finally, amide formation is achieved in the proper solvent given the "R" group desired to be exposed off the functionalized MWCNT.

Briefly, MWNTs (1 g) were added to concentrated nitric acid (70%, 1 L) and sonicated for 15 min to disperse the material. The suspended MWCNT solution was refluxed at 130 °C for 12 hr. The suspension was allowed to cool and then filtered using a membrane filtration apparatus in conjunction with a polycarbonate filter (0.2 μm pore size), and washed thoroughly with DI water (6 L). MWCNTs were then dispersed into DI water (1 L), to which KMnO4 (3 g) was added under vigorous stirring. After cooling to 5 °C, the solution was acidified with the addition of $HClO_4$. After acidification, the solution was allowed to warm to room temperature and quenched with excess citric acid monohydrate (60 g), accompanied by a color change from deep purple to clear. The MWCNT were then filtered as previously described and washed with excess DI water (6 L). At this point, carboxylic acid functionalities are present on the MWCNT, which can be readily dispersed under mild sonication in water.

For acid chloride functionalities, the carboxylic acid functionalized MWCNT were dried under vacuum for 24 hrs. Thionyl chloride (400 mL) was used as the solvent and reactant, being added to the functionalized MWCNT and sonicated (15 min) to

disperse the MWCNTs. This suspension was heated to 70 °C in a N_2 atmosphere and vigorously stirred for 24 hrs. This converts the carboxylic acid functionality to an acid chloride functionality. $SOCl_2$ was then carefully removed by rotary evaporation equipped with a liquid N_2 trap and dried to completion using a Schlenk apparatus (~6 hrs.).

Finally, attachment of an amine terminated arbitrary alkyl-chain is accomplished by choosing the solvent system proper for solubilizing the chosen amine. This dry solvent with 5 mmol of the desired amine is used to disperse the acid chloride functionalized MWCNTs using sonication (15 min.), with 5 fold weight excess of the amine compared to the MWCNTs. The solution is warmed to ~50 °C (depending on the solvent system chosen) and vigorously stirred for 24 hrs with intermittent sonication to enhance dispersion during the reaction. The functionalized MWCNT are then filtered using the previously described filtration apparatus, but instead using an anodized aluminum filter (0.2 μm pore size) and typically rinsed with 1 L of the utilized solvent followed by 1 L of ethanol.

Using this approach, most any "R" alkyl group can be attached which is selected with consideration of the eventual host polymer. Indeed, sequential attachment of moieties can also be achieved by iterations of the amide formation via the acid chloride and amine reaction outlined in this scheme. Furthermore, this approach produces large numbers of functionalities upon the outer wall of the MWCNTs such that the exposed chemical nature of the MWCNT becomes well defined by the functional group attached.[64]

2.4 MWCNTs Incorporated with Kevlar Composites

Using the general approach for MWCNT functionalization outlined above, being necessary for proper composite formation, we look at the potential enhancement of an already mechanically robust polymer, Kevlar. Kevlar is a well-known polymer with exceptional stiffness and strength (Table 2-1), and the uses of Kevlar all revolve around these superior mechanical properties. Further enhancement of the mechanical properties of Kevlar would make it more useful in its current applications and perhaps allow for further applications to be considered. Kevlar is synthesized through a condensation polymerization route common for poly-amides with terephthaloyl chloride (TPC) condensing with p-phenylenediamine (PDA) to form a poly-aramide. The strength of the Kevlar fiber comes from the strong interaction between polymeric chains with strong hydrogen bonding and pi-pi stacking occurring between adjacent chains (Figure 2-2). In fact, Kevlar forms a liquid crystal in a proper solvent such as concentrated sulfuric acid. If this interaction can be mimicked off the sidewalls of a MWCNT, then the strong intermolecular interactions found in Kevlar can allow for an interface with strong interactions. Ideally then, MWCNT incorporation within the Kevlar matrix will result in a high aspect ratio filler with strong interaction with the host matrix yielding a composite material with mechanical properties superior to that of the basic Kevlar polymer.

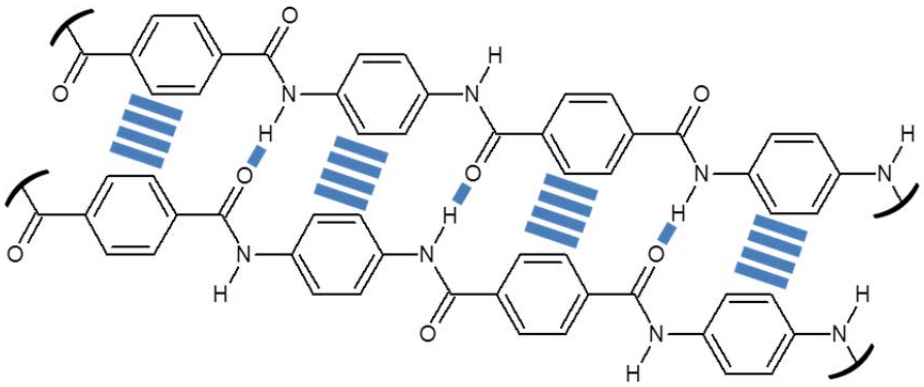

Figure 2-2. Two chains of Kevlar which display the pi-pi interaction between phenyl groups (groups of 4 wide blue lines) and the hydrogen bonding occurring between different portions of the amide groups (single blue lines).

2.4.1 Sequential Attachment of Kevlar Monomeric Units

Such that advanced composites of MWCNTs within a Kevlar matrix could eventually be synthesized, the thorough characterization of MWCNT functionalized with monomeric units of Kevlar and their incorporation within basic Kevlar polymeric systems was undertaken.[65] To demonstrate the ability to attach arbitrary numbers of monomer units, sequential functionalization of MWCNTs with TPC and PDA was done, with 1.5 monomeric units being attached (PDA-TPC-PDA) to the outer walls of MWCNTs.

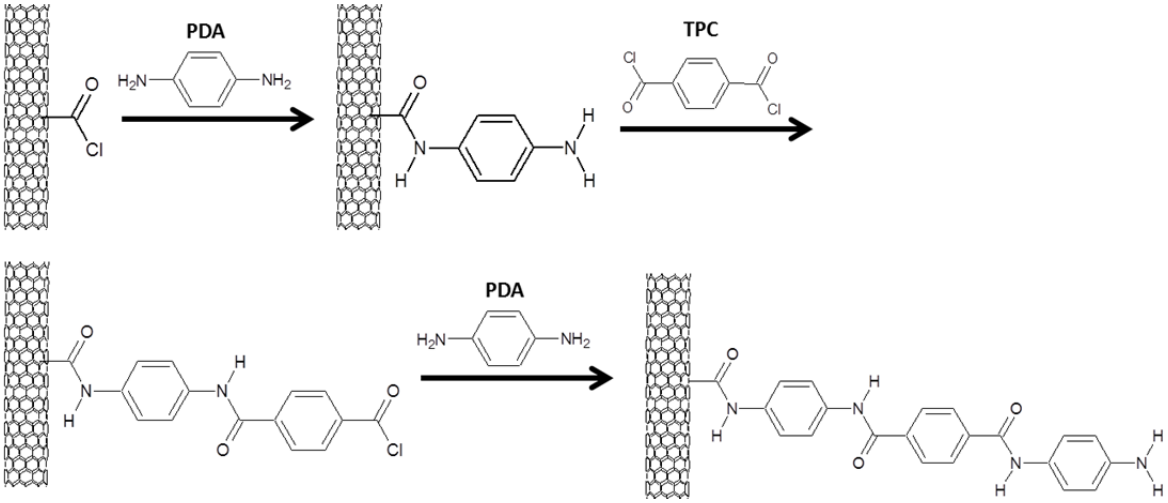

Scheme 2-2. Acid chloride functionalized MWCNTs (Scheme 2-1) are iteratively functionalized with PDA, then TPC, then PDA to obtain MWCNTs with 1.5 monomeric units of Kevlar covalently attached to the sidewalls of the MWCNT.

As indicated in Scheme 2-2, PDA-functionalized MWNTs (PDA-MWNTs) were synthesized by creating a solution of p-phenylenediamine(PDA) (0.50 g, 4.62 mmol) in N-methyl-2-pyrrolidone (NMP) (anhydrous) (200 mL) with acid chloride functionalized MWCNTs (COCl-MWCNT) (see Scheme 2-1) (0.100 g). The solution was sonicated (15 min) to allow the complete dispersion of the MWNTs in the PDA solution. The suspension was heated to 50 °C to promote optimum dispersion and exfoliation of the COCl-MWCNTs within the solution and to promote the coupling of PDA at the surface of the COCl-MWCNTs via amide formation. The appearance of the suspended material at this stage resembled a rich black oil-like material, giving preliminary indication to a favorable dispersion and reaction of the COCl-MWNTs in the suspension. The suspension was allowed stir for 12 hr, throughout which intermittent sonication (5 min at 2 hr intervals) was performed in order to ensure optimum dispersion of materials. PDA-MWNTs were then recovered by filtration (as described above) and were washed thoroughly with NMP (500 mL), ethanol (500 mL), and methanol (500 mL) to ensure complete removal of excess PDA.

For the modification of PDA-MWNTs with TPC to form TPC-PDA-MWNTs, a solution of TPC (0.938 g, 4.62 mmol) in NMP (anhydrous) was added to PDA-MWNTs (0.100 g) which had been dried using a Schlenk line (6hr). The PDA-MWNTs were sonicated (15 min) into suspension, and the material heated to 50 °C under magnetic stirring for 12 hr to facilitate the covalent coupling of TPC to PDA-amino groups at the surface of the PDA-MWNTs (intermittent sonication, 5 min, every 2 hr). The TPC-PDA-MWNT material was filtered (as described above) and was thoroughly washed with NMP (anhydrous) (1.5 L) to allow removal of unreacted TPC.

For final attachment of PDA, the TPC-PDA-MWNTs were immediately transferred to a round-bottomed flask by sonicating the material off the Teflon filter membrane using NMP (30 mL). Modification of TPC-PDA-MWNTs with PDA to form PDA-TPC-PDA-MWNTs was done by creating a solution of PDA (0.50 g, 4.62 mmol) in NMP (anhydrous) (200 mL), which was added to TPC-PDA-MWNTs (0.100 g). The material was sonicated (10 min) to ensure adequate dispersion of the MWNTs and resembled a rich black suspension as before. The suspension was heated to 50 °C and allowed to stir for 12 h, with intermittent sonication (5 min, every 2 h). The PDA-TPC-PDA-MWNTs were filtered and washed with NMP (500 mL), ethanol (500 mL), and methanol (500 mL) to ensure complete removal of excess PDA. As material which has been allow to form a cake on top of a filter membrane has the potential to trap unreacted materials, the material was redispersed in methanol (1 L) and filtered once more followed by washing with methanol (1 L). PDA-TPC-PDA-MWNTs were recovered from the filter and dried on a Schlenk line (6 hr) before use.

2.4.2 FTIR Analysis of Kevlar Attachment to MWCNTs

Characterization of the sequential attachment of these moieties can be done by using IR spectroscopy (Figure 2-3). Initially, pristine MWCNTs are very IR inactive in the range shown, but the spectrum for PDA-MWCNTs clearly indicates the covalent attachment of the PDA molecule. The broad band at 1631 cm^{-1} with a shoulder at 1640 cm^{-1} is from a combination of the N-H bend of the free amino group and the amide C═O

absorption. The broad band at 1570 cm^{-1} is attributed to the amide II N-H absorption, while the band at 1508 cm^{-1} indicates the C=C absorption of the aromatic ring. The appearance of these bands and the fact that N-H bands are present due to both amine and amide groups give firm evidence for the covalent attachment of PDA molecules at the surface of the MWNTs.

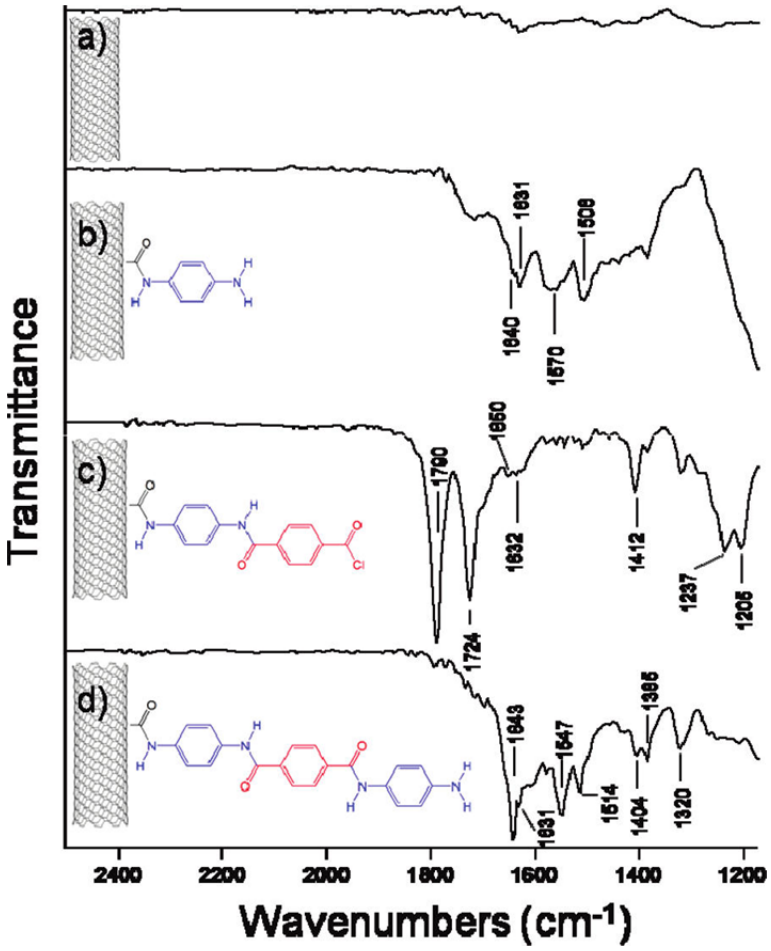

Figure 2-3. FTIR spectra of **a.** pristine MWCNT **b.** PDA-MWCNTs **c.** TPC-PDA-MWCNTs and **d.** PDA-TPC-PDA-MWCNTs.

Following subsequent coupling of TPC to PDA terminal amino groups via amide formation, TPC-MWNTs were characterized. The appearance of intense bands at 1790 and 1724 cm^{-1} are indicative of the C=O of an acid chloride in both free and hydrogen bound states (Figure 2-3c). Bands at 1650 and 1632 cm^{-1} are due to the amide I C=O stretch and the amide II N-H bend, respectively. The aromatic C=C stretching band is found at 1412 cm^{-1}, whereas two equivalent bands at 1237 and 1205 cm^{-1} are indicative of the two forms of *p*-disubstituted benzene rings which collectively support the assertion of the covalent modification of PDA-MWNTs with TPC to form TPC-PDA-MWNTs.

Further coupling of PDA to the terminal acid chloride groups of the TPC-PDA-MWNTs was performed. In contrast to the spectrum of the TPC-PDA-MWNTs

(Figure 2-2c), where the C═O stretch of the acid chloride groups appear as intense bands, in the case of PDA-TPC-PDA-MWNTs (Figure 2-2d), these bands are absent and have been replaced by the sharp amide I C═O absorption at 1643 cm^{-1} with a shoulder at 1631 cm^{-1} of the amide II N-H absorption. The N-H bend of the terminal amino group of the PDA molecule is seen at 1547 cm^{-1}, whereas the sharp absorption of the aromatic C═C stretching is seen at 1514 cm^{-1}. Bands at 1404 and 1385 cm^{-1} are due to the aromatic C-H bend, whereas a band at 1320 cm^{-1} is due to the phenyl C-N stretch. Notably, the amide I band has increased in intensity as might be expected because of both the presence of additional amide functional groups and the increased vibrational freedom of molecules subsequently bound to the surface of MWNTs. This effect is well-known in the case of ligands bound to the substrates and nanoparticles, where groups α to the surface are often weak or indistinguishable, whereas ω groups are typically well-defined.[66]

2.4.3 Creation of Kevlar-MWCNT Composites

Composites can be made of the Kevlar-monomer functionalized MWCNTs to exhibit the favorable interaction with the functionalized MWCNTs and the host matrix, Kevlar. Briefly, preparation of Kevlar/pristine-MWNT (p-MWCNT) and Kevlar/ PDA-TPC-PDA-MWNT were done as follows. The polycondensation between TPC and PDA to form Kevlar, was carried out in the presence of MWNTs to result in 1 wt % MWNT-impregnated Kevlar composites. For comparative purposes, composites of Kevlar with pristine as-received MWNTs (p-MWNTs), denoted Kevlar/p-MWNTs, and Kevlar with PDA-TPC-PDA-MWNTs (PTP-MWNTs), denoted Kevlar/PTP-MWNTs, were prepared.

PDA (5.28 g, 49 mmol) was dissolved in NMP (50 mL), and the solution cooled to 3 °C under magnetic stirring. MWNTs (either p-MWNTs or PTP-MWNTs, 0.100 g) were added to the stirring solution and sonicated (10 min) to ensure dispersion of the material. A solution of TPC (9.92 g, 49 mmol) in NMP was added to the stirring MWNTs/PDA solution. This resulted in the immediate formation of the polymer Kevlar, evidenced by the formation of a paste-like opaque yellow-green material. The material was filtered using membrane filtration equipment, and was washed by NMP (500 mL) and methanol (500 mL) to ensure removal of the reaction byproduct, HCl. The resultant material was vacuum-dried using Schlenk apparatus (6 h) and yielded ~10 g of MWNT impregnated-Kevlar.

2.4.4 Analysis of Kevlar-MWCNT Composites

Since PTP-MWNTs possess surface chemistry identical to that of the Kevlar host matrix, it was expected that the PTP-MWNTs would be well integrated within the Kevlar composite. Alternatively, p-MWNTs, possessing little or no surface functionality, are expected to aggregate among themselves and form insoluble nanotube regions within the Kevlar matrix.

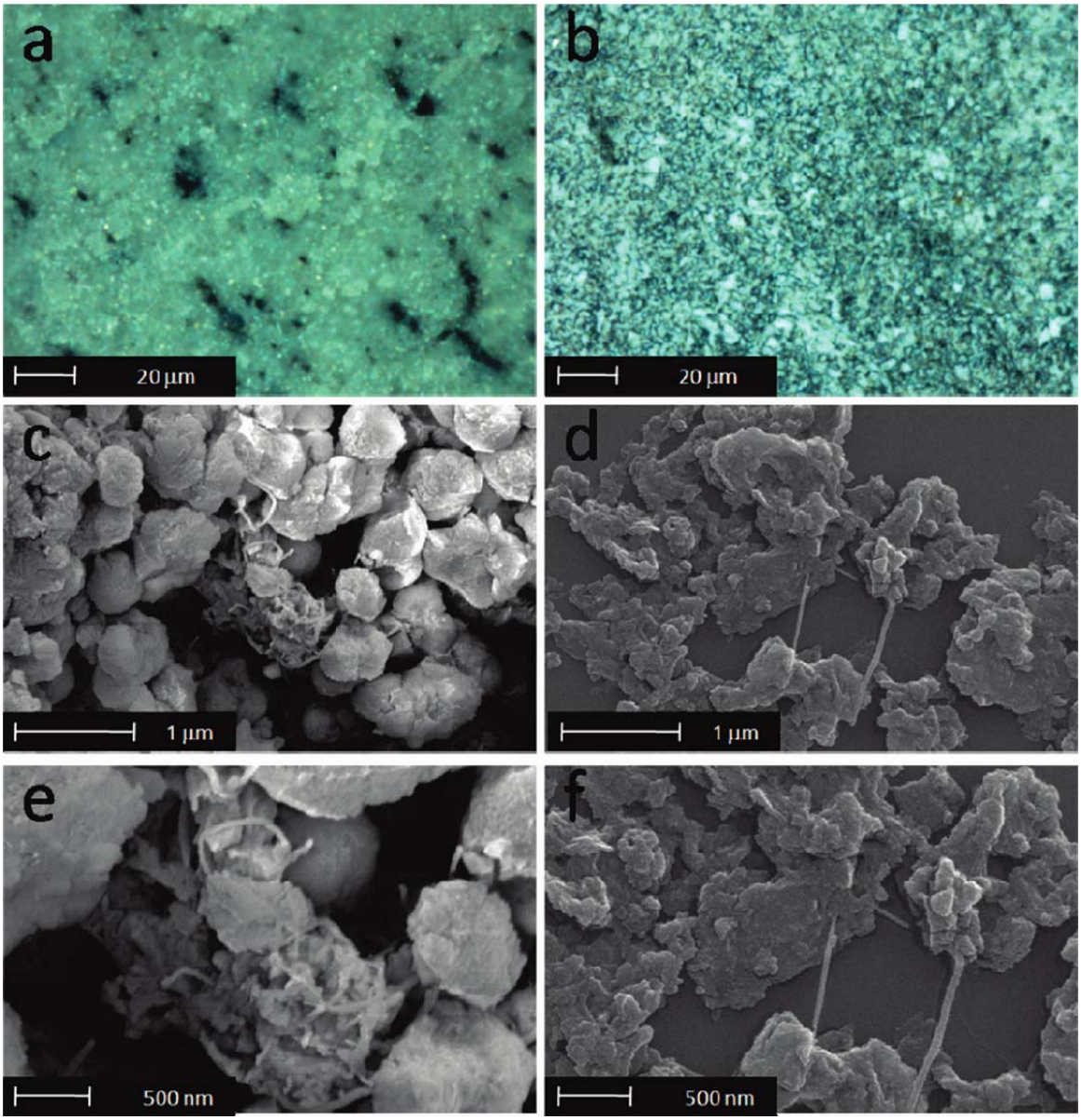

Figure 2-4. Optical images of **a.** p-MWCNT/Kevlar and **b.** PTP-MWCNT/Kevlar as well as SEM Micrographs of **c,e.** p-MWCNT/Kevlar and **d,f.** PTP-MWCNT/Kevlar.

Optical images of the composites indicated distinct differences between the materials (Figure 2-4a,b). Kevlar is opaque yellow in color, whereas the composites of p-MWNTs/Kevlar and PTP-MWNTs/Kevlar were gray and olive-green in color, respectively. The fact that the materials were markedly different in appearance gave some preliminary indication that the MWNTs had been distributed differently within the polymer matrix. Optical images of the p-MWNTs/Kevlar and PTP-MWNTs/Kevlar composites at 500X magnification show macroscopic aggregates of MWNTs in the case of the p-MWNTs (black regions in Figure 2-4a), which were absent in the case of the PTP-MWNTs (Figure 2-4b).

SEM images of the materials deposited onto a piece of silicon wafer indicated that large aggregates of MWNTs existed on top of large Kevlar regions in the case of the

p-MWNTs (Figure 2-4c). While in the case of the PTP-MWCNTs, individual MWNTs were observed to be embedded within the Kevlar matrix, and were not found as aggregates within the material (Figure 2-4d). The entire morphology of the samples was notably different as can be seen from the SEM images. I speculate that in the case of the p-MWNTs, Kevlar was formed independently from the MWNTs that were present. In the case of the PTP-MWNTs, PTP-MWNTs were found to be embedded within the Kevlar matrix that exhibits markedly different grain size and morphology because of the size regime of the MWNTs that the PPTA had formed around. Images e and f in Figure 2-4 show the materials at higher magnification, which clearly shows the p-MWNT aggregates in the case of the p-MWNTs/Kevlar (e) and individual PTP-MWNTs protruding from within sheets of the Kevlar material (f).We hypothesize that in the latter case, this is possible because of the intrinsic interaction between the materials on account of their identical surface chemistry.

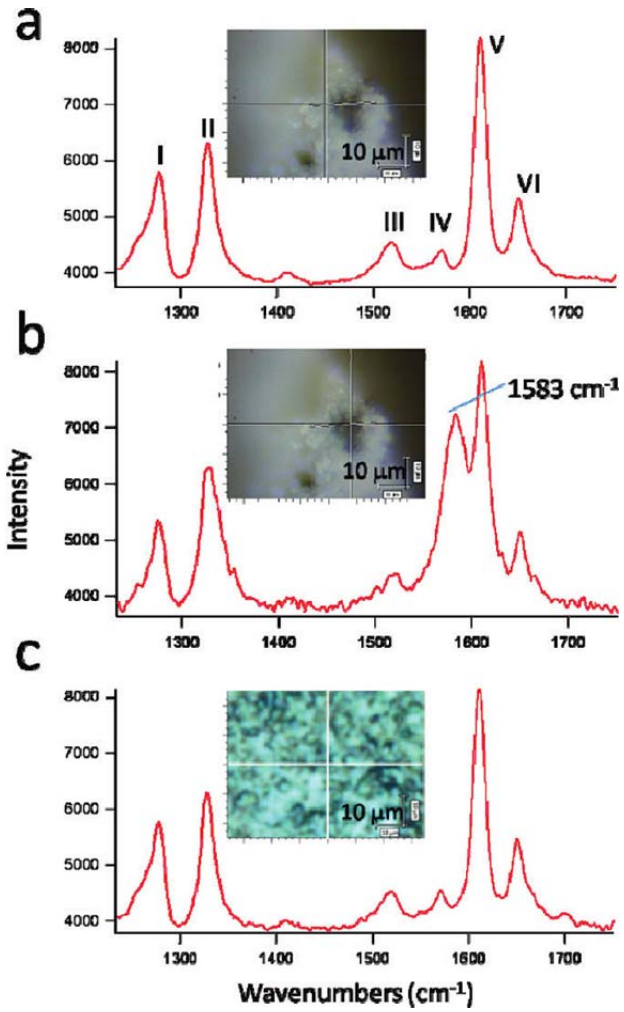

Figure 2-5. Raman spectra with optical insets of **a.** a Kevlar region within the p-MWNTs/Kevlar composite, **b.** an aggregate of p-MWNTs within the p-MWNTs/Kevlar composite, **c.** a representative area of the PTP-MWNT/Kevlar composite.

Raman mapping of the composite materials was also used to spectroscopically identify the regions in the MWNTs/Kevlar composites using a laser with λ= 514.5 nm. In the case of the p-MWNT/Kevlar composite, Figure 2-5a shows the Raman bands corresponding to a region of Kevlar material, as indicated by the optical image in the inset. The bands labeled I-VI correspond exactly with values reported in the literature for Kevlar.[67] Figure 2-5b shows the bands corresponding to an aggregate of p-MWNTs within the Kevlar matrix, as shown in the inset. Clearly evident is the appearance of a band at 1583 cm^{-1}, which is identified at the G-band characteristic of MWNTs. Such regions were indistinguishable in the case of the PTP-MWNTs/Kevlar material, whose spectrum was dominated by the Kevlar bands, Figure 2-5c. It is indeed gratifying that bands due to MWNTs are not observed in this latter case, corresponding with good integration and dispersion of MWNTs within the PPTA matrix.

These results well establish the case that with unmodified MWCNTs, dispersion within a Kevlar matrix host is not accomplished during polymer formation whereas with MWCNTs which have been covalently modified with monomeric units of host polymer, individual MWCNTs can been found well dispersed within the host matrix. The high degree of functionalization obtained through this approach seems to change the surface chemistry of the MWCNT such that facile dispersion within the host matrix is possible. Further attempts to directly covalently attach MWCNTs to the host Kevlar matrix can easily be envisioned, but even without covalent attachment to Kevlar polymeric chains, the strong intermolecular interactions present within Kevlar will still be present between a non-covalently bound PTP-MWCNT and the surrounding Kevlar material.

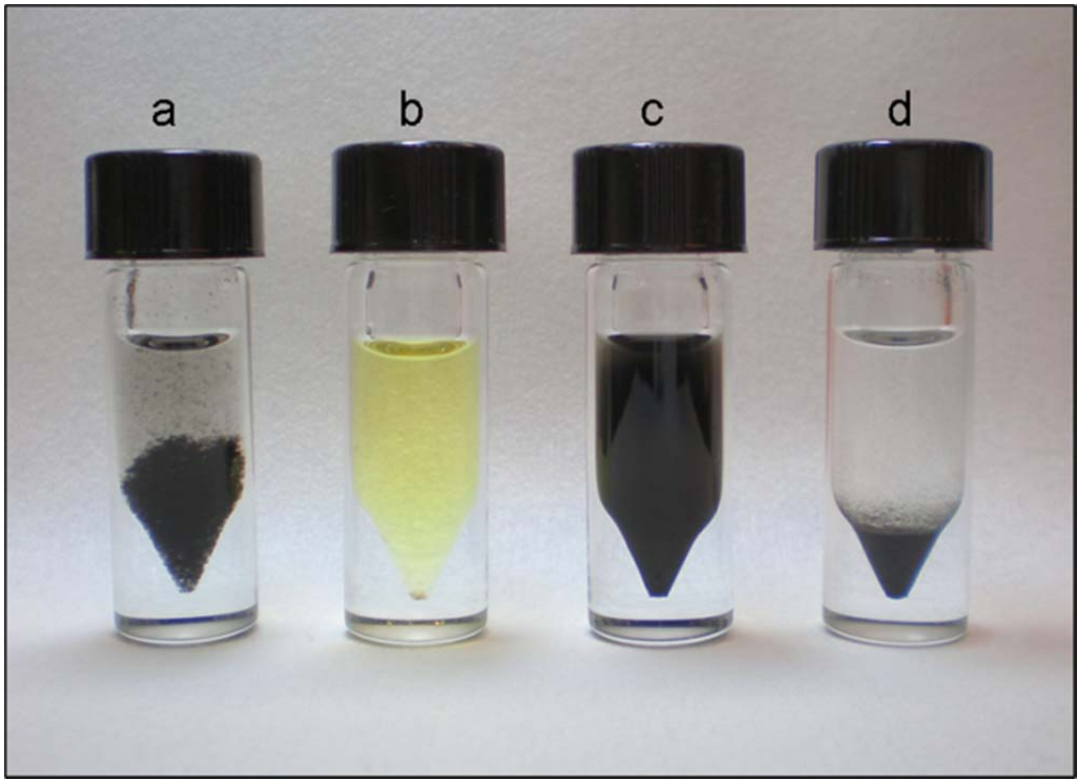

Figure 2-6. Vials containing **a.** unmodified-MWNTs, **b.** Kevlar trimer **c.** Kevlar trimer-MWNTs and **d.** cross-linked Kevlar trimer-MWNTs, all in DMF.

The potential for incorporation within a Kevlar matrix is further indicated with the following qualitative solubility experiment. Although pristine MWCNT (Figure 2-6a) are not soluble within DMF, a trimer of Kevlar (Figure 2-6b), which is soluble in DMF, upon covalent bonding to functionalized MWCNTs will draw the Kevlar trimer-MWCNT into DMF solution (Figure 2-6c). However, upon addition of TPC to the solution, the Kevlar trimer-MWCNT become cross linked and insoluble in DMF (Figure 2-6d). This qualitatively shows the cross-linking which occurs when very small Kevlar chains are made, likely linking MWCNTs together through their covalent functionalities and drawing them out of solution due to the highly cross-linked material that is formed. This furthers the argument that Kevlar functionalized MWCNTs will directly bond to a Kevlar matrix when added in situ during polymerization.

2.4.5 Kevlar-MWCNT Study Assessment

With the study undertaken, the important feature of a well dispersed fiber within the host matrix were demonstrated, and the other important parameter of having high interfacial stress transfer between the fiber and matrix should certainly be greatly enhanced through either direct covalent attachment of the MWCNT to polymeric chains or through strong intermolecular interactions between the polymer and identical monomeric units covalently attached to the MWCNT.

This study was a new type of approach to MWCNT-polymer composites as previous studies often times would involve crude mixing of unmodified-MWCNTs with the solvent system and host polymer or attempt to enhance interaction between the MWCNTs and the polymer but fail to fully take into consideration the aims of functionalization and combine this with proper characterization.

2.5 MWCNT Nanoparticle Hybrids

Another promising use for functionalized MWCNTs is to covalently attach metal nanoparticles (NPs) for a complex nano-hybrid of nanoparticle-decorated-MWCNTs. These hybrids show great promise for use as efficient catalytic systems[68] where loss of high surface area catalytic nanoparticles is diminished when used in a continuous flow reactor system. They can also be of interest for hydrogen storage materials given the spillover mechanism which can be facilitated when Pt or Pd can atomize molecular H_2 on the particle surface which then "spills-over" onto a material that otherwise would only weakly bind H_2 but not atomic hydrogen, like CNTs or BNNTs.[69]

For these systems to be effective, covalent attachment of the metal nanoparticle must be achieved such that simple rinsing does not remove the nanoparticles in the case of catalysis or the nanoparticle is within range for the spillover mechanism to occur in the case of the hydrogen storage material. Looking back to Scheme 2-1, it can be understood that a properly chosen "R" group could potentially allow for covalent attachment of a nanoparticle to a nanotube. It is well known that noble metals bind strongly to thiol groups, and indeed long alkyl-chain thiol ligands are common for stabilizing nobel metal nanoparticles.[70] Therefore, if the "R" group were a long chain thiol, then a nanoparticle could covalently attach to the MWCNT.

The final consideration is that colloidal techniques for synthesizing nanoparticles, a ligand must stabilize the nanoparticle from further aggregation.[71] However, if the attached ligand is too strongly bound, then displacement of the ligand necessary for synthesis with the functionality attached to the MWCNT may not be possible. Syntheses of nanoparticles with a weakly bound ligand are not common as stronger ligands are much more favorable, given the long-term stability of nanoparticles with more strongly bound ligands, however 4-dimethylaminopyridine (DMAP) has been shown to be a ligand which properly stabilizes noble metal NPs, but is very weakly attached such that displacement by the functionality off the MWCNT could occur.[72]

2.5.1 DMAP Pd NPs Attached to MWCNTs

To obtain nanoparticles sufficient for attachment to a MWCNT, DMAP stabilized Palladium nanoparticles (DMAP-PdNP) were synthesized using previously reported procedures.[72] Acid chloride functionalized MWCNTs (Figure 2-7) are reacted with mercapto-dodecylamine (mDDA) by dispersing COCl-MWCNTs (1 g) in dry

dichloromethane (1 L) with mDDA (4 g) under sonication (15 min.). This solution was vigorously stirred for 24 hrs with intermittent sonication. This solution was then filtered using an anodized aluminum filter (0.2 μm), rinsed with dichloromethane (1 L) and ethanol (1 L). mDDA-functionalized MWCNTs (1 mg) were then dispersed in water (1 mL) to which was added excess DMAP-PdNPs (5 μL aqueous solution). This solution was allowed to settle for 2 days without disruption. The solution turns from a brownish color (from the DMAP-PdNPs) to a much more clear solution over the course of a few hours. This solution is then diluted with water and centrifuged to crash out the nanotube material. After collecting the pellet and allowing it to dry, the material is dispersed in IPA through mechanical shaking. This solution is spotted onto a TEM grid for analysis.

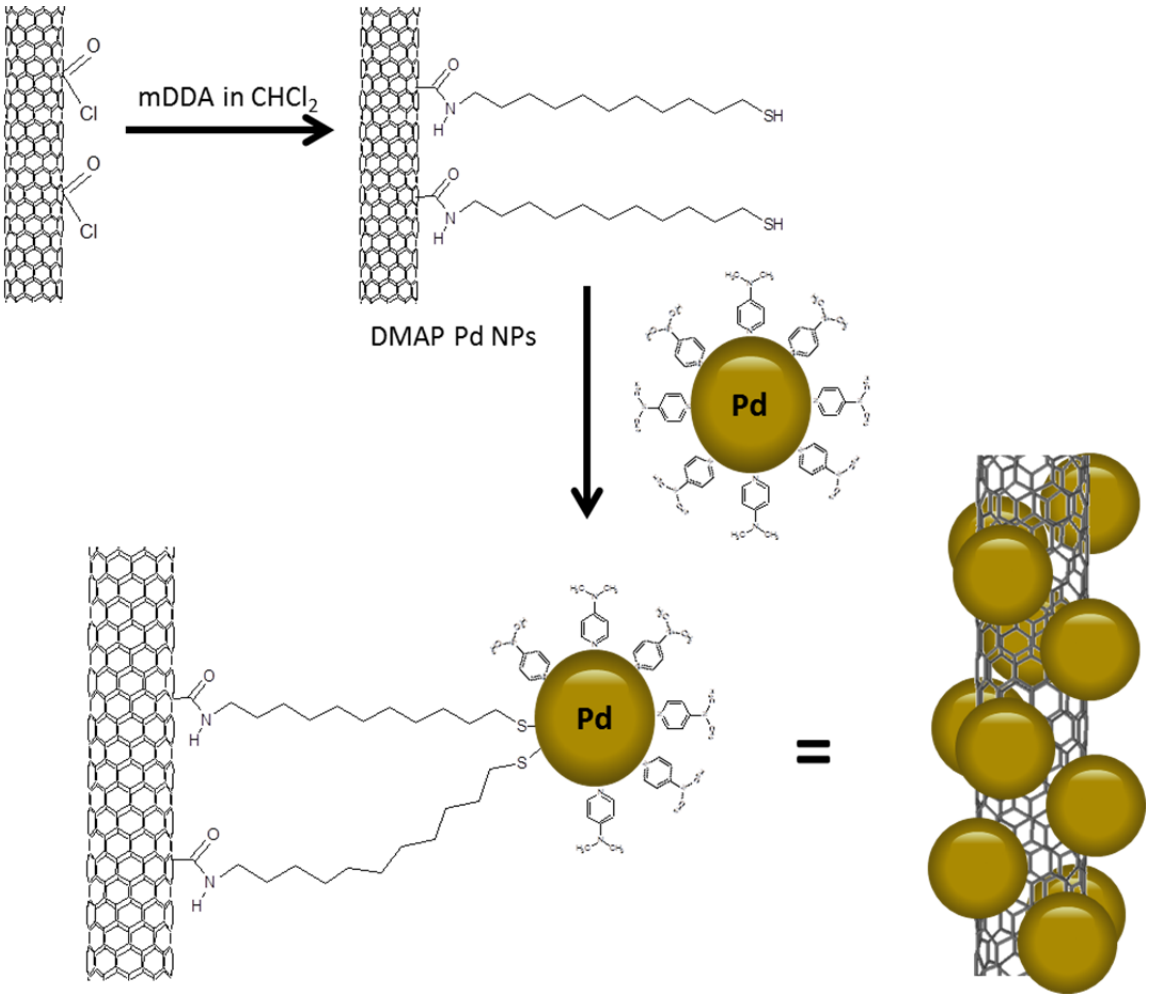

Figure 2-7 Acid chloride functionalized MWCNTs are further functionalized with mercapto-dodecylamine (mDDA) and subsequently reacted with DMAP-PdNPs to form a MWCNT-PdNP hybrid material.

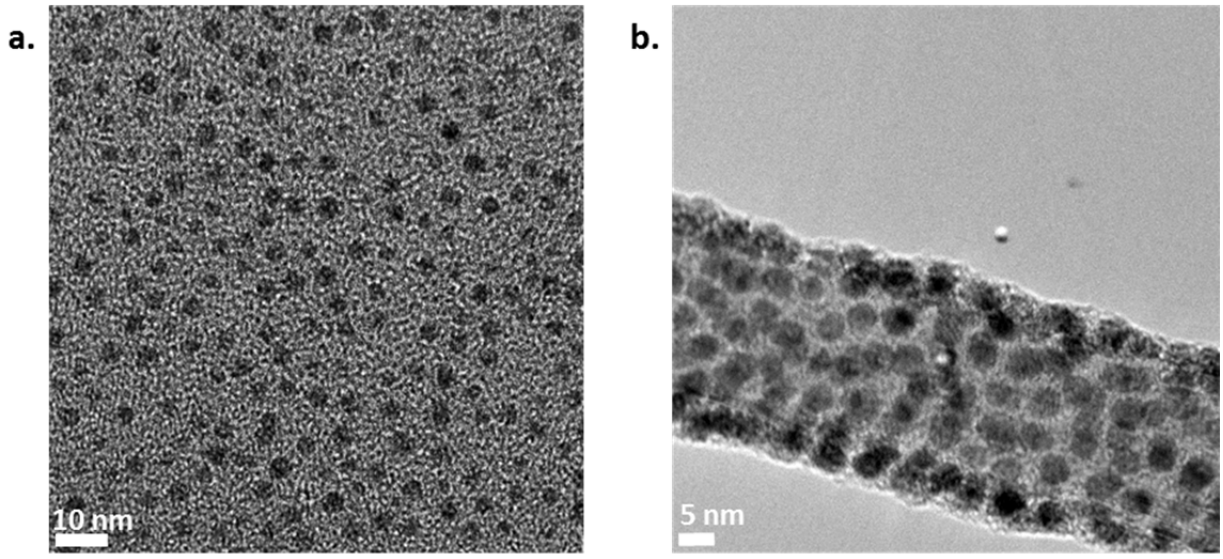

Figure 2-8. TEM micrographs of **a.** DMAP-PdNPs which was deposited onto a carbon support TEM grid. **b.** MWCNT-PdNP hybrid material with PdNPs decorating the MWCNT.

Indeed, covalent attachment of the PdNPs is accomplished as evidence from the TEM micrograph (Figure 2-8b). The density of nanoparticles on the MWCNT is very high and highly uniform upon the MWCNT surface. These particles should be covalently attached considering the chemistry employed and given the centrifugation done to rinse off any unattached nanoparticles.

This approach is promising as a variety of nanoparticles (including semi-conducting nanoparticles) can be attached through this general approach. Furthermore, this approach can be utilized for attaching nanoparticles to BNNTs as well.[73]

2.6 Covalent Modification of BNNTs for the Development of Advanced Aerospace Composites

The type of covalent functionalization of nanotubes presented for MWCNT can also be utilized for the covalent modification of BNNTs. BNNTs have been modified with amine functionalities within the Zettl group[74] which given a chemical handle upon which further moieties can be attached eventually resulting in interesting hybrid materials very similar to the MWCNT-Pd NP hybrids discussed.[75] The amine functionalization was affected through an ammonia plasma treatment which amine functionalized boron atoms on the outer walls of multi-walled BNNTs. However, this technique is geometry limited as the ammonia plasma is most effective on the regions of BNNTs directly exposed to the plasma which is being accelerated towards the charged holder upon which the BNNTs are placed. Furthermore, when powders of BNNTs are used in this manner, any bundles

of BNNTs would not be as effectively functionalized as the plasma will not exfoliate these bundles apart during the process.

A method for the homogeneous functionalization of all exterior BNNT surfaces of a given sample is desired. This has been accomplished previously by the Golberg group through the solution process, hydrogen peroxide treatment of BNNTs.[76] Further attachment of moieties can again allow for interesting hybrid materials or usage of BNNTs for the incorporation into advanced composites. This is especially exciting for the development of advanced aerospace composites. BNNTs possess many ideal properties for aerospace composite enhancement including piezoelectricity,[77, 78] phenomenal temperature stability,[79] excellent radiation shielding, owing the large neutron scattering cross-section of ^{10}B,[80] as well as superior mechanical properties similar to CNTs.[81] All of these properties combined means that high strength, high temperature stability, piezoelectric responsive composites with good radiation shielding could be made, a dream material for researchers of advanced aerospace composites. One current polymer of interest for aerospace composites are the poly-imides, specifically (b-CN)APB/ODPA,[82] which, if properly enhanced with BNNTs, could result in a composite with all the above-mentioned properties.

2.6.1 Attachment of Arbitrary Moieties to BNNTs

To realize advanced aerospace composites using BNNTs, work was done on the functionalization of BNNTs towards the eventual goal of incorporation within polyimide composites. Initially, BNNTs (3 mg) were first dispersed in IPA via sonication and filtered. Hydrogen peroxide (30 % v/v, 20 mL) was used to remove the filter cake and was briefly sonicated in a vial to disperse the BNNT material within the solution. This solution was then added to an acid digestion bomb (Parr, 125 mL capacity), properly sealed and inserted into an oven at 120 °C for less than 12 hrs. Longer reaction times will oxidize the material beyond the point which is desired. The bomb was carefully removed from the oven (carefully as it is very hot, not because it is a "bomb" as they are designed to controllably "explode" if need be and will have already done so if pressure build-up was past its design limitations. This being said, a quick calculation of the pressure build up given H_2O_2 degradation to water and O_2 as well as the pressure built given water above its atmospheric pressure boiling point is recommended if using 1. different volumes of peroxide 2. different concentration of peroxide, or 3. a different size bomb) and allowed to cool to room temperature. Following cooling, the solution was retrieved and filtered using a polycarbonate filter (0.2 μm pore size), and rinsed with DI water (200 mL). This material can then be dispersed readily in water (Figure 2-9).

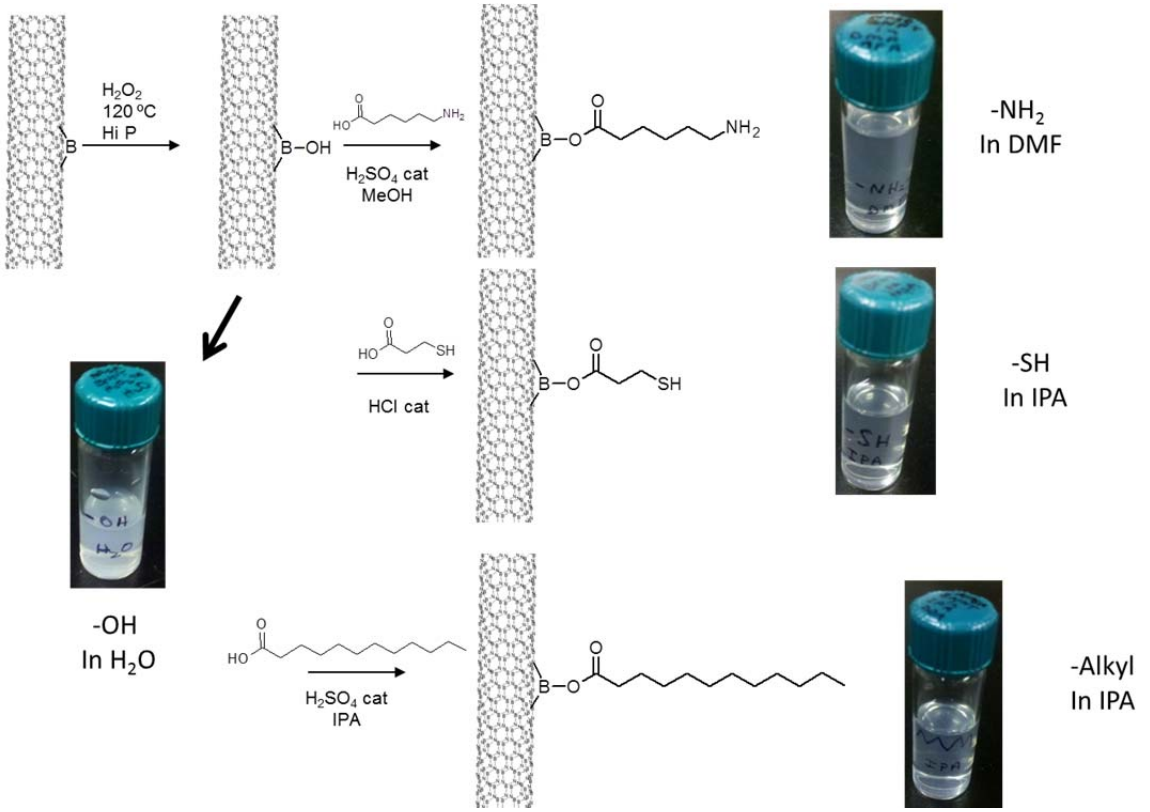

Figure 2-9. Process for functionalizing BNNTs with arbitrary functionalities. Once a chemical handle (-OH) is attached to the outer wall of multi-walled BNNTs, further moieties can be attached such that the exterior of the BNNT has the chemical nature of the desired functionality. The images show the BNNTs functionalized as indicated after brief sonication in the solvents indicated, exhibiting their high solubility in solution which they would otherwise be insoluble in.

After this chemical handle has been attached to the outer wall of the multi-walled BNNTs, attachment of additional moieties can be achieved by reaction with the hydroxyl functionality. For amine functionalized BNNTs (Figure 2-9), an ester is formed through the H_2SO_4 catalyzed reaction of hydroxyl-BNNTs and 6-aminohexanoic acid in methanol. For thiol functionalized BNNTs (Figure 2-9), an ester is formed through the HCl catalyzed reaction of hydroxyl-BNNTs and 3-mercaptopropionic acid in water. For long alkyl-chain functionalized BNNTs (Figure 2-9), an ester is formed through the H_2SO_4 catalyzed reaction of hydroxyl-BNNTs and dodecanoic acid in isopropanol. With all of these functionalization routes, the resulting BNNT material was highly soluble in the appropriate solvent system following functionalization indicating a highly functionalized material.

2.6.2 Attachment of Polyimide Polymer to BNNTs

A specific functionalization route for incorporating BNNTs within a polyimide matrix, specifically a polyimide of great interest for advanced aerospace composites, (b-CN)APB/ODPA,[82] is shown in Figure 2-10. Although this approach for developing advanced BNNT enhanced aerospace composites is exciting, actual composite creation was not practical owing to the scarcity of BNNTs and the relatively large quantities of BNNTs necessary for composite formation. However, this proof of concept for the functionalization of BNNTs and the possibility of incorporating them into aerospace composites is an exciting notion that should be investigated when large quantities of BNNTs become more readily available.

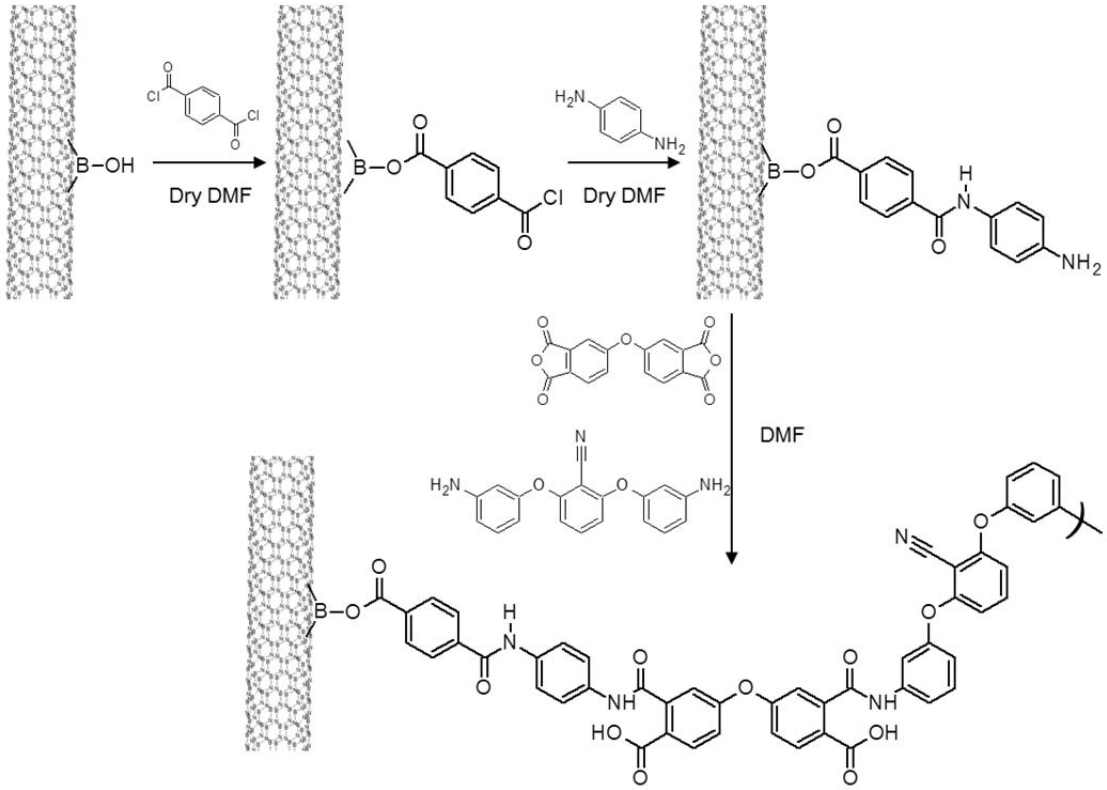

Figure 2-10. Process for the incorporation of BNNTs into the polyimide (b-CN)APB/ODPA.[82]

Chapter 3: Boron Nitride Nanoribbons

Since the discovery of CNTs,[83] the scientific community has witnessed greatly expanded interest in one- and two-dimensional allotropes of carbon, including graphene,[2, 84] and graphene nanoribbons (GNRs)[85-88] (Figure 3-1). Although graphene and GNRs share a common sp^2-bonded carbon framework,[84] the different boundary conditions lead to unique properties. With sp^2-bonded boron nitride, which shares structural analogs with carbon (Figure 3-1), a similar discovery progression can be mapped from BNNTs[89] to few-layer hexagonal boron nitride (h-BN) sheets[90] to a recent mounting interest in boron nitride nanoribbons (BNNRs).[91-100] Significantly different properties also exist between these BN-based materials. For example, BNNRs are theorized to possess a wide range of electronic, optical, and magnetic properties arising from various edge structures and terminations resulting in an extensive body of theoretical work.[91, 93, 94, 96, 98-116] Other exciting properties have been theorized when hybrid nanoribbons structures combining boron nitride and carbonaceous phases are considered.[106, 107, 117-126] These properties are of great fundamental interest and they also have implications for applications within various fields including low dimensional electronics, spintronics and optoelectronics.[91, 93, 94, 96, 98-116]

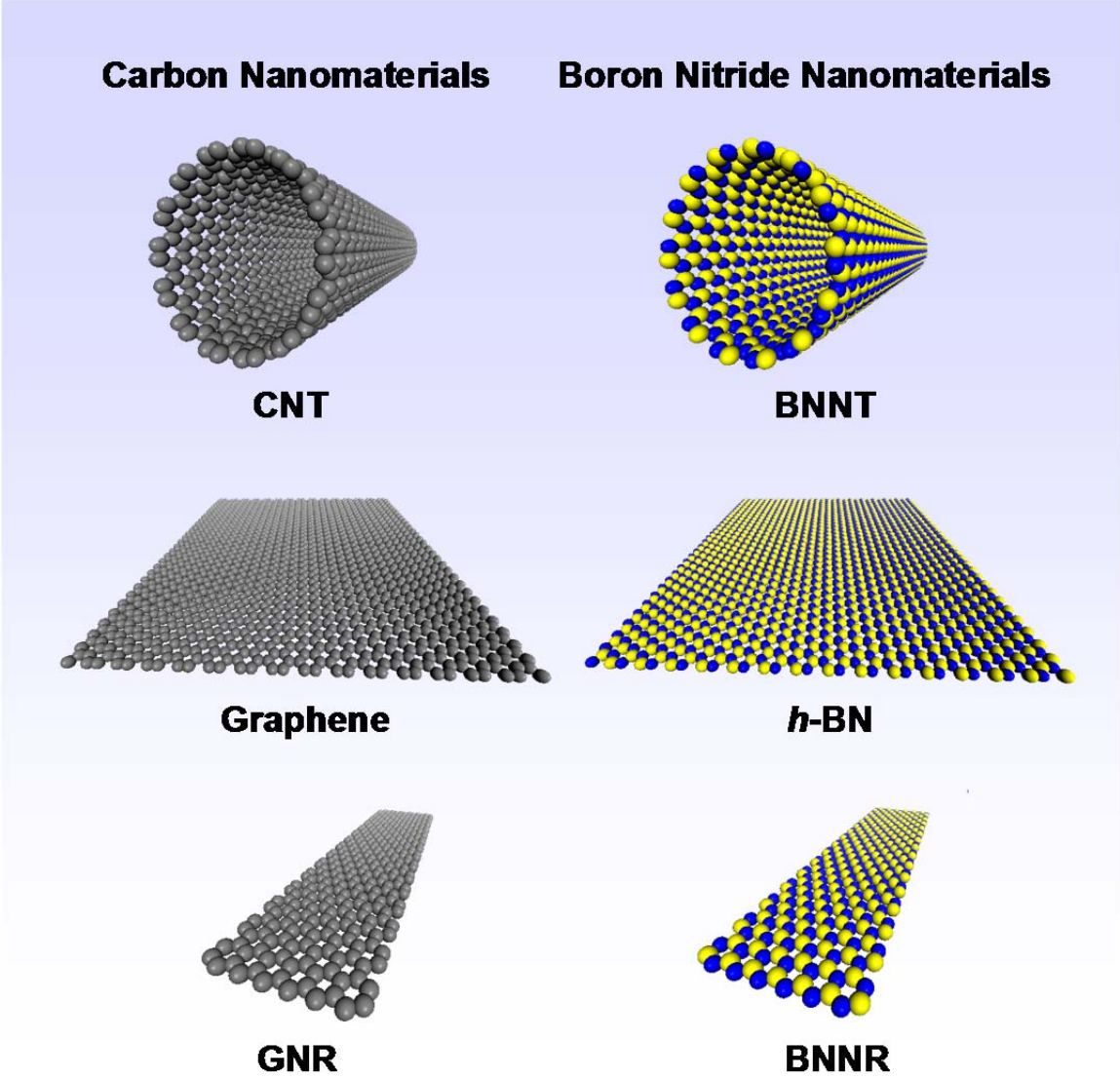

Figure 3-1. (Left) One and two dimensional carbon nanomaterials including a CNT, graphene, and a GNR. Carbon atoms are displayed in grey. (Right) One and two dimensional boron nitride structural analogues including a BNNT, single sheet *h*-BN, and a BNNR. Boron atoms are displayed in blue and nitrogen atoms are displayed in yellow. Though local bonding configurations are nearly identical for the materials in each column, boundary conditions of the selected overall geometries result in unique distinct edge states and unique characteristics. For nanotubes, the circumference defines a boundary condition, whereas for a large nanosheet, the circumferential boundary conditions are lifted and edge states have minimal affect. For nanoribbons, the width defines new boundary conditions and edge states can significantly affect many material properties. Images made using Accelrys Materials Studio 4.3.

3.1 First Synthesis of BNNRs

Numerous routes to GNRs are now well established,[85-88] and some of these approaches, such as the plasma etching of nanotubes imbedded within a polymer,[127] have been explored for the syntheses of BNNRs.[99] However, unlike the case for GNRs,[85-88] the facile, scalable synthesis of high quality BNNRs remains a significant challenge and only one alternative synthesis of BNNRs[99] has attempted to answer the call of the significant body of theoretical BNNR research. The approach for this synthesis was to spin BNNTs onto a substrate, embed them within a polymer, peel them off the substrate and then plasma etch the bottom side of the peeled polymer. The effect was to plasma-etch portions of the BNNTs embedded within the polymer, yielding BNNRs following removal of the surrounding polymer, very similar to one of the first GNR synthetic methods.[86] Although this was indeed the first synthetic method for BNNR production, many aspects of this synthesis were not ideal. The synthesis requiring a substrate will always be limited in terms of its scalability. Also, the polymer required for synthesis makes separation and cleaning of the ribbons difficult. Indeed, conductivity measurement of these ribbons done in situ during TEM analysis likely had conductivity resulting from all the residual carbon owing to the required polymer step of the synthesis.[119] Finally, few layer ribbons with quality edges were difficult to produce via this method as plasma etching is not preferable in any certain geometry for a given precursor BNNT and apparently etches through many walls of the precursor BNNT.

3.2 First Scalable Method for High Quality BNNRs

Given these limitation of the BNNRs produced via the plasma etch method, other approaches to BNNR formation were considered, especially taking into consideration the various approaches for GNR synthesis available. A particularly effective route to high quality GNRs involves potassium-intercalation-induced longitudinal splitting of CNTs.[88] This is the approach taken here for the synthesis of BNNRs.

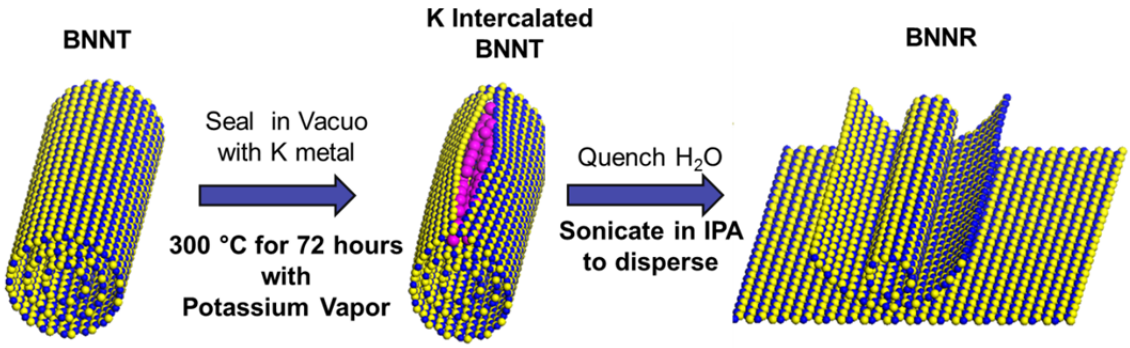

Figure 3-2. Schematic of the splitting process of a BNNT to form a BNNR. Boron atoms are in blue, nitrogen atoms in yellow, and potassium atoms in pink. The pristine BNNT (Left) begins to locally unzip owing to potassium intercalation induced pressure buildup and reactivity with features of the BNNT (Middle) which results in further splitting of the nanotube in the longitudinal direction to form few layer nanoribbons (Right) which are quenched with water and can be readily dispersed in isopropanol. Images made using Accelrys Materials Studio 4.3.

Figure 3-2 shows pictorially the mechanism for splitting BNNTs through alkali metal intercalation. Using this approach, we find that potassium vapor treatment of BNNTs yields narrow (between 20-50 nm), long (at least 1 μm in length), few sheet (usually between 2-10 layer) pristine BNNRs with very uniform widths as well as minimal defects within the ribbon plane and along their edges. The synthesis process is bulk, facile, and easily scalable. Approximately 1% of treated BNNTs exhibit splitting, comparable to a common bulk route to GNRs,[127] and separation should be possible through established GNR purification techniques.[88, 127] Our process allows for BNNRs that can be stabilized in a solvent and then dispersed onto various substrates to allow for further characterization and potential device fabrication.[128]

3.2.1 Precursor BNNTs

BNNTs from different synthetic methods afforded themselves differently to potassium vapor treatment. Some BNNTs are noticed to have closed ends (Figure 3-3b), and splitting was more difficult with these tubes presumably as a closed end would hinder potassium intercalation between tube walls. If these tubes were subjected to aggressive sonication, ends could be opened by effectively ripping apart tubes to form smaller tubes, but significant damage to nanotube walls was also caused by this process, and splitting of this material was likewise difficult. BNNTs synthesized through the vertical induction furnace method using metal oxides (specifically Mg and Sn) as catalysts with solid boron and ammonia as B and N sources, respectively, were ideal for usage as very high crystallinity, predominantly open ended BNNTs are formed (both Figure 3-3a, Golberg lab material, and Figure 3-3d, Zettl lab material). Another material which potassium vapor treatment has been attempted on is BNNT material synthesized by collaborators in a NASA lab (Figure 3-3c).[129] This novel synthetic technique utilizes a high power laser in a high pressure N_2 environment to react pure boron powder with elemental nitrogen. This method produces very small diameter BNNT of long lengths, but the increased interaction between these small diameters of BNNTs (similar to bundling of SWCNTs) make analysis of the ends of these BNNTs very difficult.

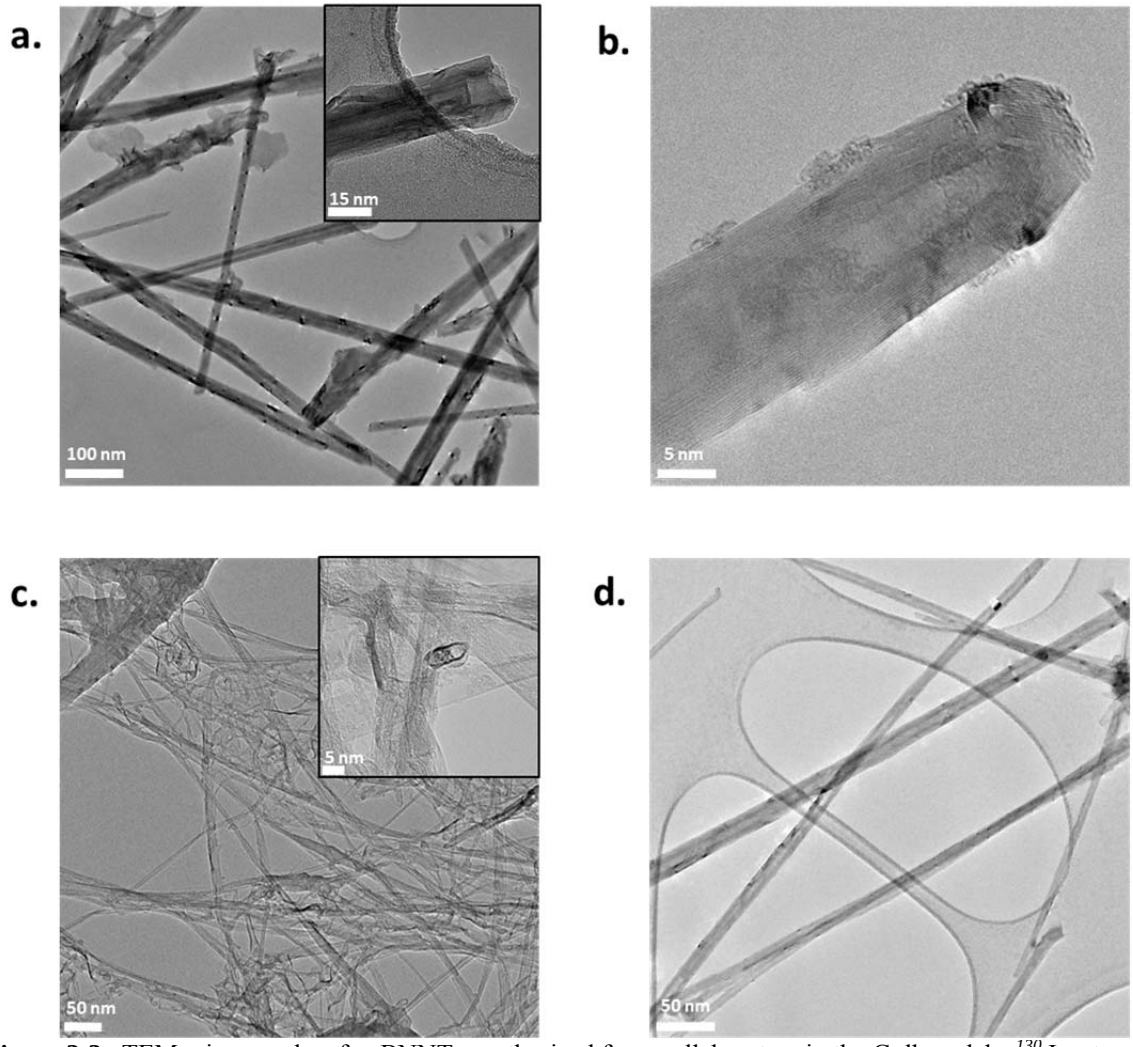

Figure 3-3. TEM micrographs of **a.** BNNTs synthesized from collaborators in the Golberg labs.[130] Inset shows an opened end commonly found for these BNNTs. **b.** BNNTs synthesized (by Mark Lorente, Zettl labs) through a CVD furnace method using NH_3, boron powder, and MgO, very similar to a method developed in the Golberg labs.[131] **c.** BNNTs synthesized by collaborators from NASA research via a laser system under high pressure N_2 with boron powder.[129] Inset shows how determination of whether the ends of these tubes are open is difficult given the highly interacting nature of these small diameter BNNTs. **d.** BNNTs synthesized (by Michael Rousseas, Zettl labs) through a high temperature induction furnace method using NH_3, boron powder, and SnO.

The precursor BNNTs (Figure 3-3d) utilized for this study were synthesized through a process similar to a previously reported route.[130] A mixture of solid boron, magnesium oxide and tin oxide powders were placed in a graphite crucible which was heated under a nitrogen atmosphere in a vertical induction furnace to 1500 °C. Nitrogen carrier gas brought the powder into a graphite vessel where it reacted with ammonia to form a white, spongy material rich in BNNTs.

3.2.2 BNNR Synthetic Route

BNNT materials (3 mg, Figure 3-3d) were taken as synthesized, and placed into the bottom of a ¼ inch quartz tube sealed on one end. A notch in the tube was made to separate the BNNTs from the potassium metal (30 mg), which was freshly cut in a fume hood, rinsed with dry diethyl ether to clean off mineral oil, and then placed into the quartz tube (CAUTION: Potassium and sealing of the potassium-loaded ampoule should be handled with utmost care, due to the highly reactive nature of potassium metal. Users should wear safety glasses and a face shield, and all operations should be done in a fume hood when handling this reagent). The quartz tube was then taken to 10^{-6} Torr by evacuating with a turbo pump and the quartz tube was sealed with a H_2/O_2 torch. The created ampoule was then placed in an oven at 300 °C for 72 hours. Higher temperatures resulted in significant reduction of the quartz and sometimes resulted in broken ampoules. Lower temperatures resulted in lower yields of BNNRs. Residual carbonaceous materials, presumably from remaining mineral oil and from atmospheric adsorbates, graphitized on the surface of the BN material during the treatment making it grayish. This residual carbon was therefore calcined off at 600 °C in air for 30 minutes such that only BN material remained. Both the BNNT and BNNR material could be readily dispersed in isopropanol under mild sonication and then dried onto any surface. For our purposes, the material was dispersed in IPA and spotted onto Au mesh lacey carbon TEM grids and allowed to dry for further analysis. TEM analysis was done on a JEOL 2010 microscope operated at 100 kV.

3.2.3 BNNR TEM Analysis and Discussion

BNNTs used for the BNNR synthesis were of variable diameters ranging from 6 nm to 70 nm (see Figure 4-4a). Figure 3-4a displays a TEM micrograph of a typical BNNT precursor. The tube displays characteristic higher contrast walls with a lower contrast inner core.[132] The periodic darkened regions along the length of the nanotube are common for high quality BNNTs.[133] Diffraction of the BNNT (Figure 3-4a inset) displays spots that are elongated perpendicularly to the tube axis, owing to the curvature of the nanotube, and demonstrates high intra-wall crystallinity.[133]

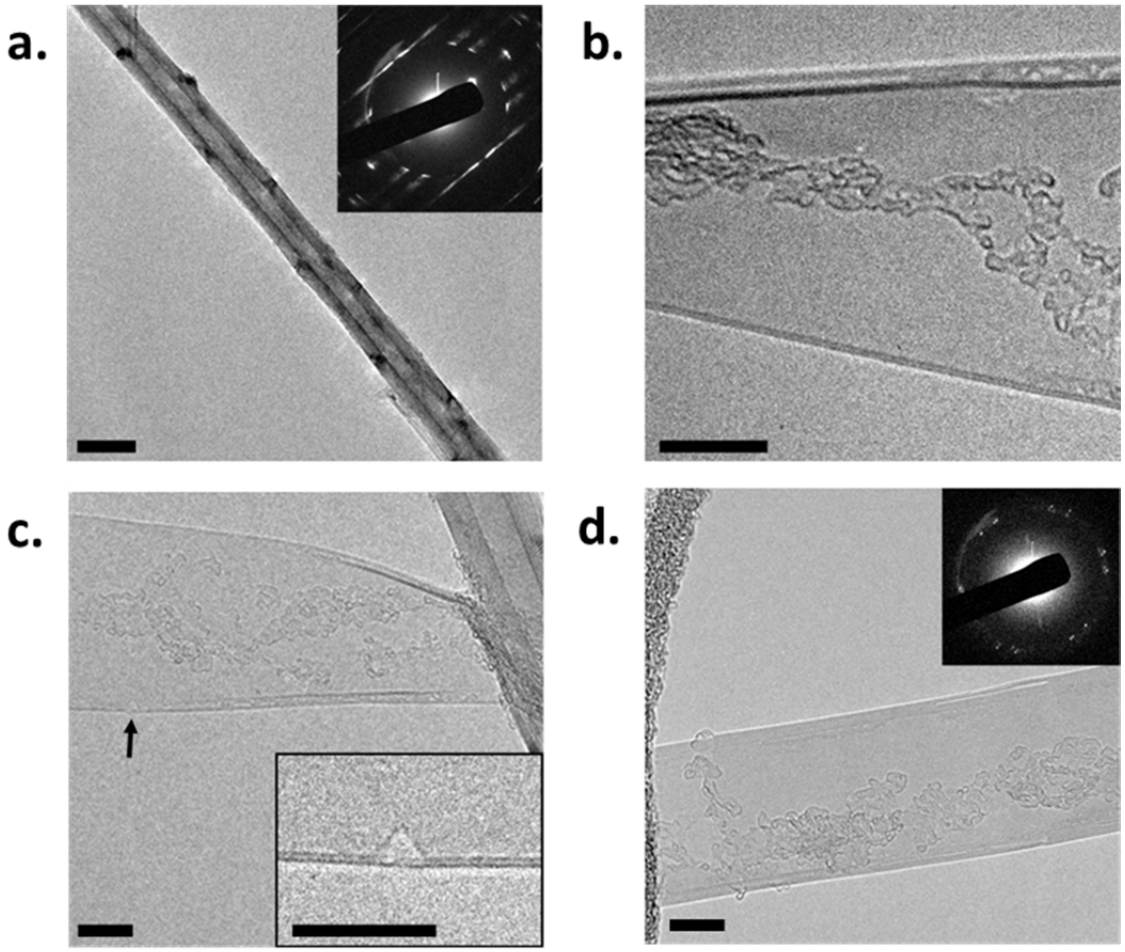

Figure 3-4. TEM micrographs of the following: **a.** Common BNNT precursor. Scale bar is 50 nm. Inset is diffraction of the BNNT. Diffraction peaks elongate perpendicularly to the tube axis, indicating a cylindrical geometry. **b.** A few layer BNNR that has a pristine, straight edge along the bottom and is scrolled at the top. Carbonaceous adsorbates are noticeable on the ribbon surface. Scale bar is 10 nm. **c.** Another few layer BNNR that has unzipped off its parent tube on the right. Arrow marks the zoomed in region found in the inset, which highlights a singular triangular defect found along the ribbon edge. Scale bars are 10 nm. **d.** A lone BNNR about 5 layers thick. Scale bar is 10 nm. Inset shows diffraction of BNNR which lacks elongation of diffraction peaks indicating a flat geometry.

Figure 3-4b displays a TEM micrograph of a BNNR likely two layers thick with a pristine, linear edge and nearly defect free surface. This ribbon scrolls up along the top and some carbonaceous adsorbates are noticeable on the ribbon surface. Figure 3-4c displays a TEM micrograph of a BNNR 40 nm in width which has been partially split off of its parent tube. This ribbon also appears to be two layers thick and scrolls up when near the parent tube, straightening out further from the tube. This ribbon also has minimal defects within the plane and along its edge, but the inset of Figure 3-4c highlights a singular defect found along the edge. Triangular defects like this are commonly observed when boron nitride materials are subjected to electron beam irradiation and normally a defect of this geometry is zigzag along its edge.[134] Assuming this orientation, the general ribbon edge here would be zigzag. This is likely since BNNTs often form with all their walls being mostly of armchair or mostly of zigzag

orientation,[132] yielding ribbons with edges defined by the tube chirality. The periodic contrast seen along the observed edge in the micrographs of Figure 3-4 should not be mistaken for the ribbon edge where bond termination occurs. It instead represents a fold where the edge of the ribbon folds back onto the plane of the ribbon.[135] Such edge folding or partial scrolling is common in graphitic materials,[135, 136] including GNRs,[88] and it is also observed for boron nitride materials.[99] However, the linear nature of the observed edge likely indicates a similarly straight edge where bond termination does occur.

Brief sonication in isopropanol separates many ribbons from their parent tubes, and a lone ribbon of about 5 layers is seen in Figure 3-4d. Diffraction of the BNNR (Figure 3-4d inset) is markedly different from the diffraction of a BNNT. Specifically, the curvature induced elongation of diffraction spots, seen for nanotubes, is absent for the ribbon, indicating its flat geometry. This diffraction pattern further indicates that the highly crystalline nature of the parent BNNTs is conserved during BNNR formation. It also reveals the edge orientation to be approximately armchair in this ribbon. Although BNNRs, similar to the parent BNNTs,[132] are expected to often have successive layers of a similar orientation, our diffraction studies also show a second set of spots resulting from either another preferred orientation of some layers or folding of the ribbon along the edge.

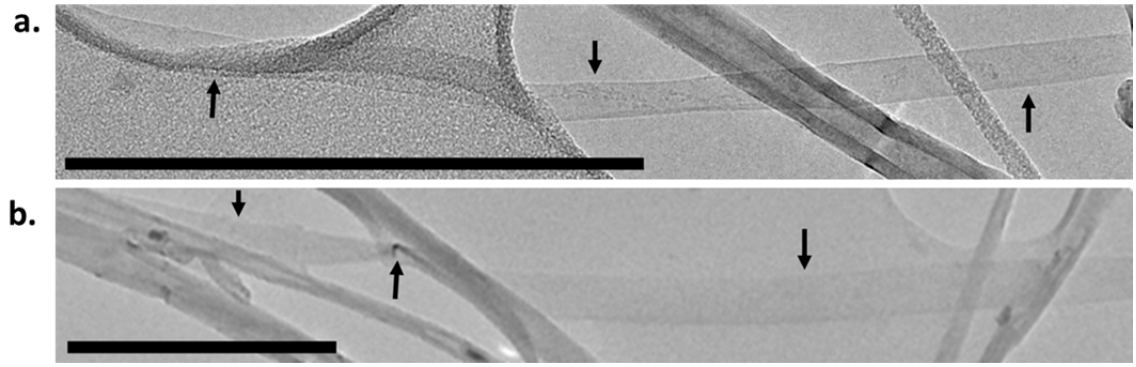

Figure 3-5. TEM micrographs of: **a.** A long BNNR, having a consistent width along the length of the ribbon and straight edges. It spans across the image draping on top of lacey carbon to the left and over an unzipped BNNT to the right. Three arrows point to the ribbon to aid identification. **b.** A BNNR over 1 micron in length, pointed to by the arrows. The middle arrow points to a twist in the BNNR. Scale bars are both 300 nm.

Figure 3-5 shows more BNNRs that are well-separated from their parent tubes, one being at least 1 μm in length. Ribbons tend to drape along the lacey carbon and BNNTs making the full length of the ribbons difficult to determine. The flexibility of the BNNRs is evident as a ribbon changes slightly in direction while draping along the lacey carbon support in Figure 3-5a. Figure 3-5b shows another ribbon with a full twist (labeled by the middle arrow). Such geometries are not possible for rigid BNNTs. Ribbons are seen to have consistent widths along their entire lengths, only changing in apparent width when accommodating geometries like the twist seen in Figure 3-5b.

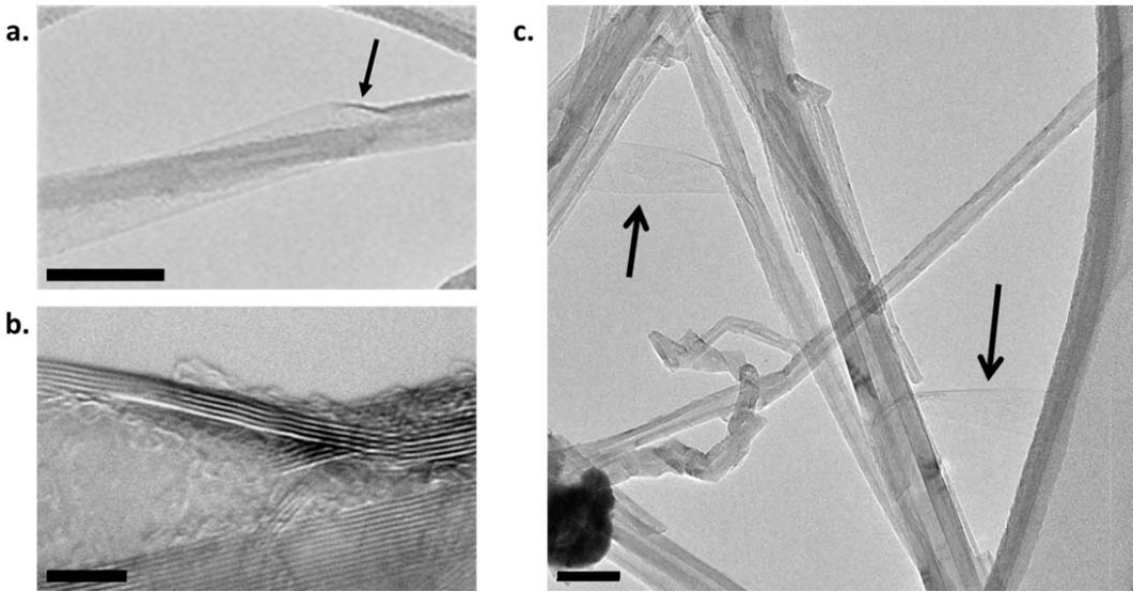

Figure 3-6. TEM micrographs of: **a.** A few layer BNNR splitting off its parent ribbon. The arrow marks the zoomed in region found in (b). Scale bar is 50 nm. **b.** Zoomed in region where the few layer nanoribbon is seen coming off its parent nanotube. Scale bar is 5 nm. **c.** Two BNNTs next to each other exhibiting splitting with their associated BNNRs coming off the sides as indicated by the arrows. Scale bar is 50 nm.

Figure 3-5a,b displays details of a ribbon in the process of splitting off its parent tube, clearly displaying how a few outer walls peel off of the nanotube to form the nanoribbon, which then separates away from the parent tube. Again, straight edges and a consistent width are observed for this ribbon. Although the intermediate stage of splitting is highlighted here, most BNNRs are seen to be fully separated from their parent BNNT following the gentle sonication used to disperse them in solution. Figure 3-5c shows neighboring BNNTs with BNNRs actively splitting off of them.

3.2.4 Alternative BNNT precursors

Other BNNT sources were investigated to determine their response to potassium vapor treatment (Figure 3-7). BNNTs synthesized through the laser heating of elemental boron powder in high pressure N_2[129] do exhibit splitting into BNNRs (Figure 3-7b). However, the very "sticky" nature of the BNNTs, which exhibit strong intermolecular interactions with each other and are difficult to observe individually, makes assessment of the success of potassium vapor treatment difficult.

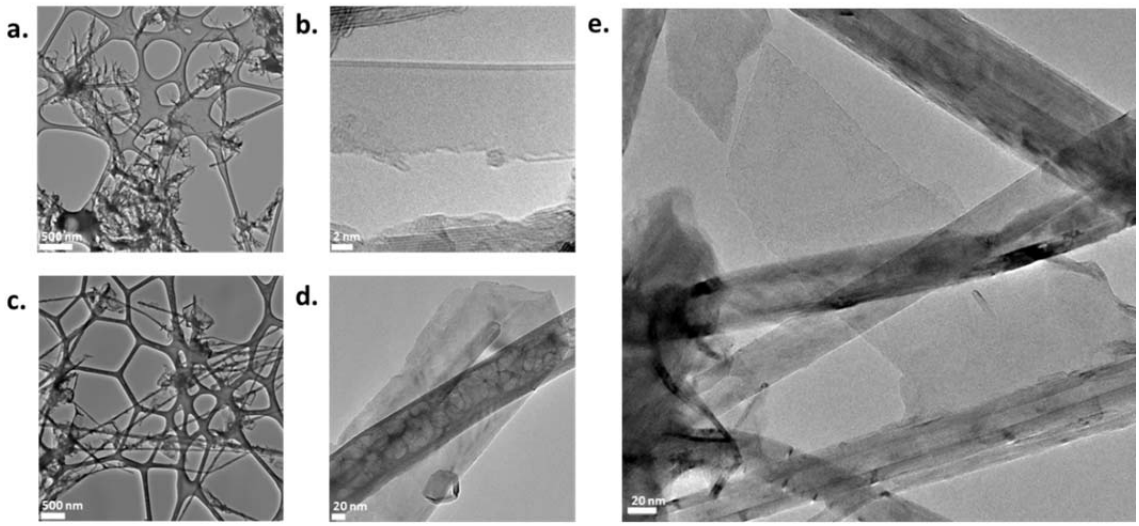

Figure 3-7. TEM micrographs of **a.** BNNRs from the NASA BNNTs (Figure 3-3c) and **b.** zoom in of a BNNR from the NASA BNNTs **c.** BNNRs from the Golberg BNNTs (Figure 3-3a), **d.** zoom in of a BNNR from the Golberg BNNTs and **e.** a BN platelet formed from Golberg BNNTs.

BNNTs synthesized by the Golberg labs (Figure 3-3a)[130] also exhibited splitting to form BNNRs (Figure 3-7c,d). These larger diameter BNNTs do not agglomerate, so assessment of precursor BNNT ends is possible and confirms that most BNNT ends are open and likely suitable for potassium vapor treatment. Indeed, BNNRs do form (Figure 3-7c,d), however, given the understood mechanism of both potassium intercalation induced pressure build-up and the reactivity of potassium with sp^3 bonded lines of boron atoms found at the junction of facets within a BNNT (see later section), these BNNTs do not seem as effective at BNNR formation. The reason for this is that Golberg BNNTs have a highly faceted structure along the length of the BNNT. Some BNNTs display a continuous periodic structure like that found for BNNTs synthesized within the Zettl labs (Figure 3-4a), but more often small facets will form randomly along the length of the BNNT. Given this, these facets become "liberated" under potassium vapor treatment, often forming BN platelets (Figure 3-7e) which are much more commonly observed features of potassium vapor treated Golberg BNNTs than actual BNNRs. Although these BN platelets may be of interest given the quality edges they usual exhibit, they are not strictly BNNRs and are more dissimilar to the theoretical studies done thus far on BNNRs.

3.2.5 Alternative BNNR Synthetic Routes

Alternative methods for the synthesis of BNNRs were undertaken in close collaboration with the Rice group headed by James Tour. A method developed by Bostjan Genorio involves dissolving a sodium-potassium alloy in 1,2-dimethoxyethane, in which precursor BNNTs are dispersed. Allowing this reaction to occur over 5 days followed by quenching with methanol results in quality BNNRs (Figure 3-8). This method is promising as it is both more easily scaled (given the solution chemistry employed) as well as seems to provide for better yields of BNNRs.

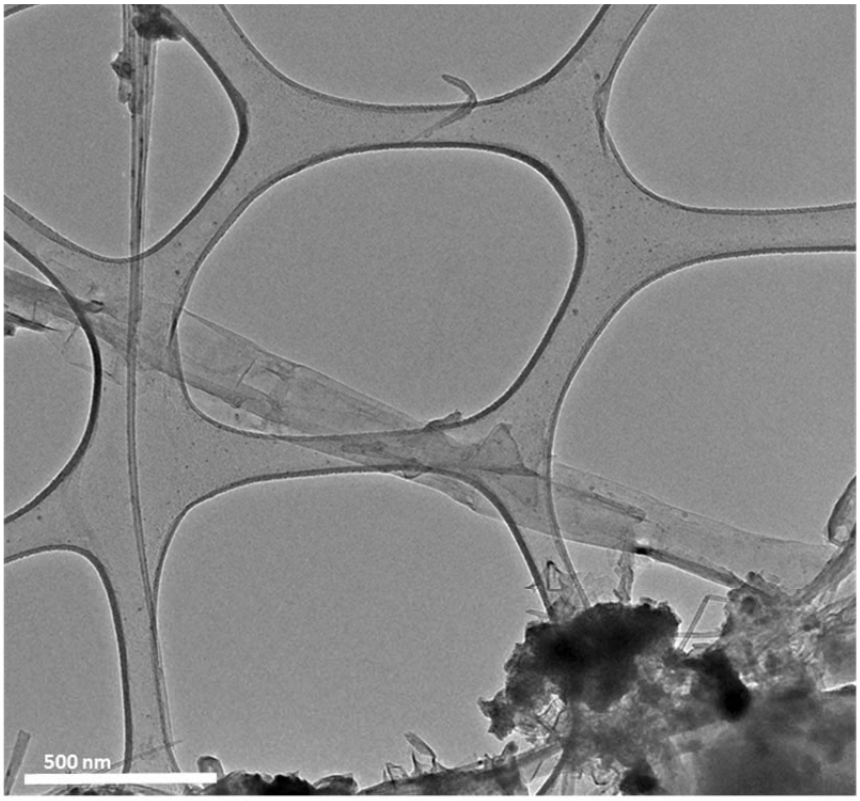

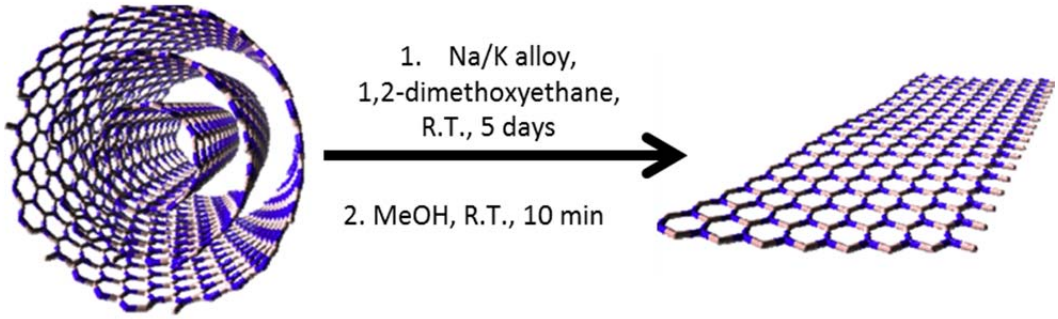

Figure 3-8 TEM micrograph of a BNNR formed through the alkali solubilized method for BNNT splitting, being pictorially represented in the lower schematic, where precursor BNNTs (left) are reacted with a Na/K alloy dissolved in dry 1,2-dimethoxyethane to form BNNRs (right) following a quench step in methanol.

3.2.6 Separations of BNNRs from Parent BNNTs

If separation of the synthesized BNNRs from the parent BNNTs can be achieved, increases to yields (which have been minimal for the alternative techniques attempted) will be unnecessary as any reasonable fraction of BNNRs which are formed from BNNTs can be separated to yield a material which has a very high proportion of BNNRs.

3.2.6.1 Separation via PmPV Wrapping

One of the most common and useful syntheses for GNRs utilizes the polymer poly(m-phenylenevinylene-co-2,5-dioctoxy-p-phenylenevinylene) (PmPV), whereby a material having relatively few GNRs compared to precursor MWCNTs can be solubilized through the aid of a wrapping polymer and then ultracentrifuged.[137] Owing to the density difference between a polymer wrapped GNR and a polymer wrapped MWCNT, ultracentrifugation is able to sediment the MWCNTs much quicker than the GNRs. This results in a solution of almost pure GNRs which can be utilized for a variety of procedures following removal of the polymer (Figure 3-9).

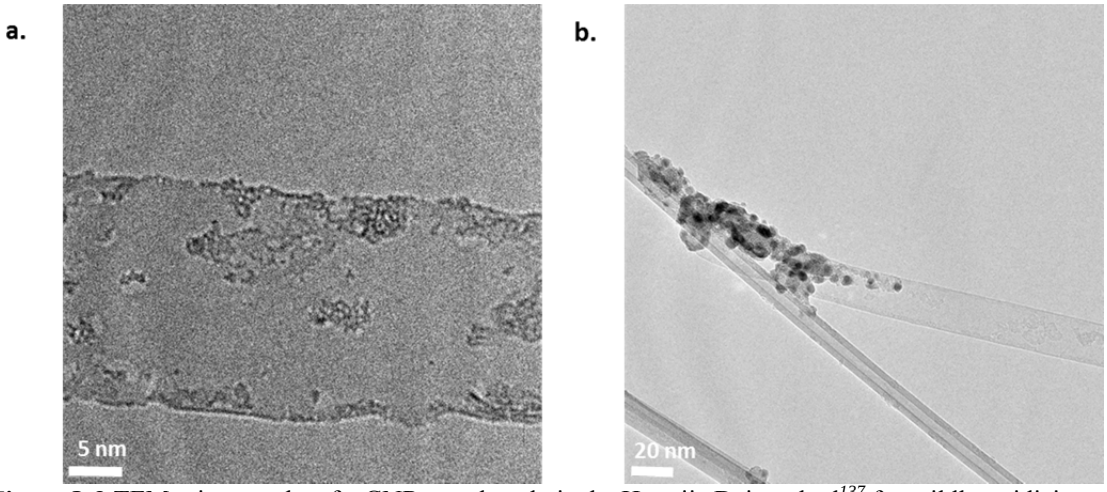

Figure 3-9 TEM micrographs of a GNRs produced via the Hongjie Dai method[137] for mildly oxidizing MWCNTs, surfactant wrapping and unzipping through sonication and finally ultracentrifugation for separation of GNRs from precursor MWCNTs. **a.** A single layer GNR with residual polymeric wrapping molecule. Holes are noticed as the sample is heated in air to 425 °C for 15 min. resulting in degradation of the GNR. **b.** A GNR (upper right) protruding off a parent MWCNT (bottom left) with residual polymer at the junction of these.

Undergoing a similar procedure, BNNR separation from the parent BNNTs was attempted. Solutions of PmPV (7.5 mg) in 1,2-dichloroethane (DCE, 10 mL) were made in which potassium treated BNNTs (3 mg) were dispersed via mild bath sonication (Crest Sonicator, Model CP230D, power level 3, 60 minutes). Immediately following sonication, solutions were super-centrifuged at 19,000 RPM in a Sorvall Supercentrifuge for 4 hours. The supernatant was carefully removed and filtered using an anodized alumina filter (0.2 μm pore size) and rinsed with DCE (200 mL). The filtered material was dispersed in IPA via mild sonication and spotted onto a lacey carbon TEM grid. For copper or gold mesh lacey carbon TEM grids, heating was done in air at 425 °C for 15 minutes to remove residual polymer to allow for better imaging, resulting in solution with the ratio of BNNRs to BNNTs being slightly enhanced from the original material (Figure 3-9), although purification was not as successful as hoped (still only ~5% BNNRs). This approach varies slightly from the one employed for GNR separation for a few distinct reasons. BNNTs and BNNRs agglomerate quickly in solution, and if a solution of sonicated potassium treated BNNTs is allowed to rest for more than a few hours,

agglomeration begins making preferential sedimentation of BNNTs compared to BNNRs impossible. This being said, immediate centrifugation following sonication is necessary. Furthermore, the sedimentation force required for pelletizing BNNT material solubilized by PmPV in DCE is less than that necessary for pelletizing CNT material. Given this, centrifugation speeds can be slower, however centrifugation at ultracentrifuge speeds would still be ideal, but not yet studied. A final note that although the yield seems similar, separations of Golberg synthesized BNNTs following potassium treatment versus Zettl lab induction furnace synthesized BNNTs following potassium treatment were very different. The ones synthesized in the Zettl labs were much more successfully separated, yet the overall availability of the Zettl BNNT material was very low compared to the Golberg synthesized BNNT material, making proper separation studies difficult.

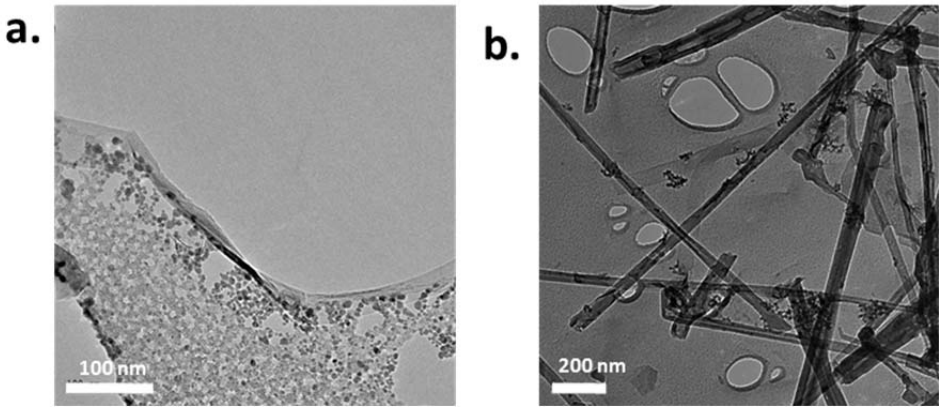

Figure 3-10. TEM micrographs of BNNRs separated from Golberg method BNNTs **a,b.** via PmPV wrapping and centrifugation. Many parent BNNTs still remain (b).

3.2.6.2 Separation via Superacid Solubilization

A method utilized for separating BNNRs from the parent BNNTs was through the superacid solubilization and subsequent centrifugation of the potassium treated BNNT material. Super acid solubilization of graphitic and boron nitride based nanomaterials has proven largely successful,[138] with the solubilization of hBN nanosheets being specifically investigated in methanesulfonic acid (MSA).[79] This MSA solubilization was investigated for the solubilization of potassium treated BNNTs such that subsequent centrifugation could result in separation of the BNNRs from the parent BNNTs. Potassium treated BNNTs (3 mg) were initially dispersed within IPA and sonicated until no large chunks remained. This materials was filtered using a polycarbonate filter, and the filtered material was transferred into a glass centrifuge tube ("oil centrifuge tube") and allowed to air dry. To this tube, MSA (20 mL) was carefully added. This tube was capped and parafilmed before sonicating at lower power (power level 3, 90 minutes) at which point a noticeable color change occurs indicating solubilization of the boron nitride nanomaterials.[79] The centrifuged tube was then properly balanced and centrifuged at moderate speed (7,000 RPM) for 4 hours. Unfortunately due to the reactive nature of this superacid, higher speed centrifugation is difficult to safely experimentally undertake. The supernatant is carefully and slowly decanted into a large reservoir of water (300 mL,

which is contained in a much larger beaker (1 L) such that any splashing from superacid addition to water is not hazardous), which is then filtered through a Teflon filter (0.2 μm pore size). The filter cake is redispersed in water (300 mL) and refiltered as above. This material is dispersed in IPA and spotted onto TEM grids for analysis. Separations through this route did seem possible (Figure 3-11), but the lower centrifuge speeds required makes proper separation more difficult.

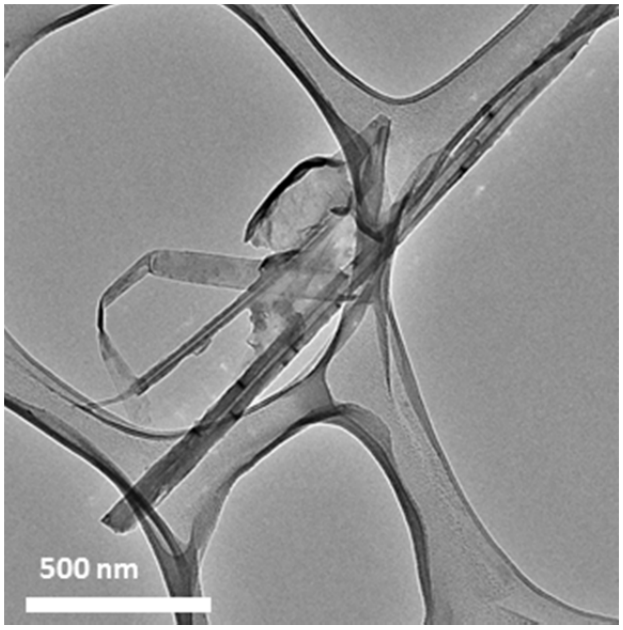

Figure 3-11 TEM micrographs of BNNRs separated from Golberg method BNNTs via methanesulfonic acid solubilization and subsequent centrifugation showing a BNNR and a few remaining parent BNNTs.

Separation using solutions with chlorosulfonic acid (CSA) were also undertaken. However, CSA is a much stronger superacid, so the experimental design must be changed to account for this and resulted in poorer separations. Briefly, if CSA is used in the manner described above for MSA, much more care must be taken at each and every step. CSA must be stored and handled in the glove box given its violent reactivity with water. Atmospheric moisture will only degrade the quality of CSA, but any contact with liquid water will result in violent spitting and spraying of a super acid (not desirable!!!!). Given this, preparations of solutions must be done in a glove box. Then sonication must be closely monitored as the tube falling into the sonicator would be disastrous (however retrieving the tube if it were to fall into the sonicator is NOT recommended unless you are absolutely certain that there should be no leaks in the tube cap seal, therefore, much parafilm should be used to help make that seal tight!!). Centrifugation can then be done with a glass centrifuge tube (CSA will react even more quickly with any polymeric centrifuge tube). Decanting must be carefully undertaken in many respects. A large beaker of low density ice (not cubes, but the ice chunks common for ice makers is suitable) must be prepared. Then a glass pipette can be used to carefully withdraw a mL at a time of the CSA/BNNT/BNNR material. The pipette must then be quickly inserted to the BOTTOM of the ice (with a good 5 inches of ice above the tip where CSA will be released) and then moderately quickly the CSA solution should be dispensed. Care must

be taken to not get any solution onto the pipette tip (from melted ice or from touching the rising liquid solution) as any droplets on the pipette tip will result in spitting of the CSA solution when subsequent aliquots of the supernatant are withdrawn. Finally, any and all materials that have come into contact with CSA will violently spit when exposed to water, so be very careful with the discarding of pipette tips, centrifuge tubes or any other material that come into contact with CSA. Also, these materials must be deluged with water to bring washing solutions of them to a moderately safe pH. The ice solutions can then be allowed to melt and then filtered as above. However, given all the precautions of this approach coupled with the initial lack of results means that this approach for separating BNNRs from BNNTs is likely not worth further investigation.

3.2.6.3 Separation via Oxidation of BNNT/BNNRs

An approach to separate BNNRs from the parent BNNTs undertaken was through the oxidative functionalization of potassium treated BNNT material followed by solubilization and subsequent centrifugation. The method employed was based off an approach developed by the Golberg labs.[76] Potassium treated BNNT materials (3 mg) is first dispersed in IPA via sonication and filtered. A process identical to that described in Chapter 2 for the oxidation of pristine BNNTs was then done. After reaction with H_2O_2 at elevated temperature, the solution is retrieved and filtered using a polycarbonate filter (0.2 μm pore size). The filter cake is then sonicated in IPA or NMP (90 minutes, power level 3) and then supercentrifuged as above for the PmPV samples. The supernatant is retrieved and then spotted onto lacey carbon TEM grids. Separations using this approach were not as promising as hoped and the material would have to be restored back to its un-oxidized state which may prove difficult (see Chapter 1).

A final approach for separation which was conceived and initially investigated was size selective filtration of materials. Following sonication, dispersed solutions of BNNTs and BNNRs could be placed in a dialysis membrane will a very large pore size. The flexibility and smaller overall size of BNNRs could allow for them to preferably travel through the dialysis membrane pores. Although this was initially investigated, experimental procedures were not optimized and work would have to be done to optimize this process.

3.2.7 Understanding the Mechanism of Splitting and the Resultant BNNRs

Potassium intercalation between walls of a nanotube is crucial for the splitting process with the previously reported GNRs synthesis[88] and is considered essential in our case of BNNR formation. However, unlike the case of graphitic materials where there exists a large body of research on intercalation compounds,[139] studies on the intercalation of h-BN are limited.[140, 141] Alkali metals are among the few experimentally reported intercalants of h-BN,[140, 142] and the equilibrium interplanar spacing for potassium intercalated h-BN has been calculated to be 5.8 Å.[143] For a nanotube, this significant increase in wall spacing from 3.4 Å[132] would result in significant bond strain circumferentially around the tube. The mechanism of splitting proposed to occur during

potassium intercalation of CNTs likely also occurs for BNNTs, whereupon intercalated potassium islands grow from an initial starting point of intercalation.[88] This island growth continues until enough circumferential strain results in bond breakage. Finally, potassium bonds to the bare ribbon edge and the hindrance arising from these moieties induces further splitting longitudinally.[88] If the potassium intercalation induced splitting of BNNTs occurred randomly within the tube, the edges of the resultant ribbons would be expected to be only moderately straight. The extremely linear, high quality edges observed for our BNNRs indicate that some further order to the splitting process occurs.

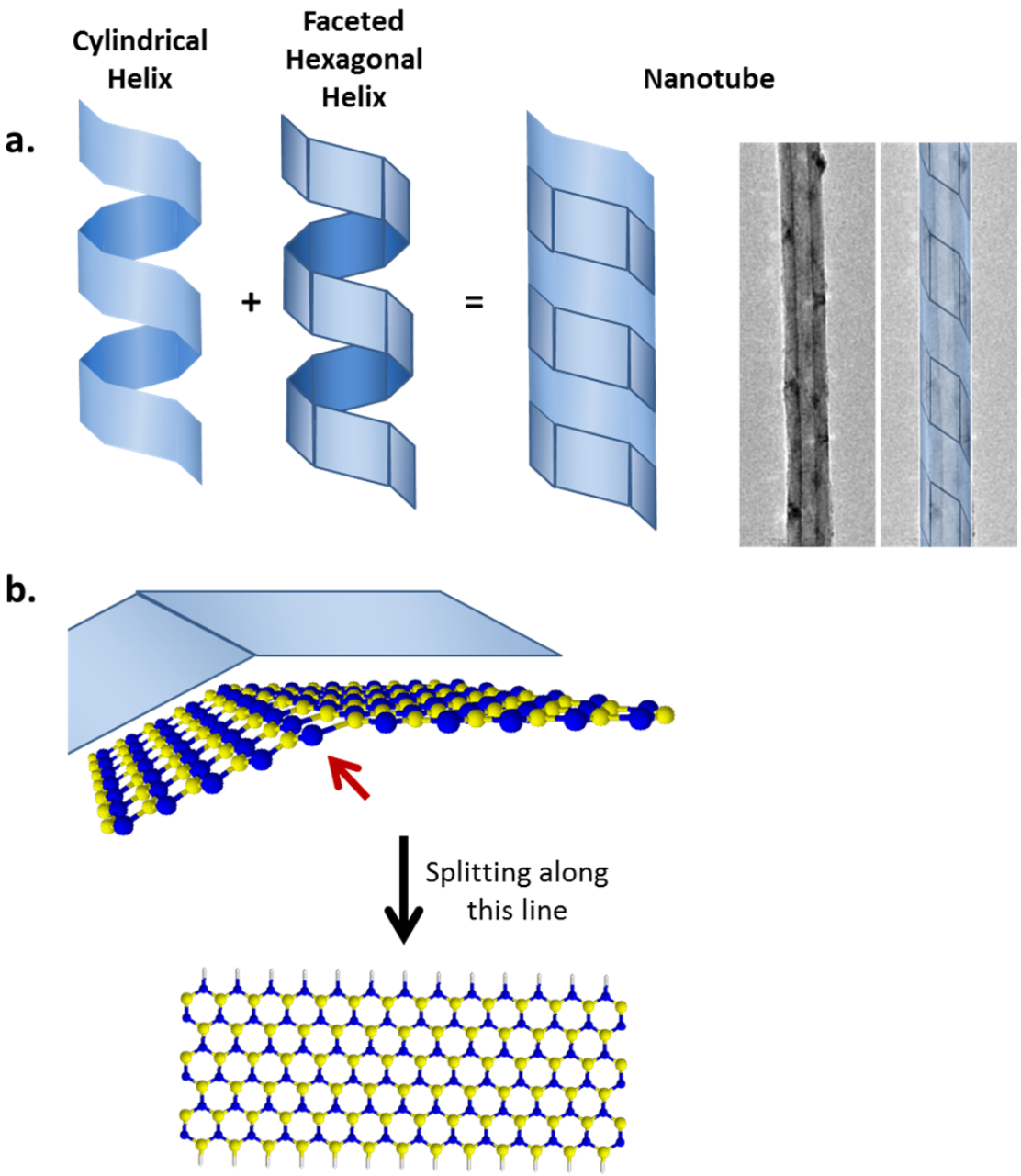

Figure 3-12. **a.** Representation of the two different helices present in many BNNTs with the continuous helix representing the cylindrical portion of the tube and the segmented helix representing the faceted hexagonal planes with the two adding together on the right to form a double helix structure,[133] similar to that seen in the TEM micrograph of the BNNT to the far right, which has this double helix formation overlayed on the far right to aid in understanding of the structure. **b.** Representation of two planes of hexagonal boron nitride meeting and adjoining at a facet (planes above the atomistic representation help in indicating where within the structure of a. these formations exist). Red arrow points to the line of boron atoms which would be highly acidic under this strained configuration. Below, the BNNR that could be produced if potassium were to react with the line of boron atoms as discussed above following a water or ethanol quench. In this BNNR, hydrogens are attached to both edges of the BNNR, given the understood edge functionalities for the quenching solutions used. This BNNR perfectly matches a theoretically considered BNNR.[98]

To understand the mechanism of splitting, a further look at the bonding structure of BNNTs is instructive (Figure 3-11a). A significantly larger interplanar interaction exists between walls of a BNNT compared to CNT walls as polar boron-nitrogen in-plane bonds result in AA' stacking between planes to allow heteroatoms from adjacent walls to align.[132] This often results in all walls of a BNNT being of nearly the same chirality, unlike the random chiralities found in CNTs, which maximizes the overlap between boron and nitrogen atoms in adjacent walls.[132] However, the commensurate stacking cannot continue around the full circumference of a tube given the changing diameter of concentric tube walls. A thorough TEM diffraction study[133] revealed that this geometric constraint often results in tubes that are formed in a double helical fashion. One helix consists of walls which are AA' stacked and flat, with facets along the helix. A second helix completes the tube which has consecutive walls that are mismatched and not AA' stacked. The crystalline helix causes characteristic diffraction peaks of a faceted, polygonal structure whereas the lower crystallinity helix causes diffraction peaks characteristic of a cylindrical structure. Finally, within the highly crystalline faceted helix, lines of strained sp^3 bonds connect each facet, on the order of 6 facets around the tube, with these lines running parallel to the longitudinal axis of the tube (Figure 3-11a,b).[133]

We propose that due to the observed highly linear edges of our BNNRs, potassium likely preferentially intercalates near these higher energy lines of sp^3 bonds connecting facets and eventually begins splitting along these lines (Figure 3-11b). Splitting then propagates down the tube following these lines of weaker bonds, also inducing splitting through the mismatched structure regions. This splitting along predefined lines within the BNNTs explains the high quality, linear edges that are seen on the BNNRs. Also, boron atoms along these lines would be highly acidic with enhanced reactivity towards electropositive potassium, allowing for easier splitting along the lines. Furthermore, a larger interplanar spacing exists along these lines of sp^3 bonds likely allowing for more facile intercalation into these regions. Finally, intercalation likely facilitates exfoliation of unzipped walls as it disturbs the interplanar interaction between the BNNT walls. Splitting under these conditions could produce BNNRs that exactly match theoretically considered BNNRs (Figure 3-11b).[98] Splitting through this process should not introduce defects within the ribbon plane, as we have observed with our BNNRs. As with most nanomaterials, each particular BNNT varies significantly from the next in terms of overall structure and geometry. Therefore, although this mechanism is proposed, it is understood that the splitting to form each ribbon is highly dependent upon the particular characteristics of the parent tube and much more complex mechanics may occur to allow for each individual ribbon to form.

Since BNNTs will often form in either zigzag or armchair orientation,[132] the longitudinal splitting of BNNTs seen in this study may result in a high proportion of ribbons with zigzag and armchair edges (Figure 3-4) as opposed to other edge orientations. This is especially exciting given the significant body of theoretical work done on BNNRs requiring edges with minimal defects and usually of zigzag orientation.[93, 94, 96-98] Predicted properties for BNNRs include metallic or semi-conducting electronic states, which can be magnetically polarized,[53, 91, 93, 94, 96, 98, 99, 120] as well as edges displaying ferromagnetism or antiferromagnetism,[94, 96, 98, 99] all of which are dependant upon edge geometry and termination. Given this significant dependence upon

BNNR edges for imbuing particular electronic and magnetic properties, the high likelihood of synthesizing ribbons with zigzag edges may make them particularly suitable for addressing theoretical predictions and realizing proposed applications. It is also worthwhile to consider the possibility of functionalizing the edges of these BNNRs. GNR edges synthesized via this route are potassium terminated during synthesis and hydrogen terminated upon exposure to water or ethanol.[88] BNNRs synthesized through this route could be similarly terminated, and many of the predicted BNNR properties necessitate hydrogen terminated edges.[94, 96-98, 100] Furthermore, the reactive potassium terminated edge could easily be replaced with species other than hydrogen. Different chemicals could be used for quenching to impart other terminations. In addition, hydrogen could be replaced after quenching by either utilizing established boron nitride functionalization routes[144, 145] or by devising new routes unique to the highly reactive nanoribbon edge.

Chapter 4: Hexagonal Boron Nitride

The significant interest in graphene has heralded in a mounting interest in other 2D-crystals,[146] especially hexagonal-boron nitride (h-BN), which is a material very closely resembling graphene. Instead of a two carbon atom unit cell, the h-BN unit cell consists of a boron and nitrogen atom, making it isoelectronic with graphene such that similar sp^2 bonding exists in this material, which also forms a 2D hexagonal lattice resembling a honeycomb. Subtle differences exist between the bonding structure of h-BN and graphene, as indicated in Table 4-1.

	Graphene	Hexagonal Boron Nitride
Bond Length (d)	142 pm	145 pm
In plane lattice Spacing (a)	246 pm	250 pm
Interlayer Distance (c)	335 pm	333 pm
Bond Order	1.33	~1.22

Table 4-1. Small differences exist between the graphene and hexagonal boron nitride bonding structure.

One of the most significant differences in Table 4-1 is the difference in bond order between these two materials. This arises as the two extra electrons on the nitrogen atom after forming the initial sp^2 bonds are not perfectly shared in a π bond, like in graphene, but instead partially remain on the nitrogen atom, given is higher electronegativity than boron . The electronegativity difference between these two atoms also polarizes the sp^2 bonds such that a partial negative charge exists on the nitrogen atom and a partial negative on the boron. This polar bond, and also different orbital ionization energies of boron and nitrogen *2p* orbitals, results in h-BN having a large band gap (~5.9 eV)[147] compared to the zero-gap which graphene exhibits.

4.1 Applications of h-BN

Many various applications of h-BN can be envisioned. Given its single atom thickness, h-BN is of interest as a thin dielectric (indeed, the thinnest possible dielectric).[148] h-BN has also been seen to be an ideal substrate for graphene (enhancing the mobility of graphene significantly over a similar device where graphene is deposited onto a silica substrate).[12, 149] There is also interest in its usage as a very high quality factor mechanical resonator, potentially having a Q-factor larger than already promising graphene resonators,[150] given the lack of energy dissipation with its large band gap. There is also significant interest in creating hybrid structures whereby a single atomic sheet consists of graphitic portions and h-BN portions bonded together in various geometries.[106, 107, 117-126, 151] Further interest along these lines includes interest in the synthesis of a as stoichiometric BCN material with, for example, a BNC_2 unit cell, which could result in materials with band gaps intermediate between hexagonal boron nitride and graphene,[152] which will be discussed more in-depth later on. h-BN also has significantly higher stability in oxidative environments, so interest in h-BN layers for passivation has been significant for many years.[153]

4.2 Syntheses of h-BN

To realize the potential applications of h-BN, thin h-BN layers (ideally from sub-monolayer upwards to multi-layer materials) must be synthesized. Indeed, a significant body of work exists at this point with syntheses of single sheet h-BN being accomplished on single-crystal transition metal substrates.[90, 147, 154-188] Most often these studies use the molecule borazine ($B_3N_3H_6$, the boron nitride equivalent of benzene) as the boron and nitride source,[90, 147, 154-183] but sometimes other boron and nitrogen sources are used.[184-188] Certain requisite aspects of these syntheses are not desirable in terms of producing a material suitable for the above-mentioned applications. For non-academic purposes, the material produced is not suitable given that the syntheses requires ultra-high vacuum (UHV) conditions such that very low doses of borazine can be used (only 40 Langmuirs; 1 L = 10^{-6} torr*s, or the dosage necessary to give a monolayer of a perfectly sticking adsorbate) and the growth substrate must be a single crystal. These studies all utilize a single crystalline substrate, given the preferential growth of h-BN on particular crystalline faces, but in order to be utilized for its proposed applications, the synthesized h-BN must be liberated from the catalytic growth surface. This is common practice for graphene syntheses where the copper substrate for graphene is dissolved away to liberate the graphene layer. However, for single crystal substrates which have commonly been used for h-BN synthesis, this idea comes across as absurd as single crystalline substrates are prohibitively expensive to simply dissolve away (even in the best funded research labs!). Given this, it is of great interest to design a synthetic technique for the synthesis of few layer (down to sub-monolayer) h-BN in a way which could be commercially viable: without a single crystalline substrate and not under UHV conditions.

4.2.1 Current non-UHV Approaches

To develop a scalable method for the synthesis of few layer h-BN, the graphene synthetic advances are informative to consider. Indeed, quality graphene can now be synthesized in such a manner through the non-UHV CVD decomposition of carbonaceous precursors onto a transition metal foil.[10] Using this approach, inexpensive metal foils could act as the catalytic surface where boron and nitrogen precursors could decompose and growth h-BN crystals under non-UHV conditions. Indeed, work has been done attempting to synthesize such materials, with some notable successes of thicker h-BN material[147, 189, 190] synthesized through CVD methods on Cu and Ni foils, with a recent success of sub-monolayer to monolayer growth of h-BN on Cu foil.[191]

The main difference between the previous CVD h-BN syntheses of thicker material and the latter success of synthesizing single layer h-BN is in regards to the precursor molecule. For the previous studies, borazine was either used directly or made in-situ through the decomposition of ammonia borane (BH_3NH_3) by heating it at ~120 °C.[147, 189, 190] The latter synthesis decomposed ammonia borane at ~80 °C yielding amino borane (BH_2NH_2), which presumably is stable at the reaction temperatures (although this molecule is devastatingly understudied), becoming the main precursor material for h-BN growth in the CVD chamber. It seems that with this alternative precursor, many difficulties with the h-BN synthesis via borazine are bypassed, as high quality thin h-BN sheets via borazine using a CVD method have not yet been established. However, usage of this precursor is as of yet far from optimal. The synthesis employed is completely non-reproducible as the dosage of this precursor is completely unknown (and the precursor itself is proposed, but certainly not determined) and achieving the low doses required for monolayer or sub-monolayer growth proves very challenging. Indeed, CVD processes utilizing solid precursors is a challenge to begin with, in terms of determining dosages of the precursor molecule, and when the precursor is actually a decomposition product of a reagent, this challenge is significantly enhanced.

4.2.2 Considerations for CVD Growth of h-BN

Some of the difficulties with the non-UHV, CVD approach for synthesizing h-BN should be outlined. The metallic foil being used for the synthesis has high roughness as purchased, unlike high quality single crystal substrates used in the UHV studies. Therefore, different reaction rates will occur on the different crystal faces, making homogenous numbers of layers of h-BN difficult to achieve, and significant roughness can result in much thicker regions around rougher regions where nucleation is significantly enhanced. Also, much higher doses of borazine will almost necessarily be used at non-UHV conditions. It is desired that a simple rough pump could provide sufficient vacuum for h-BN growth, yet the doses used in UHV studies of 40 L with multi-layers forming at a few thousand langmuirs, meaning that with a base pressure of 1 mTorr (optimal conditions for a rough pump) and a resultant measurable partial pressure of borazine near that base pressure, borazine can only be dosed for under a second. This sort of synthesis would be absurd to attempt given the time required for equilibrium to be established in a complex CVD system, so notions of how to artificially lower the

borazine dosage must be considered (although with the CVD setup which will be described, partial pressures of borazine below the base pressure are possible). One approach is to introduce H_2 into the system as H_2 competitively etches h-BN as it is growing,[164] and it also allows for h-BN to grow over step edges on a crystal surface,[164] which is very important on a rough surface like the metal foils commonly used for CVD syntheses. Considering all this, H_2 should be flowed during the synthesis, and a moderately higher temperature (~ 900 °C instead of ~750 °C) should be used to account for the decreased reactivity of non-preferred crystal faces which will be exposed on the metal foil surface.

Carbon contamination is also a major concern when synthesizing h-BN under non-UHV conditions. Given a moderate base pressure, vapor phase carbon sources can still exist in quantities sufficient for graphene to grow instead of h-BN given the very similar reaction conditions used and the fact that graphene will growth preferentially to h-BN when any carbon contamination exists. Therefore, the reaction system must be kept relatively free of carbonaceous materials (no decomposition of carbon should be done in a h-BN CVD systems), a liquid nitrogen trap should always be used when the rough pump is on (such that back-flow of pump oil does not occur), and the substrate must be completely void of carbonaceous materials (a UV ozone or O_2 plasma treatment of the substrate should be done prior to insertion of the substrate into the CVD system).

Oxygen also plays an important but detrimental role in the CVD synthesis of h-BN. The foils used with have a native oxide layer which must be reduced prior to BN precursor introduction, which is effected via hydrogen flow to reduce the metal surface. Small pressures of oxygen are also likely in the system during growth as a portion of the base-pressure is assumed to be residual oxygen and mild leaks presumably exist in the system, but are mostly undetectable given the moderate base-pressure created by the rough pump. Given this, H_2 (again) is continuously flowed during the h-BN synthesis. Also, the effect of O_2 on the growing h-BN material must be considered as it has been shown that very small doses of O_2 will result in the formation of boron-oxygen compounds which degrade the crystallinity of the h-BN.[162] In this work,[162] low doses of ammonia were used to reverse the oxidation of the h-BN layer and exploring this approach would likely be worthwhile.

4.3 CVD Design for h-BN Synthesis

To develop a scalable method for the synthesis of few layer h-BN, I designed a CVD system for the synthesis of thin h-BN films (Figure 4-1) which was created with the intent of it being versatile such that syntheses of other carbonaceous and boron nitride based nanomaterials (specifically BCN hybrids as well) would also be possible.

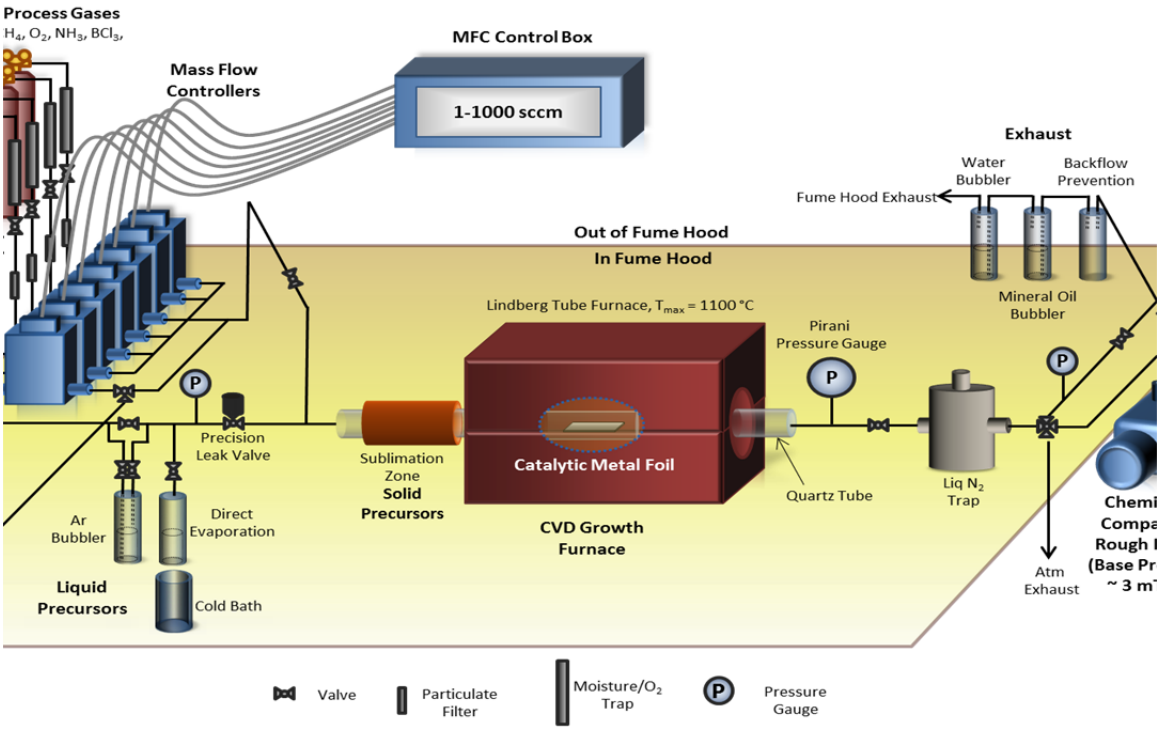

Figure 4-1. CVD designed for h-BN synthesis as well as for other related carbonaceous and boron nitride materials. Details in the text.

With this CVD system, a few key features were desired to present which necessitated many design elements. The system was designed to allow for corrosive reagents. To account for this, proper mass flow controllers were required as well as a chemically compatible pump, and the exhaust system was designed to neutralize these reagents. The system was made such that gaseous, liquid, and/or solid precursors could be used, resulting in the solid and liquid precursor zones indicated in Figure 4-1 as well as the numerous gaseous precursor tanks. The liquid precursor section was designed to accommodate for ambient pressure syntheses, where a bubbler containing a liquid is subjected to positive pressure carrier gas flow, or vacuum pressure syntheses (down to ~3 mTorr), where a closed container houses the liquid which is evaporated and introduced into the CVD system through the pressure gradient created by the vapor pressure of the liquid precursor and the vacuum on the other side of a leak valve. The liquid nitrogen trap helps the system to remain carbon-free during growths, and the precision leak valve allows for very low dosages of liquid precursor material (specifically borazine).

4.4 CVD h-BN Synthesis

Using the CVD system previously describe (Figure 4-1), the synthesis of thin h-BN was undertaken. Reaction conditions were unfortunately not optimized during my doctoral studies, so a general approach will be outlined and specifics about one particular synthesis will also be specified with its results analyzed.

4.4.1 General Reaction Conditions for CVD h-BN Synthesis

In general, Cu and Ni metal foils (25-250 μm thickness, 99.9+% purity) were annealed prior to usage at 1050 °C for Cu and 1200 °C or 1410 °C for Ni under flowing H_2 at atmospheric pressure for 12 hours, to allow for smoothing of the surface. These foils were soaked in concentrated HCl (for Cu) or 1 M HCl (for Ni) for 20 seconds prior to use and rinsed thoroughly with DI water. Following this washing, foils were placed in a UV-ozone generator and ozone treated at 100 °C for 10 minutes. Foils were quickly placed in a quartz tube and evacuated on in the CVD system after filling the liquid nitrogen trap. The borazine was attached to the system and solidified with a chloroform slush. The borazine container was then evacuated upon until a base pressure was reached. This was done specifically to remove any ammonia that formed from borazine decomposition as well as any argon which may have been used with the borazine previously. The borazine is then warmed in a acetonitrile slush or other suitable slush to determine its vapor pressure according to the empirical formula,[192]

$$P = 10^{7.714-1609/T} \qquad \text{Equation 4-1}$$

Where P is the vapor pressure in Torr of borazine and T is the temperature in Kelvin.

The borazine can then be diluted with Ar up to atmospheric pressure to dilute the incoming borazine stream with inert Ar. Under flowing H_2 (30 sccm), the CVD oven was warmed to the annealing temperature of 1050 °C for Cu or 1100 °C for Ni at the maximum heating rate. After allowing the substrates to anneal for 20 minutes, the CVD oven was allowed to slowly cool to the reaction temperature of 850-1000 °C. The leak valve was then used to allow borazine precursor gas into the system at a pressure of 1-15 mTorr (for both borazine and any Ar dilutant). The H_2 flow rate was changed during the growth to 0-100 sccm. The growth was done over the course of 2-20 minutes. The borazine and H_2 flows were then stopped and the system was allowed to quickly cool to room temperature. Foils were then adhered to a TEM grid[193] using a drop of IPA and etched in $FeCl_3$ (0.1 g/mL) over the course of 6 hours. The TEM grid with the adhered h-BN layer was then transferred to 100 mL of DI water and allowed to set for 15 minutes. This process was repeated twice. The grid was then removed from the water surface and allowed to air dry (Figure 4-2).

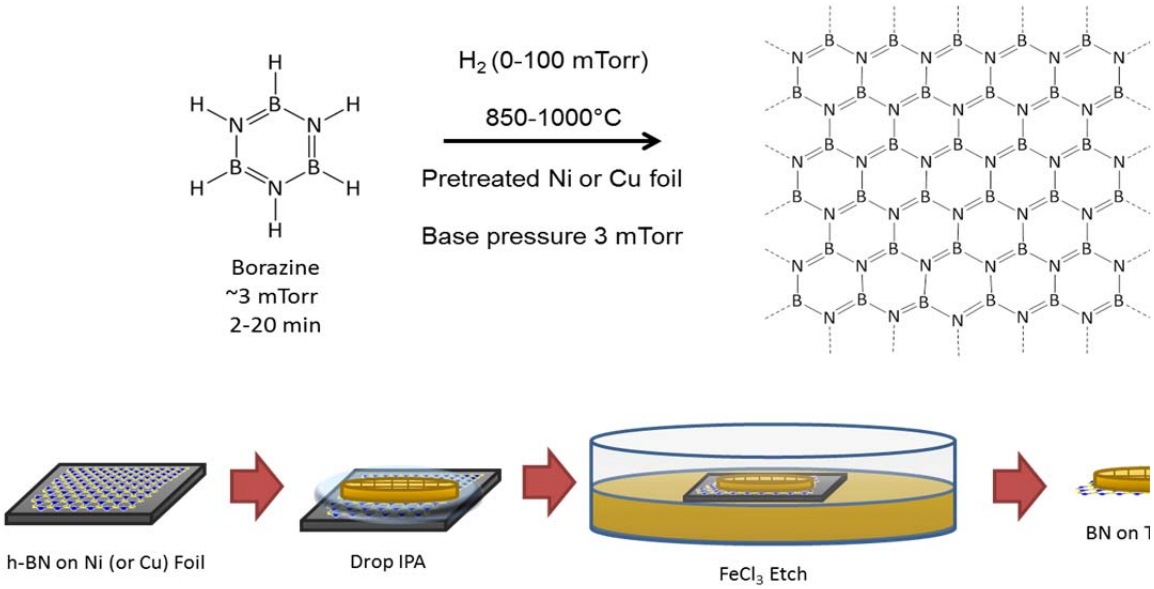

Figure 4-2. Synthetic approach for h-BN synthesis (above) and transferring the h-BN material to a TEM grid for analysis (below).

4.4.2 Specific Reaction Conditions for a CVD h-BN Synthesis

Specifically, for the h-BN growth closely examined here, the synthetic conditions were as follows. Ni foil was heated in the CVD chamber directly to 1100 °C (over 30 minutes) under flowing H_2 (100 sccm), kept at 1100 °C for 20 minutes and cooled to 900 °C for the growth. The H_2 flow rate was decreased to 20 sccm and borazine was introducted into the system (6 mTorr) for 6 minutes. The borazine and H_2 streams were then stopped and the chamber was allowed to cool to room temperature quickly (by opening the CVD oven). The material was then prepared for TEM analysis as described above.

4.4.3 Analysis of CVD Synthesized h-BN

CVD synthesized h-BN can be characterized before removal of the catalytic substrate via Raman spectroscopy. Figure 4-3 indicates the highly crystalline nature of the h-BN material showing the expected peak at 1367 cm^{-1} for 514 nm laser excitation energy.[147]

The crystallinity of the material can be further verified via electron diffraction as indicated in Figure 4-4b. Little other signal is observed in this electron diffraction pattern as the aperture in the imaging plane was defined such that residual nanoparticles from the synthesis (Figure 4-4a) were not included, and this diffraction indicates that any multi-layers that were formed were of the same orientation as all other layers. A highly electron transparent film is seen to cover the quantifoil TEM grid in Figure 4-4a with some nanoparticles on top of the film. The nanoparticles were from the incomplete

annealing of the catalytic Ni substrate (a process still being optimized) and the material is not a single sheet thick, but closer to 3-6 layers, as determined from ripped and scrolled regions near to the one shown in Figure 4-4.

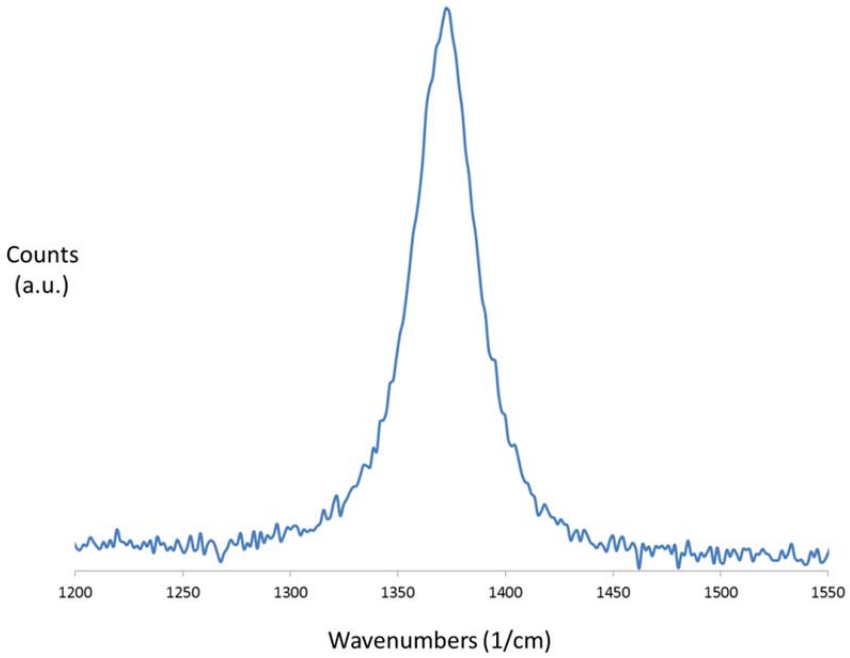

Figure 4-3. Raman analysis of h-BN material synthesized through process described in the text using a 514 nm laser. A singular peak centered at 1367 cm^{-1} indicates the highly crystalline nature of the h-BN material.

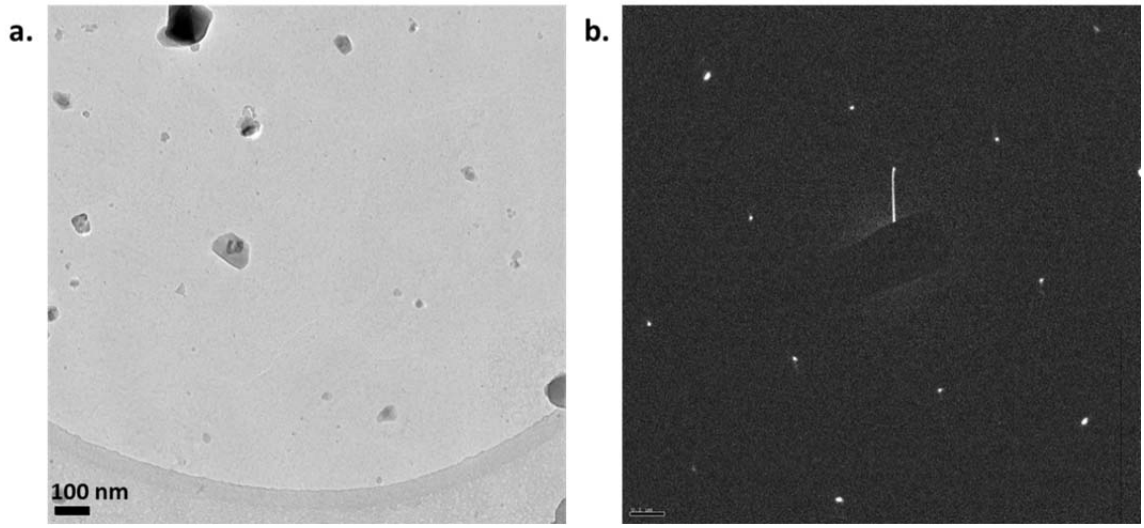

Figure 4-4. **a.** TEM micrograph of the h-BN material described in the text, which is highly electron transparent except for the remaining nanoparticles on its surface. **b.** Electron diffraction pattern of a small region of (a) indicating the highly crystalline nature of the h-BN material.

4.4.4 Assessment of CVD h-BN Syntheses

Significant work still needs to be done to optimize the synthesis of CVD h-BN. Some main concerns include achieving a properly smoothed surface, optimizing the H_2 flow rate, determining if annealing is necessary and flow conditions for during it, and how to get sub-monolayer to monolayer growth.

For a properly smoothed surface, Cu foils can easily be smoothed using the annealing conditions previously specified, but smoothing of Ni foils seems more challenging owing to the higher temperatures necessary and the pitting which often forms when annealing Ni foils under flowing H_2. Work optimizing this step is needed and electropolishing of the Ni foil may be a suitable approach for achieving this.

Given the multiple roles H_2 plays during CVD h-BN growth, the flow rate and ratio with the borazine precursor must be optimized. H_2 flow can also be useful for competitively etching lower crystallinity boron nitride materials which grow on the substrate, so studying how H_2 etches an existent h-BN layer would be very useful. Use of NH_3 during the growth may also prove helpful given that oxygen in the system would result in removal of nitrogen from the h-BN plane.

Finally, annealing of the material could be helpful given that crystalline materials are more difficult to obtain on the metal foil substrates used. However, great care must be taken when doing anneals as Ni substrates can dissolved h-BN layers at elevated temperatures (>900 °C).[174] Assessment of annealing, especially during with H_2 flow during the anneal, could be very helpful in understanding how this synthesis can be optimized.

4.5 Atomic Resolution Imaging of CVD Synthesized h-BN

Although the samples previously described (Section 4.4) were not monolayer h-BN samples, thicker samples can also be useful for high resolution microscopy analysis as the material can be thinned using a combination of electron beam exposure as well as attaching the material to a heating stage to facilitate controlled decompositions of the material. For use on a heating stage specifically designed for the TEAM 0.5 at NCEM at LBNL, h-BN was transferred to a silicon nitride window substrate with holes etched in the substrate such that high resolution analysis could be done through thin samples. The substrate was then heated to 800 °C in the TEM and left for an hour. The substrate was then cooled to 400 °C to allow for proper imaging, as imaging at elevated temperatures resulted in great instability of the material. Individual regions were then thinned by keeping the electron beam on the region of interest for ~20 minutes until the region thinned down to a distinguishable number of layers.

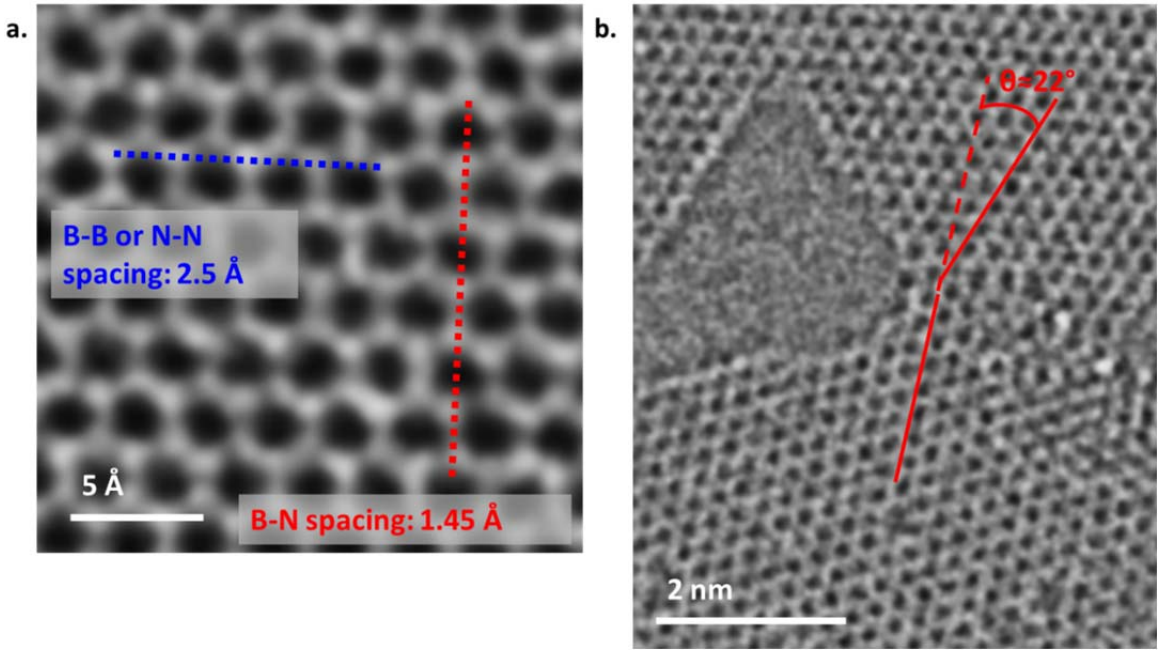

Figure 4-5. High resolution electron micrographs of **a.** a bilayer of CVD synthesized h-BN showing the highly crystalline nature of the material with the expected spacings between the atoms as indicated, and **b.** a monolayer of h-BN with a grain boundary between two crystals of h-BN. The angle between these two crystals is ~22°.

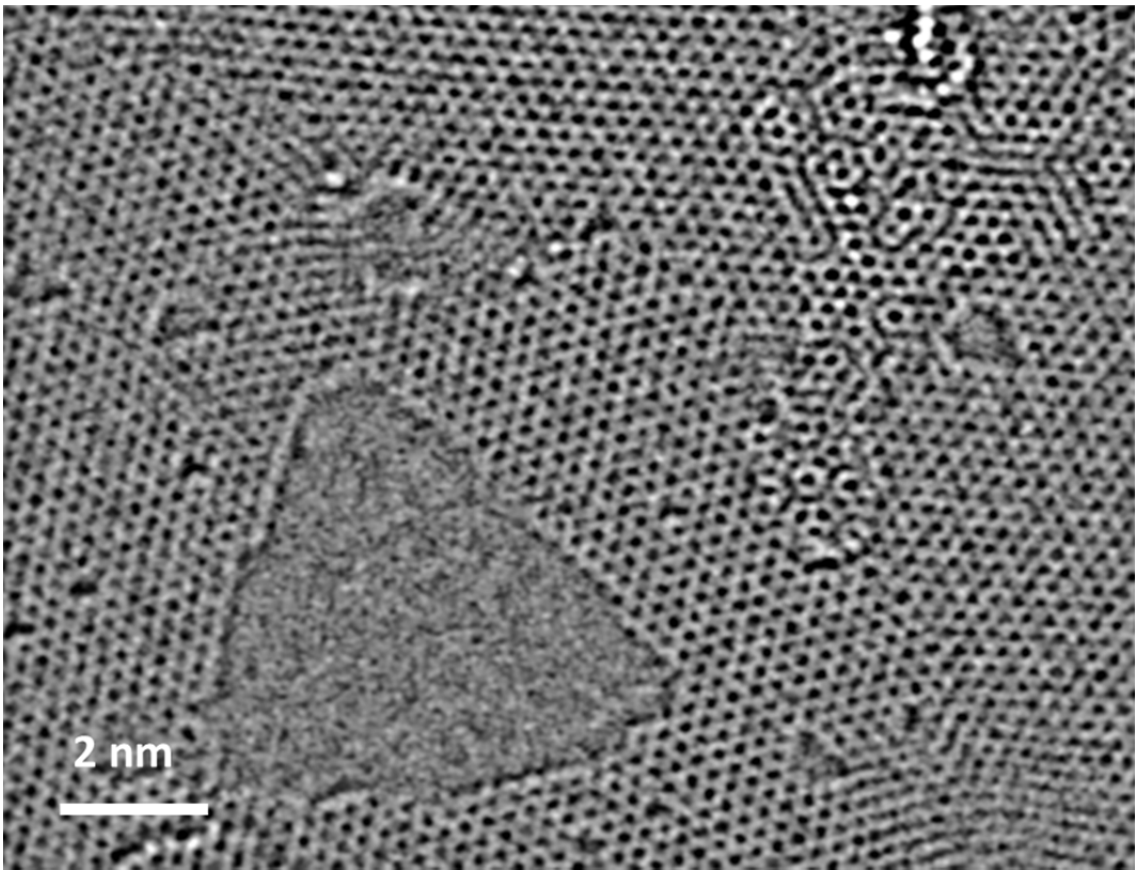

Figure 4-6. High resolution electron micrograph of a larger region of single sheet CVD grown h-BN.

Using this technique, thicker h-BN samples could be thinned down to few layers including monolayers (Figure 4-5 and Figure 4-6). This material then becomes ideal for analysis and includes features common for h-BN materials under electron beam irradiation including triangular defects of various sizes (down to single atom vacancies) with a preferred zigzag edge.[194] Previously unseen features include grain boundaries as the synthesized material is a polycrystalline h-BN sample. These features have not been previously reported and identification of the local bonding structure within these regions is of great interest especially considering that carbon contamination could have incorporated itself within these high energy grain boundaries. Understanding these grain boundaries is also of great interest as their understanding would greatly inform approaches to creating hybrid graphene/h-BN materials where these boundaries would be a dominant feature.

4.6 CVD Synthesis of Planar BCN Materials

The CVD system I designed was also created for the synthesis of planar BCN materials. The synthesis of a hybrid carbon, boron and nitrogen hexagonally structured materials is of great interest to researchers, especially for applications within electronics as this material should have a bang gap intermediate between that of graphene and h-BN.[152, 195] Indeed, if the ratio of carbon to boron and nitrogen could be tailored, without undermining electronic properties of the resultant material, band gaps ranging from 0-5.9 eV could be possible with a material still possessing promising transport properties, making such materials useful for an indiscriminately large number of applications. However, recent attempts at synthesizing this sort of material have proven unsuccessful[152] as a stoichiometric material where carbon, boron and nitrogen are homogenously intermixed within the plane is thermodynamically unfavorable as sections of graphitic material intermixed with sections of boron nitride material is the most energetically favorable case.[196] However, a significant body of previous literature exist which makes a believable argument for the synthesis of more stoichiometric planar BCN material.[197-200] With all of these studies, the XPS data differed significantly from the XPS data in the Ajayan work. This data indicates that with the Ajayan results, carbon is almost solely bonded to carbon, boron to nitrogen, and nitrogen to boron. However, XPS from these other works indicates a significant amount of bonding between carbon and boron, carbon and nitrogen, boron and carbon, and nitrogen and carbon which would indicate mixing of the graphitic and boron nitride regions into perhaps a more stoichiometric phase.

The question then must be asked of what the major synthetic difference between these studies was. The answer is apparent when considering the reactants used for the syntheses. With the Ajayan work, a boron and nitrogen containing compound (ammonia borane) was decomposed onto a Ni catalytic substrate with methane as the carbon source.

With the previous works, separate boron and nitrogen sources were used (the precursor did not have a boron-nitrogen bond), and in fact with some of the more successful syntheses, a molecule with strong carbon-nitrogen triple bond was used (acetonitrile). Given this and the tendency of carbon to segregate into discrete graphitic regions and boron and nitrogen into discrete boron nitride regions, a very strong bond in the precursor which effectively draws the boron nitride and carbonaceous phases into each other seems to be the reason that these seemingly similar studies had completely different results.

4.6.1 Planar BCN Synthetic Approach

The synthesis of a stoichiometric BCN material was undertaken which took into consideration the previous approaches to synthesize BCN materials (Section 4.6). Ni foils were prepared similarly to those used for the h-BN study. These foils were then inserted into a quartz tube and attached to the CVD system. A container with acetonitrile (dry, 99.9%) was attached to the CVD system, the acetonitrile was condensed with liquid nitrogen and evacuated upon to remove nitrogen (from the glove box preparation of the acetonitrile container) and vacuum grease for the o-rings. The BCl_3 tank was opened and the pressure down-stream from the BCl_3 regulator was slowly increased until a slight pressure over vacuum was noticed. It should be noted that BCl_3 should never sit in the stainless steel lines, especially if in contact with the mass flow controller (MFC). Although the MFC attached to the BCl_3 is specially designed for corrosive gases, prolonged exposure to corrosives will greatly decrease the lifetime of the MFC. The outlet side of the BCl_3 regulator should also only be at a slight pressure over vacuum as that is sufficient for MFC operation, yet minimizing the usage of BCl_3 is very important (as will be understood shortly). The liquid nitrogen trap is cooled and the system is evacuated to vacuum pressure. The bubbler system was then activated such that any exhaust (specifically in mind the BCl_3 exhaust) travels through a mineral oil bubbler and then a large water quench container (see Figure 4-1).

The CVD oven was then heated to 1100 °C under flowing H_2 (100 sccm), held at 1100 °C for 30 minutes and then cooled to 1000 °C for the synthesis. H_2 flow was then completely stopped and must remain stopped during any BCl_3 flow (otherwise HCl gas is formed and the CVD system will be compromised). The BCl_3 flow was then started (3 sccm) and the leak valve to allow acetonitrile flow was opened until an equivalent pressure over base pressure of the BCl_3 flow was achieved (~20 mTorr for each, ~45 mTorr total). These two precursors were flowed for 10 minutes after which both were stopped and the system was allowed to cool to room temperature.

The BCl_3 which did not react in the hot zone was then condensed on the liquid nitrogen trap. After closing the valve on the upstream side of the trap, the liquid nitrogen trap (still under vacuum) was warmed. After it was warmed, all the BCl_3 was out of the CVD system, except for the BCl_3 which dissolved in the pump oil (which seems to be a very significant amount). Given this, the pump must be run for an additional 12 hours to circulate out the BCl_3. This process can be speed up by shocking the pump with high flows of Ar to force out BCl_3 at an accelerated rate. However, this still must be iterated numerous times before BCl_3 is completely removed from the pump oil, so the 12 hour run is recommended.

The material synthesized as specified did not display any Raman signals or was it mechanically robust enough to transfer to a quantifoil TEM grid for analysis. However, it did display equal EDS signal for the boron, carbon, and nitrogen Kα lines, indicating some sort of hybrid BCN material. Although the material was likely carbon poor given the equivalent EDS signal as the material as envisioned should have had a BC_2N stoichiometry. Significant work still needs to be done to optimize this synthesis, especially choosing a temperature at which a properly annealed material results.

Chapter 5: High Surface Area Boron Nitride for H_2 Storage

Hydrogen as a potential commercial scale energy source has been considered for many decades[201] and has seen a renewed interest given the recent heightened concerns about global warming and the exhaustible supply of oil. Usage of hydrogen as a mobile fuel source, especially for motor vehicles, is particularly appealing as the by-product from either the combustion or electrochemical consumption of H_2 is simply water instead of CO_2, a greenhouse gas, as well as NO_x and SO_x, the molecules responsible for acid rain, all of which are common by-products of gasoline combustion. The energy density (MJ/kg) and volumetric energy density (MJ/L) are inferior compared to gasoline,[202] but this trade-off is somewhat mitigated considering that fuel cell technology likely could be utilized for H_2 consumption at upwards of 60% efficiency compared the ICE efficiency for gasoline at 22%.[202] When considering the source and storage of H_2, the overall efficiency of the process will be much less, with current electrolysis technology at upwards of 80% efficient and compression of H_2 (being the most common current storage means for vehicular use of H_2) at around 90% for a maximum efficiency of more around 43%. Electrolysis could eventually be a more carbon neutral production method for H_2, but presently numerous routes for H_2 production are available, and around 90% of H_2 comes from the reforming of fossil fuels.

Technologies for the storage of H_2 are very important to realize the usage of H_2 as a vehicular energy source as the current approach of compression is not feasible for most vehicular uses. Very high pressures are required to compress H_2 to densify it sufficiently such that the storage container takes up a reasonable volume. Common methods pressurize H_2 to 300-750 bar, but as can be imagined, vessel creation to accommodate these pressures is challenging and shape prohibitive, which becomes a big concern when considering usage in mid-small size vehicles.

The two other perhaps more practical approaches for storage are chemiosorptive and physiosorptive storage. The first method, chemiosorptive, utilizes compounds which are hydrogen rich, like ammonia borane,[203] which can be decomposed to a compounds which has released hydrogen. With this approach, high weight percents of hydrogen can be stored (one of the most crucial metrics for determining a promising hydrogen storage material) of up to 19.6 wt% in the case of ammonia borane, and required pressures are very low. However, the thermodynamics of the reverse process are often limiting given the usual exothermic and entropically favorable release of hydrogen being coupled with an endothermic, entropically unfavorable storage of hydrogen, making the latter process thermodynamically impossible. There are cases of endothermic release of H_2 or a highly endergonic reaction could be coupled to the storage of hydrogen, but in general these approaches have many fundamental challenges to overcome.

5.1 Physiosorptive Storage of H_2

Physiosorptive storage is another method for storing hydrogen which involves the physical bonding of hydrogen to a high surface area adsorptive medium such that at moderately high pressures (<100 bar), a sufficient amount of H_2 can be stored. The thermodynamics of this process are more favorable, but high weight percents of hydrogen being stored becomes the main challenge. Not only must a material have a very large surface area for adsorption of hydrogen, but also an optimal enthalpy of adsorption must occur, being 15-25 kJ/mol (being within the range of a typical hydrogen bond: a very strong intermolecular interaction) for ambient temperature storage at 30 bar and release at 1.5 bar[204] (although the assumption of necessitating conditions similar to these for storage and release may not be completely valid as the temperature likely could be lowered significantly by degassing the storage container slightly). Some very high surface area metal organic frameworks (MOFs) and covalent organic frameworks (COFs) have been developed having surface areas of up to 6240 m^2/g in the case of MOFs[205] and 6460 m^2/g in the case of COFs,[206] resulting in impressive hydrogen storage capacities of up to 9.0 wt% at 77 K and 40 bar.[207] However, optimal bonding energies are not always achieved with these systems, and alternative materials are of interest for physiosorptive hydrogen storage.

5.1.1 High Surface Area Carbonaceous Materials

A material potentially suitable for the physiosorptive storage of H_2 is high surface area carbon. Using this sort of material for H_2 storage could potentially be more commercially viable and has seen some recent successes. However, random pore geometry high surface area carbonaceous materials show poor hydrogen storage capacity, with high surface area activated carbon, having a large surface area of 3000 m^2/g, only exhibiting a storage capacity of 1.5 wt%.[208] However, forced liquefaction of pores during adsorption can occur with smaller pore size microporous materials (< 2 nm pore diameter) resulting in much higher hydrogen uptakes, ~2-7 wt%, of similar surface area carbonaceous materials which have been template grown off a small-pore zeolite.[209-211] With this method, a carbonaceous precursor is decomposed onto a microporous zeolite template. Following annealing of the hybrid material, the zeolite template is dissolved and removed resulting in an inverse structure of the original zeolite which consists of pure carbon. This results in a material with a similar pore geometry but of much lower density (with it consisting of only carbon instead of mainly oxygen, silicon and aluminum in the case of the zeolite) yielding a much higher surface area (reported in area per mass). In general a direct correlation usually exists between surface area and hydrogen storage capacity,[212] but the templating of materials off a microporous framework has shown great exceptional promise. As of yet templated high surface area materials have mainly been created with carbonaceous precursors.

5.2 High Surface Area Boron Nitride as a H_2 Storage Medium

Boron nitride based materials have been shown to have a much higher hydrogen uptake given the polar bond existing between boron and nitrogen in these materials compared to the non-polar carbon-carbon bonding in carbonaceous materials.[213, 214] Indeed, comparing two similar studies where CNT material and BNNT material exhibited very similar surface areas, there was around a 4-fold increase in storage for BNNTs compared to CNTs.[215, 216] However, the synthesis of very high surface area (> 1,000 m^2/g) boron nitride materials with a well-defined microstructure has not yet been done (although one group has shown significant interest in mesoporous boron nitride structures, but the usage of a precursor significantly larger than the pore size of the template makes proper template reconstruction impossible, yielding only moderately high surface areas).[217] A microporous, templated boron nitride material may indeed exhibit very high storage capacities for hydrogen.

5.2.1 Synthesis of High Surface Area Templated Boron Nitride

Work was done to attempt to use a zeolite template for the growth of microporous boron nitride materials. Common zeolites for the template growth of microporous carbonaceous materials are zeolite Y and β,[209, 211] and zeolite Y (CBV 720, Zeolyst International) was mainly used in this study given its higher surface area and its optimal pore geometry, considering the boron nitride precursor used throughout the study (borazine). The method employed for templated boron nitride material utilized the well understood decomposition of borazine into intermediate polyborazylene (a general term for a polymerized borazine material) and eventually into h-BN (Scheme 5-1).[218, 219]

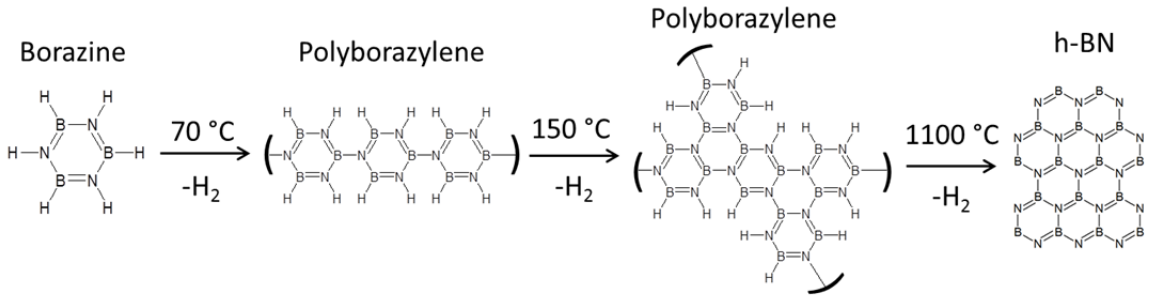

Scheme 5-1. Decomposition of borazine at lower temperatures into polyborazylene materials and eventually at elevated temperatures to h-BN with the loss of hydrogen.

The underlying concept was that if borazine could be decomposed onto the zeolite structure at moderate temperatures and then eventually at elevated temperatures (~1100 °C), then a h-BN-like material could be formed within the pores of the zeolite. The zeolite could then be dissolved, leaving a microporous, templated boron nitride material

with a very high surface area similar to the templated carbonaceous materials with surface areas around 3,000 m^2/g.[209] This process is outlined in Figure 5-1.

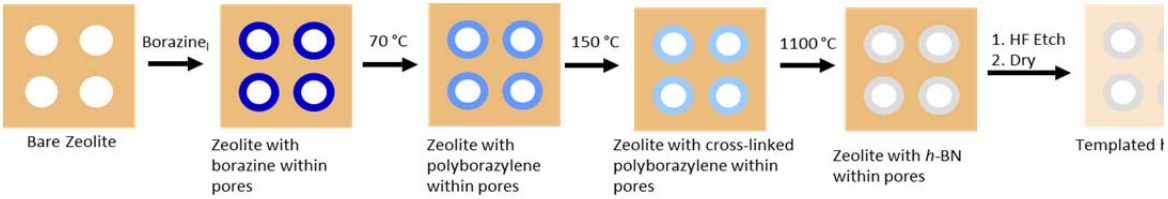

Figure 5-1. Proposed route for synthesizing template high surface area boron nitride material.

To undergo this synthesis, borazine was purchased from Gelest and stored at -4 °C until use. Zeolite Y was degassed to 8 mmHg pressure prior to use (at room temperature for 3 days) to remove the significant quantities of water and other adsorbates within the material and was then transferred to a glove box without exposure to air. Borazine and zeolite Y were then inserted into a Teflon-lined autoclave chambers (Parr, acid digestion bombs), with the zeolite only being exposed to the glove box environment for a short a time as possible. The volume of borazine used for each sample was 200 µL, but the amount of zeolite was varied depending on the sample such that different eventual theoretical monolayers of h-BN would be formed within the zeolite pores (assuming one side of and h-BN sheet with a surface area of 2,600 m^2/g would adhere to the surface of the zeolite) ranging from 0.5 of a monolayer (ML) to 6 monolayers (MLs). This meant that between 500 mg (0.5 ML) and 42 mg (6 ML) of zeolite were used. 6 ML was chosen as the maximum as visible wetting of the zeolite was observed at this amount, indicating complete filling of the zeolite pores, whereas 0.5 ML was chosen as any less would likely not form a structure which would be stable following zeolite removal.

With the two materials inserted, the autoclave was tightened and placed in an oven at 70 °C for 2 days and then at 150 °C for 2 days. After this, the autoclave was brought into a glove-bag with a quartz tube also inserted. After exchanging the volume of the glove-bag three times with N_2, the autoclave was opened and the material was transferred into aluminum boats which were inserted into the quartz tube. The tube was sealed with parafilm and removed from the glove-bag. The quartz tube was then transferred to a CVD setup (Figure 4-1), quickly attached after removing the parafilm, immediately evacuated with a rough pump, and then back-filled with Ar to atmospheric pressure. Under flowing Ar (20 sccm, 99.9999% purity, equipped with a moisture trap and oxygen), the furnace was heated to 1100 °C over 12 hours, kept at 1100 °C for 6 hours, and then cooled to room temperature.

The boat with the material was then emptied into a Teflon centrifuge tube (VWR, Nalgene Oak Ridge Centrifuge Tubes, Teflon FEP) and filled with 5% HF solution (20 mL) for etching of the zeolite (care should always be taken when working with HF solutions and ensuring that calcium gluconate gel is close at hand should be done before use). This was left overnight and then centrifuged (3,000 RPM, 30 minutes) to sediment the remaining material. The supernatant was very carefully pipetted off (with a polymer pipette tip, not a glass one) and put into an HF waste container (polypropylene or polyethylene). The tube was then filled with DI water (20 mL), centrifuged as before, and the supernatant removed and discarded into an HF waste container. This process was repeated three more times with the supernatant then being discarded to the sink under

running water. Finally, the tube was filled with isopropanol, centrifuged as before, and the supernatant was removed. This material was placed onto filter paper and placed in a vacuum oven at 50 °C for 30 minutes. The material was placed in a tared porisometer tube, the weight of the material was determined, and then the tube was placed on the degas side of the porisometer. The tube with material was heated at 100 °C under vacuum for 24 hours before backfilling with N_2 and transferring to the analysis side of the porisometer.

Nitrogen was then used as the analysis gas to determine the BET surface area of the material. BET surface area measurements are more accurate than Langmuir surface area measurements as the equations for determining the surface area using the Langmuir method assume only one monolayer can form on the solid surfaces whereas with the BET surface area, the equations accommodate for liquid layers to form on top of the first adsorbed monolayer. This is especially important for microporous materials where liquefaction of the pores often occurs.

5.2.2 Analysis of High Surface Area Templated Boron Nitride and Synthesis Concerns

One of the main difficulties with the synthesis of high surface area template boron nitride was the yield of material, which was very low. Although 200 μL of borazine (160 mg) was used, the expected amount of 148 mg of resulting material was never realized. This is likely due to a few reasons. Oxidation of the material always existed, as evidenced by EDS measurements (Figure 5-2). With this spectrum, it is seen than all zeolite material has been removed (absence of peaks at the Al and Si Kα peaks) and relatively similar amounts of boron and nitrogen are present. However, a significant amount of oxygen exists in the material as well. Before complete conversion to an h-BN-like material, the intermediate borazine based material is very susceptible to oxidation both by reaction with water and with oxygen. Any exposure during the transfer to the CVD system or mishandling during the preparation could cause oxidation during these times. Furthermore, the long times at elevated temperatures for the anneal increases the likelihood of oxidation during the anneal step. Although precautions were taken to ensure proper purity of the Ar flowing into the CVD system, any leaks in the CVD system which allowed for oxygen in the hot-zone would cause oxidation of the material at these elevated temperatures. Although formation of boron oxide if oxidation occurs would cause a decreased yield (as observed), oxidiation of this material is not strictly detrimental as some theory proposes that oxidative functionalities within a h-BN type material could give ideal hydrogen binding for storage purposes.[220]

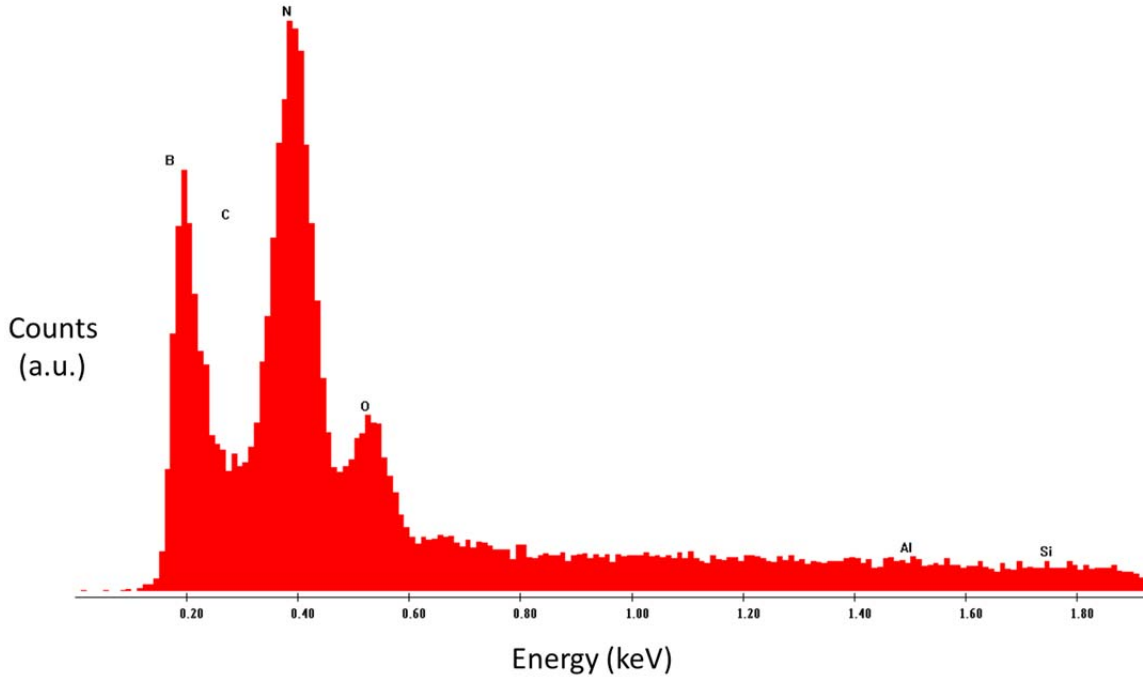

Figure 5-2. EDS spectrum of zeolite templated boron nitride material. The Kα peaks for the corresponding elements are labeled.

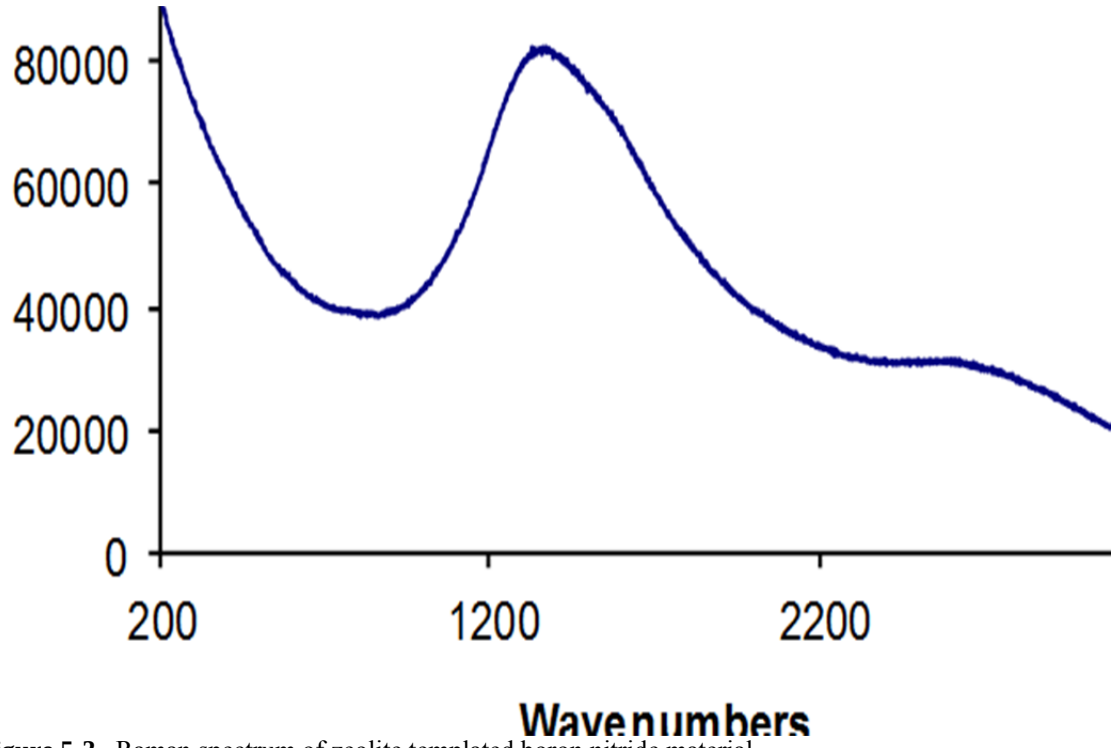

Figure 5-3. Raman spectrum of zeolite templated boron nitride material.

Another loss of yield could occur if the material has not been properly annealed to an h-BN-like state. This material would then still be reactive with the aqueous solutions used for etching and rinsing. Although the annealing process does seem to bring the material to more highly annealed state, the Raman does not well match that of perfect h-BN (Figure 5-3), which would have a single peak at 1367 wavenumbers. However, this is not strictly expected to be the case given the geometric constraints of the material annealing within a small pore. This Raman data does very closely resemble a polyborazylene-type material which has been annealed at 1200 °C as it is converted towards h-BN.[219] Therefore, complete conversion to a h-BN-like material may not have been achieved and the reactivity of the incompletely annealed material to the processing solution could have caused the decreased yield.

5.2.3 Surface Area Measurements and Assessment

High surface area template boron nitride materials were synthesized in quantities sufficient (~5 mg) for BET surface area measurement (Table 5-1). However, significant questions still remain about why the yields are so poor (~3%), and spectroscopic analysis indicates that the material has significant differences from an ideal material which would be completely converted to an h-BN-like state with no oxidation.

Sample (ML)	BET Surface Area (m^2/g)
0.5	310
1	169
2	291
4	185
6	217

Table 5-1. Samples referred to in the text in terms of the theoretical monolayers (ML) of h-BN which would form on the zeolite surface with the accompanying BET surface areas measured.

Significant work would still need to be done to determine how to optimize the synthesis to yield a promising material, especially with determining if the material has been properly annealed and determining where the oxidation occurs during the synthesis. However, if achieved, this approach is very promising in terms of creating a material ideal for hydrogen storage.

Further ideas of how to continue to optimize this material for hydrogen storage include cationic exchange of the zeolite before synthesis with platinum, similar to a study done with a templated carbon material,[221] which could allow for increased storage potential owing to the spill-over mechanism of hydrogen adsorption resulting from the remaining platinum[69] following zeolite etching. The oxidation of this material was briefly discussed, and mild oxidation of templated boron nitride could potentially result in a material with a binding energy for hydrogen very close to the ideal 15-25 kJ/mol.[220] Further approaches could be taken to enhance the surface area including the co-

decomposition of carbonaceous materials with the boron nitride precursor material. After annealing and etching of the template, the carbon could be removed from the structure by simple heating in an oxidative atmosphere resulting in a higher surface area material. Also, the research on BCN materials for hydrogen storage is very limited,[222] and creating varied ratios of BN to C within this type of material could yield promising results.

References

1. Bolotin, K. I.; Sikes, K. J.; Jiang, Z.; Klima, M.; Fudenberg, G.; Hone, J.; Kim, P.; Stormer, H. L., Ultrahigh electron mobility in suspended graphene. *Solid State Communications* **2008,** *146*,9-10, 351-355.
2. Novoselov, K. S.; Geim, A. K.; Morozov, S. V.; Jiang, D.; Zhang, Y.; Dubonos, S. V.; Grigorieva, I. V.; Firsov, A. A., Electric Field Effect in Atomically Thin Carbon Films. *Science* **2004,** *306*,5696, 666-669.
3. Novoselov, K. S.; Geim, A. K.; Morozov, S. V.; Jiang, D.; Katsnelson, M. I.; Grigorieva, I. V.; Dubonos, S. V.; Firsov, A. A., Two-dimensional gas of massless Dirac fermions in graphene. *Nature* **2005,** *438*,7065, 197-200.
4. Balandin, A. A.; Ghosh, S.; Bao, W.; Calizo, I.; Teweldebrhan, D.; Miao, F.; Lau, C. N., Superior Thermal Conductivity of Single-Layer Graphene. *Nano Letters* **2008,** *8*,3, 902-907.
5. Lee, C.; Wei, X.; Kysar, J. W.; Hone, J., Measurement of the Elastic Properties and Intrinsic Strength of Monolayer Graphene. *Science* **2008,** *321*,5887, 385-388.
6. Huang, X.; Yin, Z.; Wu, S.; Qi, X.; He, Q.; Zhang, Q.; Yan, Q.; Boey, F.; Zhang, H., Graphene-Based Materials: Synthesis, Characterization, Properties, and Applications. *Small* **2011,** *7*,14, 1876-1902.
7. Hernandez, Y.; Nicolosi, V.; Lotya, M.; Blighe, F. M.; Sun, Z.; De, S.; McGovern, I. T.; Holland, B.; Byrne, M.; Gun'Ko, Y. K.; Boland, J. J.; Niraj, P.; Duesberg, G.; Krishnamurthy, S.; Goodhue, R.; Hutchison, J.; Scardaci, V.; Ferrari, A. C.; Coleman, J. N., High-yield production of graphene by liquid-phase exfoliation of graphite. *Nat Nano* **2008,** *3*,9, 563-568.
8. Oyer, A. J.; Carrillo, J.-M. Y.; Hire, C. C.; Schniepp, H. C.; Asandei, A. D.; Dobrynin, A. V.; Adamson, D. H., Stabilization of Graphene Sheets by a Structured Benzene/Hexafluorobenzene Mixed Solvent. *Journal of the American Chemical Society* **2012,** *134*,11, 5018-5021.
9. Kim, K. S.; Zhao, Y.; Jang, H.; Lee, S. Y.; Kim, J. M.; Kim, K. S.; Ahn, J.-H.; Kim, P.; Choi, J.-Y.; Hong, B. H., Large-scale pattern growth of graphene films for stretchable transparent electrodes. *Nature* **2009,** *457*,7230, 706-710.
10. Li, X.; Cai, W.; An, J.; Kim, S.; Nah, J.; Yang, D.; Piner, R.; Velamakanni, A.; Jung, I.; Tutuc, E.; Banerjee, S. K.; Colombo, L.; Ruoff, R. S., Large-Area Synthesis of High-Quality and Uniform Graphene Films on Copper Foils. *Science* **2009,** *324*,5932, 1312-1314.
11. Bae, S.; Kim, H.; Lee, Y.; Xu, X.; Park, J.-S.; Zheng, Y.; Balakrishnan, J.; Lei, T.; Ri Kim, H.; Song, Y. I.; Kim, Y.-J.; Kim, K. S.; Ozyilmaz, B.; Ahn, J.-H.; Hong, B. H.; Iijima, S., Roll-to-roll production of 30-inch graphene films for transparent electrodes. *Nat Nano* **2010,** *5*,8, 574-578.
12. Gannett, W.; Regan, W.; Watanabe, K.; Taniguchi, T.; Crommie, M. F.; Zettl, A., Boron nitride substrates for high mobility chemical vapor deposited graphene. *Applied Physics Letters* **2011,** *98*,24, 242105.
13. Zhu, Y.; Murali, S.; Cai, W.; Li, X.; Suk, J. W.; Potts, J. R.; Ruoff, R. S., Graphene and Graphene Oxide: Synthesis, Properties, and Applications. *Advanced Materials* **2010,** *22*,35, 3906-3924.

14. Paci, J. T.; Belytschko, T.; Schatz, G. C., Computational Studies of the Structure, Behavior upon Heating, and Mechanical Properties of Graphite Oxide. *The Journal of Physical Chemistry C* **2007,** *111*,49, 18099-18111.
15. Szabo, T.; Berkesi, O.; Forgo, P.; Josepovits, K.; Sanakis, Y.; Petridis, D.; Dekany, I., Evolution of Surface Functional Groups in a Series of Progressively Oxidized Graphite Oxides. *Chemistry of Materials* **2006,** *18*,11, 2740-2749.
16. Hofmann, U.; Holst, R., The acidic nature and the methylation of graphitoxide. *Berichte Der Deutschen Chemischen Gesellschaft* **1939,** *72*, 754-771.
17. Scholz, W.; Boehm, H. P., Graphite Oxide: 6. Structure of Graphite Oxide. *Z. Anorg. Allg. Chem.* **1969,** *369*,3-6, 327.
18. Lerf, A.; He, H.; Forster, M.; Klinowski, J., Structure of Graphite Oxide Revisited. *The Journal of Physical Chemistry B* **1998,** *102*,23, 4477-4482.
19. Dreyer, D. R.; Park, S.; Bielawski, C. W.; Ruoff, R. S., The chemistry of graphene oxide. *Chemical Society Reviews* **2010,** *39*,1, 228-240.
20. Paredes, J. I.; Villar-Rodil, S.; Martinez-Alonso, A.; Tascon, J. M. D., Graphene Oxide Dispersions in Organic Solvents. *Langmuir* **2008,** *24*,19, 10560-10564.
21. López, V.; Sundaram, R. S.; Gómez-Navarro, C.; Olea, D.; Burghard, M.; Gómez-Herrero, J.; Zamora, F.; Kern, K., Chemical Vapor Deposition Repair of Graphene Oxide: A Route to Highly-Conductive Graphene Monolayers. *Advanced Materials* **2009,** *21*,46, 4683-4686.
22. Erni, R.; Rossell, M. D.; Nguyen, M.-T.; Blankenburg, S.; Passerone, D.; Hartel, P.; Alem, N.; Erickson, K.; Gannett, W.; Zettl, A., Stability and dynamics of small molecules trapped on graphene. *Physical Review B* **2010,** *82*,16, 165443.
23. Erickson, K.; Erni, R.; Lee, Z.; Alem, N.; Gannett, W.; Zettl, A., Determination of the Local Chemical Structure of Graphene Oxide and Reduced Graphene Oxide. *Advanced Materials* **2010,** *22*,40, 4467-4472.
24. Hummers, W. S.; Offeman, R. E., Preparation of Graphitic Oxide. *Journal of the American Chemical Society* **1958,** *80*,6, 1339-1339.
25. Wilson, N. R.; Pandey, P. A.; Beanland, R.; Young, R. J.; Kinloch, I. A.; Gong, L.; Liu, Z.; Suenaga, K.; Rourke, J. P.; York, S. J.; Sloan, J., Graphene Oxide: Structural Analysis and Application as a Highly Transparent Support for Electron Microscopy. *ACS Nano* **2009,** *3*,9, 2547-2556.
26. Meyer, J. C.; Geim, A. K.; Katsnelson, M. I.; Novoselov, K. S.; Obergfell, D.; Roth, S.; Girit, C.; Zettl, A., On the roughness of single- and bi-layer graphene membranes. *Solid State Communications* **2007,** *143*,1-2, 101-109.
27. Meyer, J. C.; Kisielowski, C.; Erni, R.; Rossell, M. D.; Crommie, M. F.; Zettl, A., Direct Imaging of Lattice Atoms and Topological Defects in Graphene Membranes. *Nano Letters* **2008,** *8*,11, 3582-3586.
28. Rossell, M. D.; Erni, R.; Asta, M.; Radmilovic, V.; Dahmen, U., Atomic-resolution imaging of lithium in Al3Li precipitates. *Physical Review B* **2009,** *80*,2, 024110.
29. Meyer, J. C.; Girit, C. O.; Crommie, M. F.; Zettl, A., Imaging and dynamics of light atoms and molecules on graphene. *Nature* **2008,** *454*,7202, 319-322.
30. Pantelic, R. S.; Meyer, J. C.; Kaiser, U.; Baumeister, W.; Plitzko, J. M., Graphene oxide: A substrate for optimizing preparations of frozen-hydrated samples. *Journal of Structural Biology* **2010,** *170*,1, 152-156.

31. Gomez-Navarro, C.; Meyer, J. C.; Sundaram, R. S.; Chuvilin, A.; Kurasch, S.; Burghard, M.; Kern, K.; Kaiser, U., Atomic Structure of Reduced Graphene Oxide. *Nano Letters* **2010,** *10*,4, 1144-1148.
32. Jung, I.; Dikin, D.; Park, S.; Cai, W.; Mielke, S. L.; Ruoff, R. S., Effect of Water Vapor on Electrical Properties of Individual Reduced Graphene Oxide Sheets. *Journal of Physical Chemistry C* **2008,** *112*,51, 20264-20268.
33. Becerril, H. A.; Mao, J.; Liu, Z.; Stoltenberg, R. M.; Bao, Z.; Chen, Y., Evaluation of solution-processed reduced graphene oxide films as transparent conductors. *Acs Nano* **2008,** *2*,3, 463-470.
34. Su, Q.; Pang, S.; Alijani, V.; Li, C.; Feng, X.; Müllen, K., Composites of Graphene with Large Aromatic Molecules. *Advanced Materials* **2009,** *21*,31, 3191-3195.
35. Liang, Y.; Frisch, J.; Zhi, L.; Norouzi-Arasi, H.; Feng, X.; Jergen, P. R.; Koch, N.; Mullen, K., Transparent, highly conductive graphene electrodes from acetylene-assisted thermolysis of graphite oxide sheets and nanographene molecules. *Nanotechnology* **2009,** *20*,43, 434007.
36. Li, X.; Zhang, G.; Bai, X.; Sun, X.; Wang, X.; Wang, E.; Dai, H., Highly conducting graphene sheets and Langmuir-Blodgett films. *Nat Nano* **2008,** *3*,9, 538-542.
37. Donald, W. B.; Shenderova, O. A.; Harrison, J. A.; Stuart, S. J.; Ni, B.; Sinnott, S. B., A second-generation reactive empirical bond order (REBO) potential energy expression for hydrocarbons. *Journal of Physics: Condensed Matter* **2002,** *14*,4, 783.
38. Lahaye, R. J. W. E.; Jeong, H. K.; Park, C. Y.; Lee, Y. H., Density functional theory study of graphite oxide for different oxidation levels. *Physical Review B* **2009,** *79*,12, 125435.
39. Egerton, R. F.; Wang, F.; Crozier, P. A., Beam-induced damage to thin specimens in an intense electron probe. *Microscopy and Microanalysis* **2006,** *12*,1, 65-71.
40. Li, J.-L.; Kudin, K. N.; McAllister, M. J.; Prud'homme, R. K.; Aksay, I. A.; Car, R., Oxygen-Driven Unzipping of Graphitic Materials. *Physical Review Letters* **2006,** *96*,17, 176101.
41. Girit, C. O.; Meyer, J. C.; Erni, R.; Rossell, M. D.; Kisielowski, C.; Yang, L.; Park, C. H.; Crommie, M. F.; Cohen, M. L.; Louie, S. G.; Zettl, A., Graphene at the Edge: Stability and Dynamics. *Science* **2009,** *323*,5922, 1705-1708.
42. Jeong, H.-K.; Lee, Y. P.; Lahaye, R. J. W. E.; Park, M.-H.; An, K. H.; Kim, I. J.; Yang, C.-W.; Park, C. Y.; Ruoff, R. S.; Lee, Y. H., Evidence of Graphitic AB Stacking Order of Graphite Oxides. *Journal of the American Chemical Society* **2008,** *130*,4, 1362-1366.
43. Backreedy, R.; Jones, J. M.; Pourkashanian, M.; Williams, A., A study of the reaction of oxygen with graphite: Model chemistry. *Faraday Discussions* **2002,** *119*, 385-394.
44. Kim, M. C.; Hwang, G. S.; Ruoff, R. S., Epoxide reduction with hydrazine on graphene: A first principles study. *The Journal of Chemical Physics* **2009,** *131*,6, 064704.
45. Cai, W.; Piner, R. D.; Stadermann, F. J.; Park, S.; Shaibat, M. A.; Ishii, Y.; Yang, D.; Velamakanni, A.; An, S. J.; Stoller, M.; An, J.; Chen, D.; Ruoff, R. S., Synthesis and Solid-State NMR Structural Characterization of 13C-Labeled Graphite Oxide 10.1126/science.1162369. *Science* **2008,** *321*,5897, 1815-1817.
46. Mermoux, M.; Chabre, Y.; Rousseau, A., Ftir and C-13 Nmr-Study of Graphite Oxide. *Carbon* **1991,** *29*,3, 469-474.

47. Yin, Z.; Wu, S.; Zhou, X.; Huang, X.; Zhang, Q.; Boey, F.; Zhang, H., Electrochemical Deposition of ZnO Nanorods on Transparent Reduced Graphene Oxide Electrodes for Hybrid Solar Cells. *Small* **2010,** *6*,2, 307-312.
48. Han, T. H.; Huang, Y.-K.; Tan, A. T. L.; Dravid, V. P.; Huang, J., Steam Etched Porous Graphene Oxide Network for Chemical Sensing. *Journal of the American Chemical Society* **2011,** *133*,39, 15264-15267.
49. Lin, Z.; Liu, Y.; Yao, Y.; Hildreth, O. J.; Li, Z.; Moon, K.; Wong, C.-p., Superior Capacitance of Functionalized Graphene. *The Journal of Physical Chemistry C* **2011,** *115*,14, 7120-7125.
50. Xiao, J.; Mei, D.; Li, X.; Xu, W.; Wang, D.; Graff, G. L.; Bennett, W. D.; Nie, Z.; Saraf, L. V.; Aksay, I. A.; Liu, J.; Zhang, J.-G., Hierarchically Porous Graphene as a Lithium-Air Battery Electrode. *Nano Letters* **2011,** *11*,11, 5071-5078.
51. Gudarzi, M. M.; Sharif, F., Molecular level dispersion of graphene in polymer matrices using colloidal polymer and graphene. *Journal of Colloid and Interface Science* **2012,** *366*,1, 44-50.
52. Byrne, M. T.; Gun'ko, Y. K., Recent Advances in Research on Carbon Nanotube–Polymer Composites. *Advanced Materials* **2010,** *22*,15, 1672-1688.
53. Zhang, M.; Zhang, T.; Cui, T., Wettability Conversion from Superoleophobic to Superhydrophilic on Titania/Single-Walled Carbon Nanotube Composite Coatings. *Langmuir* **2011,** *27*,15, 9295-9301.
54. Chang, C.-M.; Liu, Y.-L., Electrical Conductivity Enhancement of Polymer/Multiwalled Carbon Nanotube (MWCNT) Composites by Thermally-Induced Defunctionalization of MWCNTs. *ACS Applied Materials & Interfaces* **2011,** *3*,7, 2204-2208.
55. Han, Z.; Fina, A., Thermal conductivity of carbon nanotubes and their polymer nanocomposites: A review. *Progress in Polymer Science* **2010,** *36*,7, 914-944.
56. Fornasiero, F.; Park, H. G.; Holt, J. K.; Stadermann, M.; Grigoropoulos, C. P.; Noy, A.; Bakajin, O., Ion exclusion by sub-2-nm carbon nanotube pores. *Proceedings of the National Academy of Sciences* **2008,** *105*,45, 17250-17255.
57. Deng, C. F.; Wang, D. Z.; Zhang, X. X.; Li, A. B., Processing and properties of carbon nanotubes reinforced aluminum composites. *Materials Science and Engineering: A* **2007,** *444*,1-2, 138-145.
58. Ruoff, R. S.; Qian, D.; Liu, W. K., Mechanical properties of carbon nanotubes: theoretical predictions and experimental measurements. *Comptes Rendus Physique* **2003,** *4*,9, 993-1008.
59. Pennings, A. J.; Hooft, R. J.; Postema, A. R.; Hoogsteen, W.; Brinke, G., High-speed gel-spinning of ultra-high molecular weight polyethylene. *Polymer Bulletin* **1986,** *16*,2, 167-174.
60. Wei, X.; Wang, M.-S.; Bando, Y.; Golberg, D., Tensile Tests on Individual Multi-Walled Boron Nitride Nanotubes. *Advanced Materials* **2010,** *22*,43, 4895-4899.
61. http://en.wikipedia.org/wiki/Young's_modulus.
62. Demczyk, B. G.; Wang, Y. M.; Cumings, J.; Hetman, M.; Han, W.; Zettl, A.; Ritchie, R. O., Direct mechanical measurement of the tensile strength and elastic modulus of multiwalled carbon nanotubes. *Materials Science and Engineering: A* **2002,** *334*,1–2, 173-178.

63. Coleman, J. N.; Khan, U.; Blau, W. J.; Gun'ko, Y. K., Small but strong: A review of the mechanical properties of carbon nanotube-polymer composites. *Carbon* **2006,** *44*,9, 1624-1652.
64. Hiura, H.; Ebbesen, T. W.; Tanigaki, K., Opening and purification of carbon nanotubes in high yields. *Advanced Materials* **1995,** *7*,3, 275-276.
65. Sainsbury, T.; Erickson, K.; Okawa, D.; Zonte, C. S.; FreÌ chet, J. M. J.; Zettl, A., Kevlar Functionalized Carbon Nanotubes for Next-Generation Composites. *Chemistry of Materials* **2010,** *22*,6, 2164-2171.
66. Badia, A.; Singh, S.; Demers, L.; Cuccia, L.; Brown, G. R.; Lennox, R. B., Self-Assembled Monolayers on Gold Nanoparticles. *Chemistry – A European Journal* **1996,** *2*,3, 359-363.
67. Prasad, K.; Grubb, D. T., Deformation behavior of Kevlar fibers studied by Raman spectroscopy. *Journal of Applied Polymer Science* **1990,** *41*,9-10, 2189-2198.
68. Karousis, N.; Tsotsou, G.-E.; Evangelista, F.; Rudolf, P.; Ragoussis, N.; Tagmatarchis, N., Carbon Nanotubes Decorated with Palladium Nanoparticles: Synthesis, Characterization, and Catalytic Activity. *The Journal of Physical Chemistry C* **2008,** *112*,35, 13463-13469.
69. Bhowmick, R.; Rajasekaran, S.; Friebel, D.; Beasley, C.; Jiao, L.; Ogasawara, H.; Dai, H.; Clemens, B.; Nilsson, A., Hydrogen Spillover in Pt-Single-Walled Carbon Nanotube Composites: Formation of Stable C-H Bonds. *Journal of the American Chemical Society* **2011,** *133*,14, 5580-5586.
70. Jadzinsky, P. D.; Calero, G.; Ackerson, C. J.; Bushnell, D. A.; Kornberg, R. D., Structure of a Thiol Monolayer-Protected Gold Nanoparticle at 1.1 A Resolution. *Science* **2007,** *318*,5849, 430-433.
71. Bönnemann, H.; Richards, Ryan M., Nanoscopic Metal Particles − Synthetic Methods and Potential Applications. *European Journal of Inorganic Chemistry* **2001,** *2001*,10, 2455-2480.
72. Flanagan, K. A.; Sullivan, J. A.; Mueller-Bunz, H., Preparation and Characterization of 4-Dimethylaminopyridine-Stabilized Palladium Nanoparticles. *Langmuir* **2007,** *23*,25, 12508-12520.
73. Sainsbury, T.; Ikuno, T.; Okawa, D.; Pacile, D.; Frechet, J. M. J.; Zettl, A., Self-Assembly of Gold Nanoparticles at the Surface of Amine- and Thiol-Functionalized Boron Nitride Nanotubes. *The Journal of Physical Chemistry C* **2007,** *111*,35, 12992-12999.
74. Zettl, A.; Ikuno, T.; Sainsbury, T.; Okawa, D.; Frechet, J. M. J., Amine-functionalized boron nitride nanotubes. *Solid State Communications* **2007,** *142*,11, 643–646.
75. Sainsbury, T.; Ikuno, T.; Okawa, D.; Pacile, D.; Frechet, J. M. J.; Zettl, A., Self-assembly of gold nanoparticles at the surface of amine- and thiol-functionalized boron nitride nanotubes. *Journal of Physical Chemistry C* **2007,** *111*,35, 12992-12999.
76. Zhi, C. Y.; Bando, Y.; Terao, T.; Tang, C. C.; Kuwahara, H.; Golberg, D., Chemically Activated Boron Nitride Nanotubes. *Chemistry – An Asian Journal* **2009,** *4*,10, 1536-1540.
77. Kang, J. H.; Park, C.; Scholl, J. A.; Brazin, A. H.; Holloway, N. M.; High, J. W.; Lowther, S. E.; Harrison, J. S., Piezoresistive characteristics of single wall carbon

nanotube/polyimide nanocomposites. *Journal of Polymer Science Part B: Polymer Physics* **2009,** *47*,16, 1635-1636.
78. Nakhmanson, S. M.; Calzolari, A.; Meunier, V.; Bernholc, J.; Nardelli, M. B., Spontaneous polarization and piezoelectricity in boron nitride nanotubes. *Physical Review B* **2003,** *67*,23, 5.
79. Wang, Y.; Shi, Z.; Yin, J., Boron nitride nanosheets: large-scale exfoliation in methanesulfonic acid and their composites with polybenzimidazole. *Journal of Materials Chemistry* **2011,** *21*,30, 11371-11377.
80. Yu, J.; Chen, Y.; Elliman, R. G.; Petravic, M., Isotopically Enriched 10BN Nanotubes. *Advanced Materials* **2006,** *18*,16, 2157-2160.
81. Chopra, N. G.; Zettl, A., Measurement of the elastic modulus of a multi-wall boron nitride nanotube. *Solid State Communications* **1998,** *105*,5, 297-300.
82. Kang, J. H.; Park, C.; Scholl, J. A.; Brazin, A. H.; Holloway, N. M.; High, J. W.; Lowther, S. E.; Harrison, J. S., Piezoresistive characteristics of single wall carbon nanotube/polyimide nanocomposites. *Journal of Polymer Science Part B: Polymer Physics* **2009,** *47*,10, 994-1003.
83. Iijima, S., Helical microtubules of graphitic carbon. *Nature* **1991,** *354*,6348, 56-58.
84. Geim, A. K.; Novoselov, K. S., The rise of graphene. *Nature Materials* **2007,** *6*,3, 183-191.
85. Jiao, L.; Wang, X.; Diankov, G.; Wang, H.; Dai, H., Facile synthesis of high-quality graphene nanoribbons. *Nat Nano* **2010,** *5*,5, 321-325.
86. Jiao, L.; Zhang, L.; Wang, X.; Diankov, G.; Dai, H., Narrow graphene nanoribbons from carbon nanotubes. *Nature* **2009,** *458*,7240, 877-880.
87. Kosynkin, D. V.; Higginbotham, A. L.; Sinitskii, A.; Lomeda, J. R.; Dimiev, A.; Price, B. K.; Tour, J. M., Longitudinal unzipping of carbon nanotubes to form graphene nanoribbons. *Nature* **2009,** *458*,7240, 872-876.
88. Kosynkin, D. V.; Lu, W.; Sinitskii, A.; Pera, G.; Sun, Z.; Tour, J. M., Highly Conductive Graphene Nanoribbons by Longitudinal Splitting of Carbon Nanotubes Using Potassium Vapor. *ACS Nano* **2011,** *5*,2, 968-974.
89. Chopra, N. G.; Luyken, R. J.; Cherrey, K.; Crespi, V. H.; Cohen, M. L.; Louie, S. G.; Zettl, A., BORON-NITRIDE NANOTUBES. *Science* **1995,** *269*,5226, 966-967.
90. Nagashima, A.; Tejima, N.; Gamou, Y.; Kawai, T.; Oshima, C., ELECTRONIC DISPERSION-RELATIONS OF MONOLAYER HEXAGONAL BORON-NITRIDE FORMED ON THE NI(111) SURFACE. *Physical Review B* **1995,** *51*,7, 4606-4613.
91. Azadi, S.; Moradian, R., First principle study of unzipped boron nitride nanotubes. *Phys. Lett. A* **2010,** *374*,4, 605-609.
92. Barone, V.; Peralta, J. E., Magnetic boron nitride nanoribbons with tunable electronic properties. *Nano Letters* **2008,** *8*,8, 2210-2214.
93. Chen, W.; Li, Y.; Yu, G.; Li, C.-Z.; Zhang, S. B.; Zhou, Z.; Chen, Z., Hydrogenation: A Simple Approach To Realize Semiconductor Half-Metal Metal Transition in Boron Nitride Nanoribbons. *Journal of the American Chemical Society* **2010,** *132*,5, 1699-1705.
94. Ding, Y.; Wang, Y. L.; Ni, J., The stabilities of boron nitride nanoribbons with different hydrogen-terminated edges. *Applied Physics Letters* **2009,** *94*,23, 3.

95. Feng, C.; Mi, Z.; Jian-xin, Z., Strain effect on transport properties of hexagonal boron nitride nanoribbons. *Chin. Phys. B* **2011,** *19*,8, 086105.
96. Lai, L.; Lu, J.; Wang, L.; Luo, G.; Zhou, J.; Qin, R.; Gao, Z.; Mei, W. N., Magnetic Properties of Fully Bare and Half-Bare Boron Nitride Nanoribbons. *The Journal of Physical Chemistry C* **2009,** *113*,6, 2273-2276.
97. Park, C.-H.; Louie, S. G., Energy gaps and stark effect in boron nitride nanoribbons. *Nano Letters* **2008,** *8*,8, 2200-3.
98. Topsakal, M.; Aktark, E.; Ciraci, S., First-principles study of two- and one-dimensional honeycomb structures of boron nitride. *Physical Review B* **2009,** *79*,11, 1-11.
99. Zeng, H.; Zhi, C.; Zhang, Z.; Wei, X.; Wang, X.; Guo, W.; Bando, Y.; Golberg, D., "White Graphenes": Boron Nitride Nanoribbons via Boron Nitride Nanotube Unwrapping. *Nano Letters* **2010,** *10*,12, 5049–5055.
100. Zheng, F.; Zhou, G.; Liu, Z.; Wu, J.; Duan, W.; Gu, B.-L.; Zhang, S., Half metallicity along the edge of zigzag boron nitride nanoribbons. *Physical Review B* **2008,** *78*,20, 1-5.
101. Samarakoon, D. K.; Wang, X. Q., Intrinsic half-metallicity in hydrogenated boron-nitride nanoribbons. *Applied Physics Letters* **2012,** *100*,10, 4.
102. Qi, J. S.; Qian, X. F.; Qi, L.; Feng, J.; Shi, D. N.; Li, J., Strain-Engineering of Band Gaps in Piezoelectric Boron Nitride Nanoribbons. *Nano Letters* **2012,** *12*,3, 1224-1228.
103. Chen, Y. H.; Zhang, C. M.; Wu, J. B.; Lin, Q., Effect of O/N Substitutive Doping on the Band Structure and Transport Properties of the zigzag Boron Nitride Narrow-Nanoribbons. *Acta Phys.-Chim. Sin.* **2012,** *28*,3, 567-572.
104. Lu, D. B.; Song, Y. L.; Tian, Y.; Xu, H. R.; Lu, Z. W., First-principles study of the F-terminated Boron Nitride nanoribbons. *Comput. Theor. Chem.* **2012,** *979*, 49-53.
105. Lopez-Bezanilla, A.; Huang, J. S.; Terrones, H.; Sumpter, B. G., Boron Nitride Nanoribbons Become Metallic. *Nano Letters* **2011,** *11*,8, 3267-3273.
106. Izmaylov, A. F.; Frisch, M. J., Spin decoherence in carbon and boron-nitride nanoribbons. *Abstr. Pap. Am. Chem. Soc.* **2009,** *237*, 1.
107. Mukherjee, R.; Bhowmick, S., Edge Stabilities of Hexagonal Boron Nitride Nanoribbons: A First-Principles Study. *Journal of Chemical Theory and Computation* **2011,** *7*,3, 720-724.
108. Chen, F.; Chen, Y. P.; Zhang, M.; Zhong, J. X., Strain effect on transport properties of hexagonal boron-nitride nanoribbons. *Chin. Phys. B* **2010,** *19*,8, 6.
109. Jalili, S.; Vaziri, R., Curvature effect on the electronic properties of BN nanoribbons. *Molecular Physics* **2010,** *108*,24, 3365-3371.
110. Chen, W.; Li, Y.; Yu, G.; Zhou, Z.; Chen, Z., Electronic Structure and Reactivity of Boron Nitride Nanoribbons with Stone-Wales Defects. *Journal of Chemical Theory and Computation* **2009,** *5*,11, 3088-3095.
111. Yi, D.; Yanli, W.; Jun, N., The stabilities of boron nitride nanoribbons with different hydrogen-terminated edges. *Applied Physics Letters* **2009,** *94*,23, 233107.
112. Tang, Q.; Zhou, Z.; Chen, Z. F., Molecular Charge Transfer: A Simple and Effective Route To Engineer the Band Structures of BN Nanosheets and Nanoribbons. *Journal of Physical Chemistry C* **2011,** *115*,38, 18531-18537.

113. Kan, E. J.; Wu, F.; Xiang, H. J.; Yang, J. L.; Whangbo, M. H., Half-Metallic Dirac Point in B-Edge Hydrogenated BN Nanoribbons. *Journal of Physical Chemistry C* **2011,** *115*,35, 17252-17254.
114. Wang, S. D.; Chen, Q.; Wang, J. L., Optical properties of boron nitride nanoribbons: Excitonic effects. *Applied Physics Letters* **2011,** *99*,6, 3.
115. Liu, Y. Y.; Bhowmick, S.; Yakobson, B. I., BN White Graphene with "Colorful" Edges: The Energies and Morphology. *Nano Letters* **2011,** *11*,8, 3113-3116.
116. Wang, Y. L.; Ding, Y.; Ni, J., Stereo Boron Nitride Nanoribbons with Junction-Dependent Electronic Structures from First-Principles. *Journal of Physical Chemistry C* **2012,** *116*,10, 5995-6003.
117. Huang, B.; Lee, H.; Gu, B. L.; Liu, F.; Duan, W. H., Edge stability of boron nitride nanoribbons and its application in designing hybrid BNC structures. *Nano Research* **2012,** *5*,1, 62-72.
118. Modarresi, M.; Roknabadi, M. R.; Shahtahmasbi, N., Transport properties of an armchair boron-nitride nanoribbon embedded between two graphene electrodes. *Physica E* **2011,** *43*,9, 1751-1754.
119. Wei, X. L.; Wang, M. S.; Bando, Y.; Golberg, D., Electron-Beam-Induced Substitutional Carbon Doping of Boron Nitride Nanosheets, Nanoribbons, and Nanotubes. *Acs Nano* **2011,** *5*,4, 2916-2922.
120. Zheng, F. L.; Zhang, Y.; Zhang, J. M.; Xu, K. W., Effect of the dangling bond on the electronic and magnetic properties of BN nanoribbon. *Journal of Physics and Chemistry of Solids* **2011,** *72*,4, 256-262.
121. Lai, L.; Lu, J., Half metallicity in BC2N nanoribbons: stability, electronic structures, and magnetism. *Nanoscale* **2011,** *3*,6, 2583-2588.
122. He, J.; Chen, K. Q.; Fan, Z. Q.; Tang, L. M.; Hu, W. P., Transition from insulator to metal induced by hybridized connection of graphene and boron nitride nanoribbons. *Applied Physics Letters* **2010,** *97*,19, 3.
123. Gyungseon, S.; Jing, G., Bandgap opening in boron nitride confined armchair graphene nanoribbon. *Applied Physics Letters* **2011,** *98*,14, 143107.
124. Noei, M.; Fathipour, M.; Pourfath, M., A Computational Study on the Electronic Properties of Armchair Graphene Nanoribbons Confined by Boron Nitride. *Japanese Journal of Applied Physics* **2012,** *51*,3, 6.
125. Du, A. J.; Smith, S. C.; Lu, G. Q., First-principle studies of electronic structure and C-doping effect in boron nitride nanoribbon. *Chemical Physics Letters* **2007,** *447*,4-6, 181-186.
126. Yu, Z. Z.; Hu, M. L.; Zhang, C. X.; He, C. Y.; Sun, L. Z.; Zhong, J. X., Transport Properties of Hybrid Zigzag Graphene and Boron Nitride Nanoribbons. *Journal of Physical Chemistry C* **2011,** *115*,21, 10836-10841.
127. Jiao, L. Y.; Zhang, L.; Wang, X. R.; Diankov, G.; Dai, H. J., Narrow graphene nanoribbons from carbon nanotubes. *Nature* **2009,** *458*, 877-880.
128. Sinitskii, A.; Dimiev, A.; Kosynkin, D. V.; Tour, J. M., Graphene nanoribbon devices produced by oxidative unzipping of carbon nanotubes. *ACS nano* **2010,** *4*,9, 5405-13.
129. Michael, W. S. a. K. C. J. a. C. P. a. J.-W. K. a. P. T. L. a. R. C. a. J. S. H., Very long single-and few-walled boron nitride nanotubes via the pressurized vapor/condenser method. *Nanotechnology* **2009,** *20*,50, 505604.

130. Zhi, C.; Bando, Y.; Tan, C.; Golberg, D., Effective precursor for high yield synthesis of pure BN nanotubes. *Solid State Communications* **2005,** *135*,1-2, 67-70.
131. Tang, C.; Bando, Y.; Sato, T.; Kurashima, K., A novel precursor for synthesis of pure boron nitride nanotubes. *Chemical Communications* **2002**,12, 1290-1291.
132. Golberg, D.; Bando, Y.; Tang, C.; Zhi, C., Boron Nitride Nanotubes. *Advanced Materials* **2007,** *19*,18, 2413-2432.
133. Celik-Aktas, A.; Zuo, J. M.; Stubbins, J. F.; Tang, C.; Bando, Y., Double-helix structure in multiwall boron nitride nanotubes. *Acta crystallographica. Section A, Foundations of crystallography* **2005,** *61*, 533-41.
134. Alem, N.; Erni, R.; Kisielowski, C.; Rossell, M.; Gannett, W.; Zettl, a., Atomically thin hexagonal boron nitride probed by ultrahigh-resolution transmission electron microscopy. *Physical Review B* **2009,** *80*,15, 1-7.
135. Zhang, J.; Xiao, J.; Meng, X.; Monroe, C.; Huang, Y.; Zuo, J.-M., Free Folding of Suspended Graphene Sheets by Random Mechanical Stimulation. *Physical Review Letters* **2010,** *104*,16, 2-5.
136. Rotkin, S.; Gogotsi, Y., Analysis of non-planar graphitic structures: from arched edge planes of graphite crystals to nanotubes. *Materials Research Innovations* **2002,** *5*,5, 191-200.
137. Jiao, L.; Wang, X.; Diankov, G.; Wang, H.; Dai, H., Facile synthesis of high-quality graphene nanoribbons. *Nature Nanotechnology* **2010,** *5*,5, 321-325.
138. Parra-Vasquez, A. N. G.; Behabtu, N.; Green, M. J.; Pint, C. L.; Young, C. C.; Schmidt, J.; Kesselman, E.; Goyal, A.; Ajayan, P. M.; Cohen, Y.; Talmon, Y.; Hauge, R. H.; Pasquali, M., Spontaneous Dissolution of Ultralong Single- and Multiwalled Carbon Nanotubes. *ACS Nano* **2010,** *4*,7, 3969-3978.
139. Dresselhaus, M. S.; Dresselhaus, G., Intercalation compounds of graphite. *Advances in Physics* **2002,** *51*,1, 1-186.
140. Doll, G. L.; Speck, J. S.; Dresselhaus, G.; Dresselhaus, M. S.; Nakamura, K.; Tanuma, S. I., Intercalation of hexagonal boron nitride with potassium. *Journal of Applied Physics* **1989,** *66*,6, 2554-2554.
141. Shen, C., Intercalation of Hexagonal Boron Nitride by Strong Oxidizers and Evidence for the Metallic Nature of the Products. *Journal of Solid State Chemistry* **1999,** *147*,1, 74-81.
142. Sumiyoshi, a.; Hyodo, H.; Kimura, K., Li-intercalation into hexagonal boron nitride. *Journal of Physics and Chemistry of Solids* **2010,** *71*,4, 569-571.
143. Okada, S.; Otani, M., Stability and electronic structure of potassium-intercalated hexagonal boron nitride from density functional calculations. *Physical Review B* **2010,** *81*,23, 3-6.
144. Ikuno, T.; Sainsbury, T.; Okawa, D.; Frechet, J.; Zettl, A., Amine-functionalized boron nitride nanotubes. *Solid State Communications* **2007,** *142*,11, 643-646.
145. Zhi, C. Y.; Bando, Y.; Terao, T.; Tang, C. C.; Kuwahara, H.; Golberg, D., Chemically activated boron nitride nanotubes. *Chemistry, an Asian Journal* **2009,** *4*,10, 1536-40.
146. Novoselov, K. S.; Jiang, D.; Schedin, F.; Booth, T. J.; Khotkevich, V. V.; Morozov, S. V.; Geim, A. K., Two-dimensional atomic crystals. *Proceedings of the National Academy of Sciences of the United States of America* **2005,** *102*,30, 10451-10453.

147. Shi, Y.; Hamsen, C.; Jia, X.; Kim, K. K.; Reina, A.; Hofmann, M.; Hsu, A. L.; Zhang, K.; Li, H.; Juang, Z.-Y.; Dresselhaus, M. S.; Li, L.-J.; Kong, J., Synthesis of Few-Layer Hexagonal Boron Nitride Thin Film by Chemical Vapor Deposition. *Nano Letters* **2010,** *10*,10, 4134-4139.
148. Britnell, L.; Gorbachev, R. V.; Jalil, R.; Belle, B. D.; Schedin, F.; Katsnelson, M. I.; Eaves, L.; Morozov, S. V.; Mayorov, A. S.; Peres, N. M. R.; Castro Neto, A. H.; Leist, J.; Geim, A. K.; Ponomarenko, L. A.; Novoselov, K. S., Electron Tunneling through Ultrathin Boron Nitride Crystalline Barriers. *Nano Letters* **2012,** *12*,3, 1707-1710.
149. Decker, R. g.; Wang, Y.; Brar, V. W.; Regan, W.; Tsai, H.-Z.; Wu, Q.; Gannett, W.; Zettl, A.; Crommie, M. F., Local Electronic Properties of Graphene on a BN Substrate via Scanning Tunneling Microscopy. *Nano Letters* **2011,** *11*,6, 2291-2295.
150. Zande, A. M. v. d.; Barton, R. A.; Alden, J. S.; Ruiz-Vargas, C. S.; Whitney, W. S.; Pham, P. H. Q.; Park, J.; Parpia, J. M.; Craighead, H. G.; McEuen, P. L., Large-Scale Arrays of Single-Layer Graphene Resonators. *Nano Letters* **2010,** *10*,12, 4869-4873.
151. Yu, Z.; Hu, M. L.; Zhang, C. X.; He, C. Y.; Sun, L. Z.; Zhong, J., Transport Properties of Hybrid Zigzag Graphene and Boron Nitride Nanoribbons. *The Journal of Physical Chemistry C* **2011,** *115*,21, 10836-10841.
152. Ci, L.; Song, L.; Jin, C.; Jariwala, D.; Wu, D.; Li, Y.; Srivastava, A.; Wang, Z. F.; Storr, K.; Balicas, L.; Liu, F.; Ajayan, P. M., Atomic layers of hybridized boron nitride and graphene domains. *Nat Mater* **2010,** *9*,5, 430-435.
153. Carreno, M. N. P.; Bottecchia, J. P.; Pereyra, I., Low temperature plasma enhanced chemical vapour deposition boron nitride. *Thin Solid Films* **1997,** *308*, 219-222.
154. Corso, M.; Auwarter, W.; Muntwiler, M.; Tamai, A.; Greber, T.; Osterwalder, J., Boron nitride nanomesh. *Science* **2004,** *303*,5655, 217-220.
155. Auwarter, W.; Kreutz, T. J.; Greber, T.; Osterwalder, J., XPD and STM investigation of hexagonal boron nitride on Ni(111). *Surface Science* **1999,** *429*,1-3, 229-236.
156. Kouvetakis, J.; Patel, V. V.; Miller, C. W.; Beach, D. B., Composition and structure of boron nitride films deposited by chemical vapor deposition from borazine. *Journal of Vacuum Science & Technology A (Vacuum, Surfaces, and Films)* **1990,** *8*,6, 3929-3933.
157. Corso, M.; Greber, T.; Osterwalder, J., h-BN on Pd(110): a tunable system for self-assembled nanostructures? *Surface Science* **2005,** *577*,2-3, L78-L84.
158. Muller, F.; Stowe, K.; Sachdev, H., Symmetry versus commensurability: Epitaxial growth of hexagonal boron nitride on Pt(111) from B-trichloroborazine (ClBNH)(3). *Chemistry of Materials* **2005,** *17*,13, 3464-3467.
159. Shimoyama, I.; Baba, Y.; Sekiguchi, T.; Nath, K. G., NEXAFS spectra of an epitaxial boron nitride film on Ni(111). *Journal of Electron Spectroscopy and Related Phenomena* **2004,** *137*, 573-578.
160. Kuznetsov, F. A.; Golubenko, A. N.; Kosinova, M. L., A thermodynamic approach to chemical vapor deposition of boron nitride thin films from borazine. *Applied Surface Science* **1997,** *113*, 638-641.
161. Cavar, E.; Westerstrom, R.; Mikkelsen, A.; Lundgren, E.; Vinogradov, A. S.; Ng, M. L.; Preobrajenski, A. B.; Zakharov, A. A.; Martensson, N., A single h-BN layer on Pt(111). *Surface Science* **2008,** *602*,9, 1722-1726.

162. Sachdev, H.; Mueller, F.; Huefner, S., BN analogues of graphene: On the formation mechanism of boronitrene layers - solids with extreme structural anisotropy. *Diamond and Related Materials* **2004,** *19*,7-9, 1027-1033.
163. Mueller, F.; Huefner, S.; Sachdev, H.; Laskowski, R.; Blaha, P.; Schwarz, K., Epitaxial growth of hexagonal boron nitride on Ag(111). *Physical Review B* **2010,** *82*,11, 113406.
164. Sutter, P.; Lahiri, J.; Albrecht, P.; Sutter, E., Chemical Vapor Deposition and Etching of High-Quality Monolayer Hexagonal Boron Nitride Films. *Acs Nano* **2011,** *5*,9, 7303-7309.
165. Orlando, F.; Larciprete, R.; Lacovig, P.; Boscarato, I.; Baraldi, A.; Lizzit, S., Epitaxial Growth of Hexagonal Boron Nitride on Ir(111). *Journal of Physical Chemistry C* **2012,** *116*,1, 157-164.
166. Usachov, D.; Adamchuk, V. K.; Haberer, D.; Grueneis, A.; Sachdev, H.; Preobrajenski, A. B.; Laubschat, C.; Vyalikh, D. V., Quasifreestanding single-layer hexagonal boron nitride as a substrate for graphene synthesis. *Physical Review B* **2010,** *82*,7, 075415.
167. Oshima, C.; Itoh, A.; Rokuta, E.; Tanaka, T.; Yamashita, K.; Sakurai, T., A hetero-epitaxial-double-atomic-layer system of monolayer graphene/monolayer h-BN on Ni(111). *Solid State Communications* **2000,** *116*,1, 37-40.
168. Preobrajenski, A. B.; Vinogradov, A. S.; Ng, M. L.; Cavar, E.; Westerstrom, R.; Mikkelsen, A.; Lundgren, E.; Martensson, N., Influence of chemical interaction at the lattice-mismatched h-BN/Rh(111) and h-BN/Pt(111) interfaces on the overlayer morphology. *Physical Review B* **2007,** *75*,24, 245412.
169. Preobrajenski, A. B.; Nesterov, M. A.; Ng, M. L.; Vinogradov, A. S.; Martensson, N., Monolayer h-BN on lattice-mismatched metal surfaces: On the formation of the nanomesh. *Chemical Physics Letters* **2007,** *446*,1-3, 119-123.
170. Mueller, F.; Huefner, S.; Sachdev, H., One-dimensional structure of boron nitride on chromium (110) - a study of the growth of boron nitride by chemical vapour deposition of borazine. *Surface Science* **2008,** *602*,22, 3467-3476.
171. Bjelkevig, C.; Mi, Z.; Xiao, J.; Dowben, P. A.; Wang, L.; Mei, W.-N.; Kelber, J. A., Electronic structure of a graphene/hexagonal-BN heterostructure grown on Ru(0001) by chemical vapor deposition and atomic layer deposition: extrinsically doped graphene. *Journal of Physics-Condensed Matter* **2010,** *22*,30, 302002.
172. Oshima, C.; Nagashima, A., Ultra-thin epitaxial films of graphite and hexagonal boron nitride on solid surfaces. *Journal of Physics-Condensed Matter* **1997,** *9*,1, 1-20.
173. Auwarter, W.; Muntwiler, M.; Osterwalder, J.; Greber, T., Defect lines and two-domain structure of hexagonal boron nitride films on Ni(111). *Surface Science* **2003,** *545*,1-2, L735-L740.
174. Tanaka, T.; Itoh, A.; Yamashita, K.; Rokuta, E.; Oshima, C., Heteroepitaxial system of h-BN/monolayer graphene on Ni(111). *Surface Review and Letters* **2003,** *10*,4, 697-703.
175. Kawasaki, T.; Ichimura, T.; Kishimoto, H.; Akbar, A. A.; Ogawa, T.; Oshima, C., Double atomic layers of graphene/monolayer h-BN on Ni(111) studied by scanning tunneling microscopy and scanning tunneling spectroscopy. *Surface Review and Letters* **2002,** *9*,3-4, 1459-1464.

176. Laskowski, R.; Blaha, P.; Gallauner, T.; Schwarz, K., Single-layer model of the hexagonal boron nitride nanomesh on the rh(111) surface. *Physical Review Letters* **2007,** *98*,10, 064207.
177. Goriachko, A.; He, Y.; Knapp, M.; Over, H.; Corso, M.; Brugger, T.; Berner, S.; Osterwalder, J.; Greber, T., Self-assembly of a hexagonal boron nitride nanomesh on Ru(0001). *Langmuir* **2007,** *23*,6, 2928-2931.
178. Ng, M. L.; Preobrajenski, A. B.; Vinogradov, A. S.; Martensson, N., Formation and temperature evolution of Au nanoparticles supported on the h-BN nanomesh. *Surface Science* **2008,** *602*,6, 1250-1255.
179. Berner, S.; Corso, M.; Widmer, R.; Groening, O.; Laskowski, R.; Blaha, P.; Schwarz, K.; Goriachko, A.; Over, H.; Gsell, S.; Schreck, M.; Sachdev, H.; Greber, T.; Osterwalder, J., Boron nitride nanomesh: Functionality from a corrugated monolayer. *Angewandte Chemie-International Edition* **2007,** *46*,27, 5115-5119.
180. Preobrajenski, A. B.; Vinogradov, A. S.; Martensson, N., Monolayer of h-BN chemisorbed on Cu(111) and Ni(111): The role of the transition metal 3d states. *Surface Science* **2005,** *582*,1-3, 21-30.
181. Simonson, R. J.; Trenary, M., AN INFRARED STUDY OF THE ADSORPTION OF BORAZINE, (BHNH)3, ON THE PT(111) SURFACE. *Journal of Electron Spectroscopy and Related Phenomena* **1990,** *54*, 717-728.
182. Bunk, O.; Corso, M.; Martoccia, D.; Herger, R.; Willmott, P. R.; Patterson, B. D.; Osterwalder, J.; van der Veen, I.; Greber, T., Surface X-ray diffraction study of boron-nitride nanomesh in air. *Surface Science* **2007,** *601*,2, L7-L10.
183. Laskowski, R.; Blaha, P., Unraveling the structure of the h-BN/Rh(111) nanomesh with ab initio calculations. *Journal of Physics-Condensed Matter* **2008,** *20*,6, 064207.
184. Desrosiers, R. M.; Greve, D. W.; Gellman, A. J., Nucleation of boron nitride thin films on Ni(100). *Surface Science* **1997,** *382*,1-3, 35-48.
185. Cheng, Y.; Yin, X.; Liu, Y.; Li, S.; Cheng, L.; Zhang, L., BN coatings prepared by low pressure chemical vapor deposition using boron trichloride-ammonia-hydrogen-argon mixture gases. *Surface & Coatings Technology* **2010,** *204*,16-17, 2797-2802.
186. Marlid, B.; Ottosson, M.; Pettersson, U.; Larsson, K.; Carlsson, J. O., Atomic layer deposition of BN thin films. *Thin Solid Films* **2002,** *402*,1-2, 167-171.
187. Choi, B. J., Chemical vapor deposition of hexagonal boron nitride films in the reduced pressure. *Materials Research Bulletin* **1999,** *34*,14-15, 2215-2220.
188. Mueller, F.; Huefner, S.; Sachdev, H.; Gsell, S.; Schreck, M., Epitaxial growth of hexagonal boron nitride monolayers by a three-step boration-oxidation-nitration process. *Physical Review B* **2010,** *82*,7, 075405.
189. Song, L.; Ci, L.; Lu, H.; Sorokin, P. B.; Jin, C.; Ni, J.; Kvashnin, A. G.; Kvashnin, D. G.; Lou, J.; Yakobson, B. I.; Ajayan, P. M., Large Scale Growth and Characterization of Atomic Hexagonal Boron Nitride Layers. *Nano Letters* **2010,** *10*,8, 3209-3215.
190. Lee, K. H.; Shin, H.-J.; Lee, J.; Lee, I.-y.; Kim, G.-H.; Choi, J.-Y.; Kim, S.-W., Large-Scale Synthesis of High-Quality Hexagonal Boron Nitride Nanosheets for Large-Area Graphene Electronics. *Nano Letters* **2011,** *12*,2, 714-718.
191. Kim, K. K.; Hsu, A.; Jia, X.; Kim, S. M.; Shi, Y.; Hofmann, M.; Nezich, D.; Rodriguez-Nieva, J. F.; Dresselhaus, M.; Palacios, T.; Kong, J., Synthesis of Monolayer

Hexagonal Boron Nitride on Cu Foil Using Chemical Vapor Deposition. *Nano Letters* **2011,** *12*,1, 161-166.
192. Hough, W. V.; Schaeffer, G. W.; Dzurus, M.; Stewart, A. C., The Preparation, Identification and Characterization of N-Trialkylborazoles. *Journal of the American Chemical Society* **1955,** *77*,4, 864-865.
193. William, R.; Nasim, A.; Benjamin, A.; Baisong, G.; Caglar, G.; Lorenzo, M.; Feng, W.; Michael, C.; Zettl, A., A direct transfer of layer-area graphene. *Applied Physics Letters* **2010,** *96*,11, 113102.
194. Alem, N.; Erni, R.; Kisielowski, C.; Rossell, M. D.; Gannett, W.; Zettl, A., Atomically thin hexagonal boron nitride probed by ultrahigh-resolution transmission electron microscopy. *Physical Review B* **2009,** *80*,15, 155425.
195. Liu, A. Y.; Wentzcovitch, R. M.; Cohen, M. L., Atomic arrangement and electronic structure of BC2N. *Physical Review B* **1989,** *39*,3, 1760-1765.
196. Yuge, K., Phase stability of boron carbon nitride in a heterographene structure: A first-principles study. *Physical Review B* **2009,** *79*,14, 144109.
197. Kaner, R. B.; Kouvetakis, J.; Warble, C. E.; Sattler, M. L.; Bartlett, N., Boron-carbon-nitrogen materials of graphite-like structure. *Materials Research Bulletin* **1987,** *22*,3, 399-404.
198. Kawaguchi, M., B/C/N materials based on the graphite network. *Advanced Materials* **1997,** *9*,8, 615-625.
199. Watanabe, M. O.; Itoh, S.; Mizushima, K.; Sasaki, T., Bonding characterization of BC2N thin films. *Applied Physics Letters* **1996,** *68*,21, 2962-2964.
200. Kawaguchi, M.; Kawashima, T.; Nakajima, T., Syntheses and structures of new graphite-like materials of composition BCN(H) and BC3N(H). *Chemistry of Materials* **1996,** *8*,6, 1197-1201.
201. Grochala, W.; Edwards, P. P., Thermal decomposition of the non-interstitial hydrides for the storage and production of hydrogen. *Chemical Reviews* **2004,** *104*,3, 1283-1315.
202. George, W. C.; Mildred, S. D.; Michelle, V. B., The Hydrogen Economy. *Physics Today* **2004,** *57*,12, 39-44.
203. Hamilton, C. W.; Baker, R. T.; Staubitz, A.; Manners, I., B-N compounds for chemical hydrogen storage. *Chemical Society Reviews* **2009,** *38*,1, 279-293.
204. Bhatia, S. K.; Myers, A. L., Optimum Conditions for Adsorptive Storage. *Langmuir* **2006,** *22*,4, 1688-1700.
205. Furukawa, H.; Ko, N.; Go, Y. B.; Aratani, N.; Choi, S. B.; Choi, E.; Yazaydin, A.; Snurr, R. Q.; O'Keeffe, M.; Kim, J.; Yaghi, O. M., Ultrahigh Porosity in Metal-Organic Frameworks. *Science* **2010,** *329*,5990, 424-428.
206. Yuan, D.; Lu, W.; Zhao, D.; Zhou, H.-C., Porous Polymer Networks: Highly Stable Porous Polymer Networks with Exceptionally High Gas-Uptake Capacities. *Advanced Materials* **2011,** *23*,32, 3608.
207. Farha, O. K.; Ãr Yazaydan, A.; Eryazici, I.; Malliakas, C. D.; Hauser, B. G.; Kanatzidis, M. G.; Nguyen, S. T.; Snurr, R. Q.; Hupp, J. T., De novo synthesis of a metal-organic framework material featuring ultrahigh surface area and gas storage capacities. *Nat Chem* **2010,** *2*,11, 944-948.

208. Strobel, R.; Jorissen, L.; Schliermann, T.; Trapp, V.; Schatz, W.; Bohmhammel, K.; Wolf, G.; Garche, J., Hydrogen adsorption on carbon materials. *Journal of Power Sources* **1999,** *84*,2, 221-224.
209. Yang, Z.; Xia, Y.; Mokaya, R., Enhanced hydrogen storage capacity of high surface area zeolite-like carbon materials. *Journal of the American Chemical Society* **2007,** *129*,6, 1673-1679.
210. Pacula, A.; Mokaya, R., Synthesis and high hydrogen storage capacity of zeolite-like carbons nanocast using as-synthesized zeolite templates. *Journal of Physical Chemistry C* **2008,** *112*,7, 2764-2769.
211. Nishihara, H.; Hou, P.-X.; Li, L.-X.; Ito, M.; Uchiyama, M.; Kaburagi, T.; Ikura, A.; Katamura, J.; Kawarada, T.; Mizuuchi, K.; Kyotani, T., High-Pressure Hydrogen Storage in Zeolite-Templated Carbon. *Journal of Physical Chemistry C* **2009,** *113*,8, 3189-3196.
212. Morris, R. E.; Wheatley, P. S., Gas storage in nanoporous materials. *Angewandte Chemie-International Edition* **2008,** *47*,27, 4966-4981.
213. Mpourmpakis, G.; Froudakis, G. E., Why boron nitride nanotubes are preferable to carbon nanotubes for hydrogen storage? An ab initio theoretical study. *Catalysis Today* **2007,** *120*,3-4, 341-345.
214. Zhou, Z.; Zhao, J.; Chen, Z.; Gao, X.; Yan, T.; Wen, B.; Schleyer, P. v. R., Comparative study of hydrogen adsorption on carbon and BN nanotubes. *Journal of Physical Chemistry B* **2006,** *110*,27, 13363-13369.
215. Zuttel, A.; Sudan, P.; Mauron, P.; Kiyobayashi, T.; Emmenegger, C.; Schlapbach, L., Hydrogen storage in carbon nanostructures. *International Journal of Hydrogen Energy* **2002,** *27*,2, 203-212.
216. Tang, C.; Bando, Y.; Ding, X.; Qi, S.; Golberg, D., Catalyzed Collapse and Enhanced Hydrogen Storage of BN Nanotubes. *Journal of the American Chemical Society* **2002,** *124*,49, 14550-14551.
217. Schlienger, S.; Alauzun, J.; Michaux, F.; Vidal, L.; Parmentier, J.; Gervais, C.; Babonneau, F.; Bernard, S.; Miele, P.; Parra, J. B., Micro-, Mesoporous Boron Nitride-Based Materials Templated from Zeolites. *Chemistry of Materials* **2012,** *24*,1, 88-96.
218. Wideman, T.; Fazen, P. J.; Lynch, A. T.; Su, K.; Remsen, E. E.; Sneddon, L. G.; Chen, T.; Paine, R. T., Borazine, Polyborazylene, β-Vinylborazine, and Poly(β-Vinylborazine). In *Inorganic Syntheses*, John Wiley & Sons, Inc.: 2007; pp 232-242.
219. Rye, R. R.; Tallant, D. R.; Borek, T. T.; Lindquist, D. A.; Paine, R. T., Mechanistic studies of the conversion of borazine polymers to boron nitride. *Chemistry of Materials* **1991,** *3*,2, 286-293.
220. Jhi, S.-H., Activated boron nitride nanotubes: A potential material for room-temperature hydrogen storage. *Physical Review B* **2006,** *74*,15, 155424.
221. Alam, N.; Mokaya, R., Characterisation and hydrogen storage of Pt-doped carbons templated by Pt-exchanged zeolite Y. *Microporous and Mesoporous Materials* **2011,** *142*,2-3, 716-724.
222. Portehault, D.; Giordano, C.; Gervais, C.; Senkovska, I.; Kaskel, S.; Sanchez, C.; Antonietti, M., High-Surface-Area Nanoporous Boron Carbon Nitrides for Hydrogen Storage. *Adv. Funct. Mater.* **2010,** *20*,11, 1827-1833.